A Numerical and Experimental Study of Ratcheting for Head Check Initiation in Rails

Ren, F.

DOI
10.4233/uuid:d71776bf-6f44-4405-a04d-2cfdd6acdca1

Publication date
2024

Document Version
Final published version

Citation (APA)
Ren, F. (2024). *A Numerical and Experimental Study of Ratcheting for Head Check Initiation in Rails*. [Dissertation (TU Delft), Delft University of Technology]. https://doi.org/10.4233/uuid:d71776bf-6f44-4405-a04d-2cfdd6acdca1

A NUMERICAL AND EXPERIMENTAL STUDY OF RATCHETING FOR HEAD CHECK CRACK INITIATION IN RAILS

A NUMERICAL AND EXPERIMENTAL STUDY OF RATCHETING FOR HEAD CHECK CRACK INITIATION IN RAILS

Proefschrift

ter verkrijging van de graad van doctor
aan de Technische Universiteit Delft,
op gezag van de Rector Magnificus prof. ir. T.H.J.J. van der Hagen,
voorzitter van het College voor Promoties,
in het openbaar te verdedigen op 10-12-2024

door

Fang REN

Master of Science, Delft University of Technology, Delft, the Netherlands
geboren te Qingyang, Anhui, China.

Dit proefschrift is goedgekeurd door de

promotor: prof. dr. Z. Li
copromotor: dr. Z. Yang

Samenstelling promotiecommissie:

Rector Magnificus,	voorzitter
Prof. dr. Z. Li,	Technische Universiteit Delft
Dr. Z. Yang,	Technische Universiteit Delft
Onafhankelijke leden:	
Prof. dr. ir. J. Sietsma	Technische Universiteit Delft
Prof. dr. ir. R.P.B.J. Dollevoet	Technische Universiteit Delft
Prof. dr. D. Fletcher	University of Sheffield
Prof. dr. A. Ekberg	Chalmers tekniska högskola
Dr. I. Y. Shevtsov	ProRail

Printed by:

ISBN 978-94-6384-687-5

An electronic version of this dissertation is available at
http://repository.tudelft.nl/.

CONTENTS

SUMMARY

Rolling contact fatigue (RCF) poses a persistent challenge to modern railway systems, manifesting as surface cracks of rails, such as squats and head checks (HCs). If the railway track maintenance is not done timely, the damage may compromise railway longevity and lead to traffic disruptions or even accidents. Conversely, excessive maintenance to remove the cracks can be costly and disruptive to railway operations. Therefore, gaining a deep understanding of the mechanisms governing RCF damage is essential for enhancing the cost-effectiveness of maintenance strategies in the railway industry.

This dissertation combines numerical and experimental approaches to investigate the mechanisms of HC crack initiation with a specific focus on ratcheting effects in rails. A finite element (FE) model integrated with a calibrated constitutive material model was applied to simulate cyclic wheel–rail contact and the consequent rail ratcheting behaviours. Along with the numerical simulations, lab tests were conducted, including the HC replication on the V-Track (a down-scaled test rig at TU Delft) and the microscopic analysis of the HC samples, to investigate the initiation mechanisms of HC cracks and their dependence on the wheel–rail contact conditions (e.g. geometry and loading) and the contact-induced stresses in and beneath the rail surfaces. The simulated rail ratcheting effects, incorporating both material ratcheting and structural ratcheting, were also validated against the lab tests. Chapter 1 of this dissertation introduces the relevant topics and challenges in studying HCs, while Chapters 2–5 detail the steps taken to address these challenges.

Chapter 2 introduces a new FE simulation procedure designed to accurately and efficiently simulate the cyclic wheel–rail contact. The FE wheel–rail contact model was verified using the CONTACT program, and the FE meshing scheme was optimised for computational efficiency. By incorporating a non-linear kinematic hardening steel material model into the FE wheel–rail contact model, rail ratcheting behaviours were simulated under various traction conditions for up to 100 passages of typical wheel–rail frictional rolling with partial-slip contact. The findings demonstrated that cyclic wheel–rail contact can accumulate plastic deformation in the rail surface, leading to enlargement of the contact patch, reduction of contact stresses, and attenuation of further plastic deformation. The interplay between ratcheting in rail steel material and the evolution of the contact patch emerges as critical for precise predictions of rail ratcheting and HC crack initiations. The simulations also highlighted that plastic deformation and ratcheting strain accumulate rapidly initially and then stabilise. In addition, large traction coefficients can significantly increase ratcheting strain and the stabilised strain rates.

Chapter 3 delves into experimental investigations of HC initiation using the V-Track, focusing on generating ratcheting and HC damage in rails under real-life wheel–rail contact conditions. Ensuring consistent loading with high repeatability, the V-Track successfully generated rail surface HC damage under controlled conditions. Rail samples with HCs were subjected to microscopic analysis and compared with numerical stud-

ies employing the boundary element and FE methods. Both the boundary element and FE analyses successfully predicted ratcheting patterns within the contact patch, as the simulated shear stress directions correspond well to the observed microscopic plastic flows in the running band. A contrasting plastic flow pattern was noted outside the rail running band in the microscopic analysis, which can be explained by the FE contact simulations: rail material outside the contact patch may also yield via the accumulation of residual stresses.

Chapter 4 explores the mechanical, elasto-plastic, and ratcheting behaviours of three rail steels - R220, R260MN, and B320 - through uniaxial tests encompassing monotonic tension, cyclic strain ranges, and cyclic stress ranges. Two classic constitutive models, Chaboche and Ohno-Wang II (OWII), were then calibrated with the test results to model the elasto-plastic behaviours of rail steels under real-life wheel–rail contact conditions. The bainitic B320 rail steel demonstrated superior mechanical strength and notably reduced ratcheting responses compared to the pearlitic steels R220 and R260MN. The two pearlitic steels exhibited similar mechanical strength and ratcheting behaviour. The OWII model exhibited higher accuracy in reproducing the ratcheting strains and rates, while the Chaboche model struggled with reproducing low ratcheting rates.

Chapter 5 develops a framework that combines the FE simulation procedure proposed in Chapter 2 and the constitutive rail material models calibrated in Chapter 4 to simulate rail ratcheting that can lead to HC crack initiation. The framework considers both material and structural ratcheting in the FE cyclic wheel–rail contact simulations with up to 100 load cycles. Using the Chaboche models to represent B320 and R260MN rail steels, the research analysed rail plastic deformation, the evolution of the contact patch, and ratcheting rates within and outside the contact patch. The simulated results align well with the V-Track HC test results, validating the proposed framework for predicting HC crack initiation in rails. The simulations confirmed the test finding of Chapter 4 that the B320 rail demonstrated superior performance over R260MN in terms of RCF resistance. In addition, the simulations indicated that structural ratcheting during cyclic wheel–rail contact can suppress material ratcheting at the longitudinal centreline of the contact patch but intensify material ratcheting elsewhere until the contact stresses there reach the levels at the centreline. Residual stresses accumulated in the rail head outside the contact patch also (as Chapter 3) suggested potential rail material yield even without surface contact stresses.

Chapter 6 concludes the findings of this dissertation. The dissertation, in summary, proposes and validates a cyclic wheel–rail contact framework for simulating rail ratcheting effects, which can be further utilised for predicting HC crack initiations. The research enhances understanding of HC damage mechanisms by numerically and experimentally examining the relations between the wheel–rail contact conditions, contact-induced stresses in and beneath rail surfaces, rail material type and properties, rail ratcheting plastic flow and the crack initiation patterns. This enhanced understanding is expected to improve the accuracy of future RCF predictions and contribute to the cost-effectiveness and efficiency of railway maintenance and operations.

SAMENVATTING

Rolling Contact Fatigue (RCF), vermoeiing ten gevolge van het rollende contact tussen rail en wiel, vormt een voortdurende uitdaging voor moderne spoorwegsystemen. RCF leidt tot oppervlaktescheuren in rails, zoals squats en head checks (HCs). Onvoldoende onderhoud kan de levensduur van het spoor negatief beïnvloeden en kan leiden tot verstoringen van de treindienst of zelfs tot ongevallen. Overdadig onderhoud daarentegen is kostbaar en verstorend voor de exploitatie. Inzicht in de mechanismen achter RCF-schade is essentieel voor het verbeteren van de kosteneffectiviteit van onderhoudsstrategieën in de spoorwegindustrie.

Dit proefschrift combineert numerieke en experimentele benaderingen om de mechanismen van HC-scheurinitiatie te onderzoeken, met specifieke aandacht voor ratcheting effecten in rails. Een eindige-elementenmodel (EE), geïntegreerd met een gekalibreerd constitutief materiaalmodel werd toegepast om cyclisch wiel-railcontact en de resulterende rail-ratcheting gedragingen te simuleren. Naast numerieke simulaties werden laboratoriumtests uitgevoerd, waaronder HC-nabootsing op de V Track (een geschaalde testopstelling aan de TU Delft) en microscopische analyse van HC-monsters, om de initiatiemechanismen van HC-scheuren en hun afhankelijkheid van wiel-rail contactcondities en contact geïnduceerde spanningen te onderzoeken. De gesimuleerde rail-ratcheting effecten, die zowel materiaal- als structurele ratcheting omvatten, werden ook gevalideerd met de laboratoriumtests. Hoofdstuk 1 van dit proefschrift introduceert de relevante onderwerpen en uitdagingen bij het bestuderen van HC's, terwijl de hoofdstukken 2-5 de stappen beschrijven die zijn genomen om deze uitdagingen aan te pakken.

Hoofdstuk 2 introduceert een nieuwe EE-simulatieprocedure voor nauwkeurige en efficiënte simulatie van cyclisch wiel-railcontact. Het EE wiel-railcontactmodel werd geverifieerd met het CONTACT-programma en het EE-meshing schema werd geoptimaliseerd voor computationele efficiëntie. Door een niet-lineair kinematisch verhardend staalmodel te integreren in het EE wiel-railcontactmodel, werden rail-ratcheting gedragingen gesimuleerd onder verschillende tractiecondities voor maximaal 100 passages van typisch wiel-rail wrijvingscontact met gedeeltelijke slip. De bevindingen toonden aan dat cyclisch wiel-railcontact plastische vervorming in het railoppervlak kan accumuleren, wat leidt tot vergroting van het contactvlak, vermindering van contactspanningen en afzwakking van verdere plastische vervorming. De wisselwerking tussen ratcheting in railstaalmateriaal en de evolutie van het contactvlak blijkt cruciaal voor nauwkeurige voorspellingen van rail-ratcheting en HC-scheurinitiatie. De simulaties benadrukten ook dat plastische vervorming en ratcheting vervorming aanvankelijk snel accumuleren en vervolgens stabiliseren. Bovendien kunnen hoge tractiecoëfficiënten de ratcheting vervorming en de gestabiliseerde vervormingssnelheden aanzienlijk verhogen.

Hoofdstuk 3 gaat in op experimenteel onderzoek naar HC-initiatie met behulp van de V Track, gericht op het genereren van ratcheting en HC-schade in rails onder realistische

wiel-rail contactcondities. Door een consistente belasting met een hoge herhaalbaarheid te garanderen, genereerde de V-Track onder gecontroleerde omstandigheden succesvol HC- schade aan het railoppervlak. Railmonsters met HC's werden microscopisch geanalyseerd en vergeleken met numerieke studies met behulp van de grenslaag- en EE-methoden. Beide methoden voorspelden succesvol ratcheting patronen binnen het contactvlak, aangezien de gesimuleerde schuifspanningsrichtingen goed overeenkomen met de waargenomen microscopische plastische vervormingen in de loopband. Een contrasterend plastisch vervormingspatroon werd buiten de railloopband opgemerkt in de microscopische analyse, wat kan worden verklaard door de EE-contactsimulaties: railmateriaal buiten het contactvlak kan ook bezwijken door de accumulatie van restspanningen.

Hoofdstuk 4 onderzoekt het mechanische, elasto-plastische en ratchetinggedrag van drie railstaalsoorten - R220, R260MN en B320 - door middel van uniaxiale tests met monotone trek, cyclische rekbereiken en cyclische spanningsbereiken. Twee klassieke constitutieve modellen, Chaboche en Ohno-Wang II (OWII), werden vervolgens gekalibreerd met de testresultaten ten einde het elasto-plastische gedrag van railstalen onder realistische wiel-railcontactcondities te modelleren. Het bainitische B320 railstaal toonde superieure mechanische sterkte en aanzienlijk verminderde ratchetingreacties in vergelijking tot de perlitishe stalen R220 en R260MN. De twee perlitishe stalen vertoonden vergelijkbare mechanische sterkte en ratchetinggedrag. Het OWII-model toonde hogere nauwkeurigheid in het reproduceren van de ratchetingvervormingen en -snelheden, terwijl het Chaboche-model moeite had met het reproduceren van lage ratchetingsnelheden.

Hoofdstuk 5 ontwikkelt een raamwerk dat de EE-simulatieprocedure uit hoofdstuk 2 combineert met de gekalibreerde constitutieve railmateriaalmodellen uit hoofdstuk 4 om rail-ratcheting te simuleren die kan leiden tot HC-scheurinitiatie. Het raamwerk houdt rekening met zowel materiaal- als structurele ratcheting in de EE cyclische wiel-railcontactsimulaties met maximaal 100 belastingcycli. Met behulp van de Chaboche modellen om B320 en R260MN railstalen te vertegenwoordigen, analyseerde het onderzoek rail plastische vervorming, de ontwikkeling van het contactvlak en ratchetingsnelheden binnen en buiten het contactvlak. De gesimuleerde resultaten komen goed overeen met de V-Track HC-testresultaten, wat de validiteit van het voorgestelde raamwerk voor het voorspellen van HC-scheurinitiatie in rails bevestigt. De simulaties bevestigden de testbevinding van hoofdstuk 4 dat het B320 railstaal superieure prestaties vertoonde ten opzichte van R260MN wat betreft RCF-bestendigheid. Bovendien gaven de simulaties aan dat structurele ratcheting tijdens cyclisch wiel-railcontact materiaalratcheting kan onderdrukken op de longitudinale middenlijn van het contactvlak, maar materiaalratcheting elders kan intensiveren totdat de contactspanningen daar de niveaus op de middenlijn bereiken. Restspanningen die zich ophopen in de railkop buiten het contactvlak suggereren ook potentieel railmateriaalbezinking zelfs zonder oppervlaktecontactspanningen.

Hoofdstuk 6 concludeert de bevindingen van dit proefschrift. Samenvattend stelt het onderzoek een cyclisch wiel-railcontactraamwerk voor en valideert dit voor het simuleren van rail-ratchetingeffecten, wat verder kan worden gebruikt voor het voorspellen van HC-scheurinitiaties. Het onderzoek verbetert het begrip van HC-schademechanismen

door numeriek en experimenteel de relaties te onderzoeken tussen wiel-rail contactcondities, contact geïnduceerde spanningen, railmateriaaltype en -eigenschappen, railratcheting plastische vervorming en scheurinitiatiepatronen. Deze verbeterde kennis zal naar verwachting de nauwkeurigheid van toekomstige voorspellingen van RCF verbeteren en bijdragen aan de kosteneffectiviteit en efficiëntie van het onderhoud en de exploitatie van het spoorsysteem.

PREFACE

Wir müssen wissen.
Wir werden wissen.

David Hilbert
1930

1

INTRODUCTION

1

1.1. THE ROLLING CONTACT FATIGUE PROBLEM

Modern railways have been subjected to rolling contact fatigue (RCF) damages for decades. RCF stems from the cyclic frictional rolling contact at the wheel–rail interface, where the contact stresses often exceed the yield strength of the rail steels. RCF can result in cracks initiated in or beneath the rail surface and propagating downwards into the rail, potentially causing rail breakage and thus posing significant risks to railway operations [1].
The most common types of RCF damage are squats and head checks (HCs), as examples shown in Figure 1.1. Squats are often associated with rail surface irregularities, such as joints, welds, wheel burns and corrugation [2], [3]. Local stress concentrations, exacerbated by repeated wheel passages, can result in the initiation and propagation of cracks into the rail head material at these locations [4]. In contrast to the localised nature of squats, HCs can be found over a broader range in railway networks, particularly on high rails of curved tracks [5], [6]. HCs are clusters of inclined cracks that are regularly and closely distributed in the rail shoulder and gauge corner (see Figure 1.1(b)) [7]. This Ph.D. research focuses primarily on HCs.

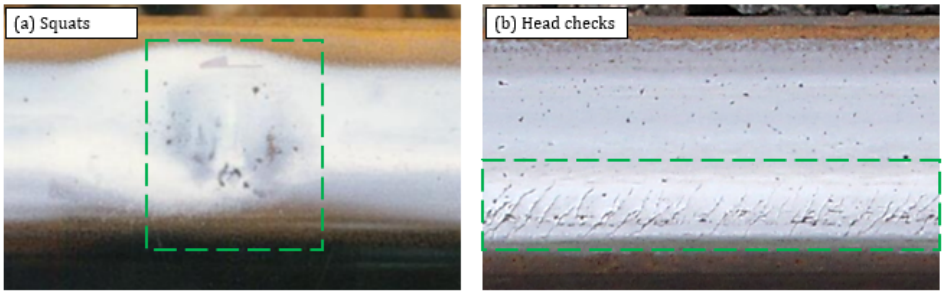

Figure 1.1: The types of RCF damage: (a) Squats [8] and (b) HCs

1.2. INITIATION AND PROPAGATION OF HC CRACKS

1.2.1. HC CRACK INITIATION

Studies [9], [10] have shown that the ratcheting effect, i.e. accumulation of plastic deformation caused by cyclic large-amplitude contact shear stresses, is the direct cause of HC cracks. Rail ratcheting behaviour can be affected by many factors, including the wheel–rail contact forces and geometry, and properties of the rail steel [11].
The wheel–rail contact geometry changes during the rail operation, especially when the bogie negotiates a curve, as shown in Figure 1.2. On a tangent track, the wheel tread is usually in contact with the rail crown, as shown in Figure 1.2(a) and (c) with the contact marked by a green rectangle. The contact is shifted laterally to the rail gauge side due to the angle of attack and train centrifugal force when the wheel enters the curve. This shift pushes the wheel flange root in contact with the rail shoulder or gauge corner, as shown in Figure 1.2(b) and (c) with the contact marked by an orange rectangle. The wheel flange root has a significant conical profile that may introduce large geometrical spin and creep forces in the lateral direction. The lateral creep force introduced by the conical wheel contact, together with possible traction or braking forces, can result in

substantially increased shear stresses in the contact patch compared to that on tangent tracks. The high shear stresses may then yield the rail steel, inducing plastic deformation in the rail top.

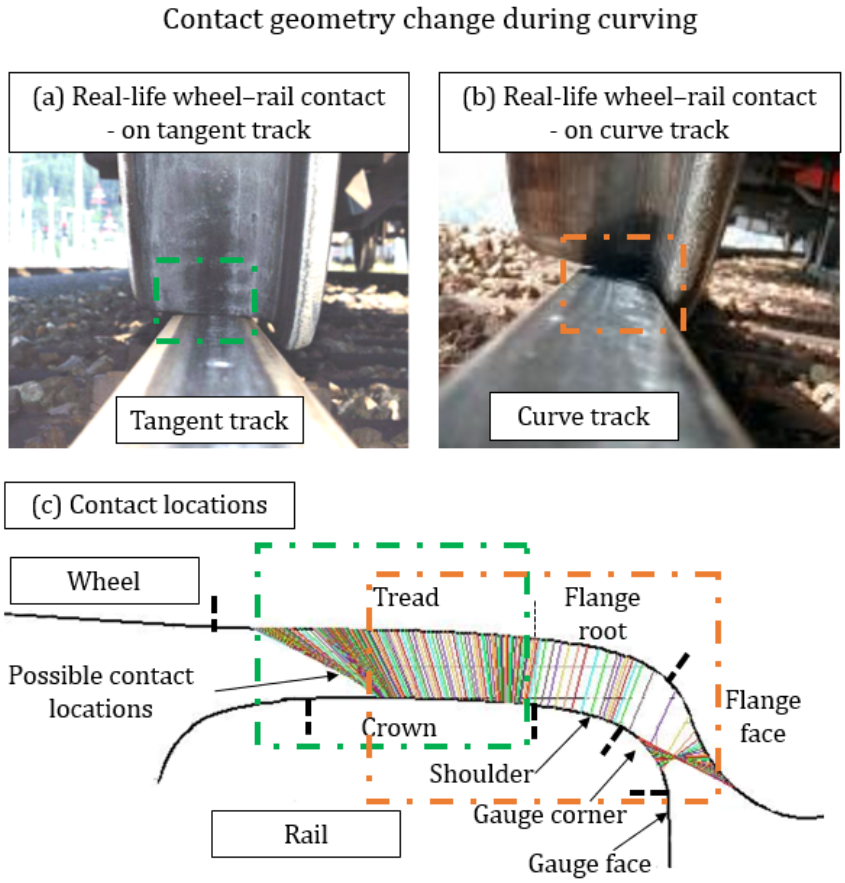

Figure 1.2: Variation of wheel–rail contact geometry: (a) on a tangent track (b) on a curve track, and (c) the pertinent wheel–rail contact locations

When the high contact stresses exceed the plastic shakedown limit [12], plastic deformation begins to accumulate in the rail under the cyclic wheel–rail contacts [13]. This process is referred to as ratcheting, which manifests itself as the accumulating plastic flow in the rail surface layer driven by the contact shear stress. Cracks can be initiated when ratcheting exhausts the ductility of the material [14], [15]. HC cracks can subsequently initiate in the layer with severe plastic deformation, following the orientation of the ratcheting plastic flow [16].

1.2.2. CRACK PROPAGATION

The initiated cracks can grow into the bulk material [7], stop at the quiescent zone [14], or come back to surface, resulting in pitting or spalling [17]. The propagation of cracks is propelled by shear stresses and can be accelerated by the fluid trapped in the cracks [18]. In dry conditions, the contact-induced shear stresses force the crack faces to slide over each other [7]. With the presence of fluid, e.g. water, in the cracks, the hydraulic pressure from the fluid would push the cracks further open, exacerbating the crack propagation, since the stress intensities in this case are higher, contributing significantly to crack expansion. Eventually, with the crack propagation extended, horizontal and vertical branching occurs with the cracks growing deeper and faster leading to rail fracture [19].

1.2.3. ROLE OF RAIL STEEL

The properties of the rail steels play an important role in the initiation and propagation of HC cracks. The mechanical properties of steels on the macro-scale are closely related to their microstructures [20], [21], which decide the elasto-plastic behaviour of the steels (e.g. ratcheting), and thus influence the initiation of HC cracks. Additionally, distinct features in their microstructures could also affect the propagation of the RCF cracks [22]. Extensive research [20], [21], [23]–[26] has been conducted on the pearlitic rail steels that are widely used in modern railways. Figures 1.3(a) and (b) show the undeformed microstructures of the pearlitic R260MN and MHH rail steels under a scanning electron microscope (SEM). The pearlite microstructure consists of two phases with alternating lamellae of ferrite (bright, white) and cementite (dark, grey) in various clusters of pearlite colonies within prior austenite grain boundaries [21]. The mechanical properties of the pearlitic rail steels have been found to be closely associated with the prior austenite grain size, the inter-lamella spacing (the space between cementite lamellae) [20], [21], and the size of the pearlite colonies [21]. The smaller inter-lamella spacing and prior austenite grain size, finer pearlite colonies would contribute to the higher tensile strength and ductility, whereas a higher carbon content could reduce the ductility of pearlitic steel [21]. A comparison between Figures 1.3 (a) and (b) on the same scale confirms that the MHH steel has higher mechanical strength than the R260MN [27], as indicated by its much finer distribution of pearlite lamellae with smaller inter-lamella spacing.

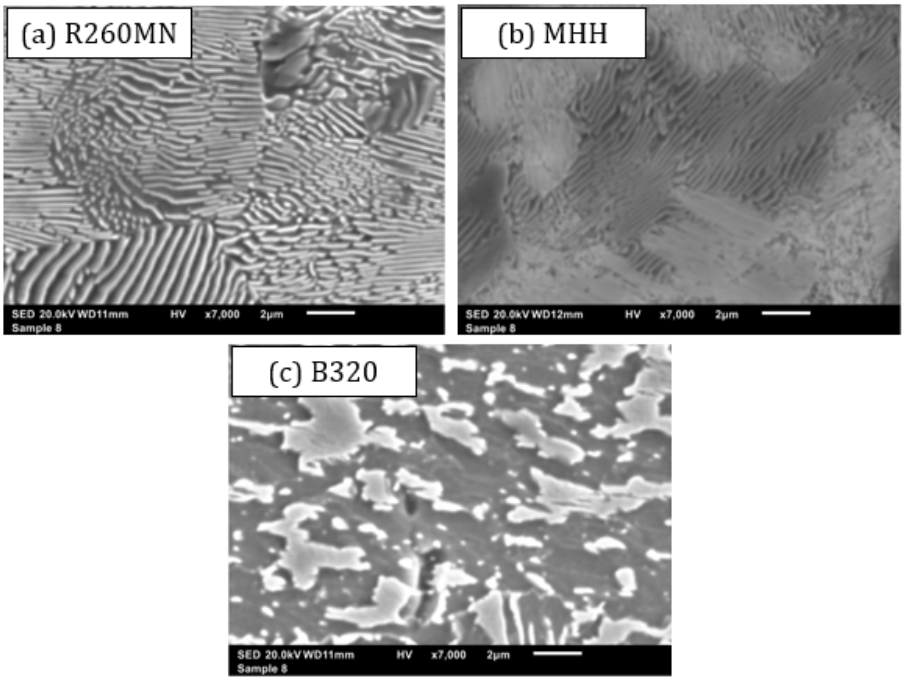

Figure 1.3: The undeformed microstructure of the rail steels under SEM: (a) Pearlitic R260MN (b) Pearlitic MHH, and (c) Bainitic B320

Recent studies have shown that carbide-free bainitic rail steels have better mechanical properties and improved RCF resistance compared to pearlitic rail steels [28]. Figure 1.3(c) shows the distinctive microstructure of a bainitic steel B320. Its microstructure consists mainly of bainite ferrite, blocky and film-like austenite, and limited carbide [22]. The finer microstructure in bainite and the low content of carbide were found to contribute to the improvement of mechanical strength [28], and the retained austenite also helps to enhance its RCF resistance [22].

The wheel–rail rolling contact-induced shear stress can reorganise the microstructure, forming plastic flow patterns, as shown in Figure 1.4. In the pearlitic rails, the cementite lamellae break [24] and reorient with the ferrite phases [29], flowing in the direction of dominant shear stresses[25], [26]. This reorientation of the ferrite lamellae on the micro-scale manifests a pattern identified as plastic flow, which can be clearly observed under a light optical microscope (LOM) in Figure 1.4(a). The accumulation of this plastic flow under wheel–rail contact is referred to as ratcheting observed on a micro-scale for the pearlitic steels. For the bainitic B320 rail steel, the reorientation of the ferrite and the accumulation of plastic flow, i.e. ratcheting, are less distinguishable, although the re-organisation in the microstructure can also be seen in the part close to the surface, as shown in Figure 1.4(b). The associations between the contact shear stress, elasto-plastic behaviour and the change in the microstructure of rail steels during wheel–rail contact are also of interest for this Ph.D. research.

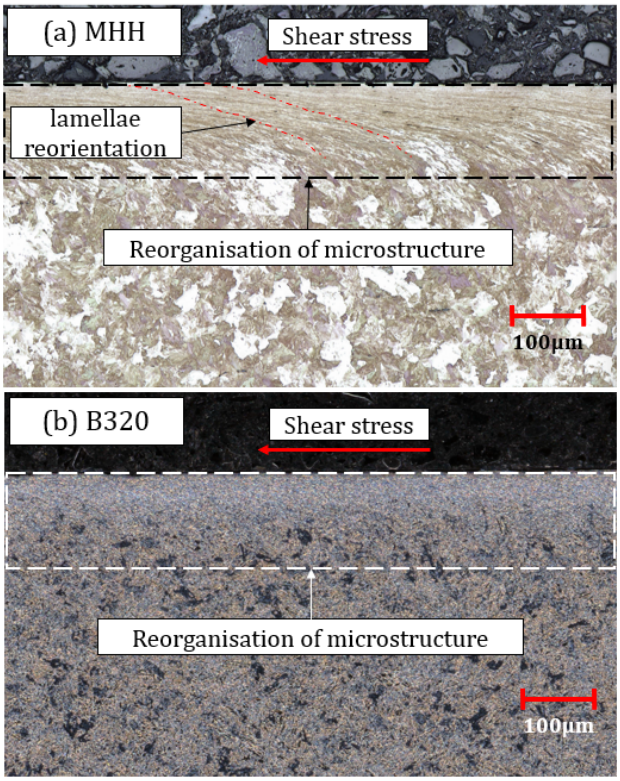

Figure 1.4: The deformed microstructure of the rail steels by shear stress under LOM: (a) Pearlitic MHH, and (b) Bainitic B320

1.3. PLASTICITY IN RAIL STEEL

1.3.1. THE ELASTO-PLASTIC BEHAVIOURS

This section discusses the mechanical properties of rail steels on a macro-scale, i.e. the elaso-plastic behaviours. Steels under certain loads develop elasto-plastic behaviours, which can be represented by stress–strain relations, with R260MN rail steel as an example shown in Figure 1.5. When the stress is lower than the yield stress (different from the yield strength as shown in Figure 1.5), only elastic strain is generated, showing a linear response in the stress–strain relation indicated by the elastic range in the figure. The elastic strain is reversible when the steel is unloaded. When the yield stress is exceeded, plastic behaviours occur forming a non-linear relation between the stress and strain. Plastic strain is irrecoverable when the steel is unloaded, as exhibited by the multiple loading–unloading case in Figure 1.5. When the stress exceeds the ultimate strength, i.e. the maximum plastic strain, the steel will fail. Note that the elasto-plastic behaviours discussed in this dissertation are strain rate-independent, i.e., the strain rate effect (visco-plasticity) is not considered in the material modelling [30], [31].

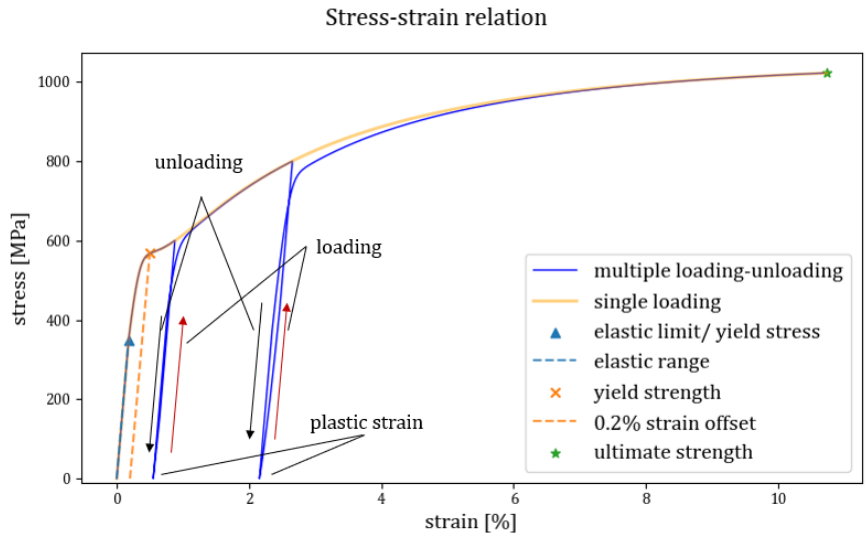

Figure 1.5: Stress–strain relation of steel of R260MN rail steel

In the fatigue or RCF study, the stress–strain responses under cyclic loading are of specific concern. Depending on the stress/strain loading conditions, the elasto-plastic behaviour of steel can be categorised into four general scenarios [32], [33], with the R260MN rail steel as an example simulated in this study shown in Figure 1.6:

a) Elastic. When the stress range is within the elastic range, the strain response is linear elastic and reversible, as shown in Figure 1.6 (a).

b) Elastic shakedown. Although the initial stress yields the steel, the subsequent stress range does not cause the hardened/softened steel to yield further. The steel behaves elastically under the stress range as shown in Figure 1.6 (b,ii).

c) Plastic shakedown. This often occurs when the steel is loaded with a symmetrical stress or strain range with a zero-mean stress level (Figure 1.6 (c,i)). Substantial plastic strain is generated with the hysteresis loop created (Figure 1.6 (c,ii)) but its growth stalls after a limited number of load cycles. Since plastic strains occur during the cyclic loading, this process is often referred to as low cycle fatigue (LCF) [33]. The plastic shakedown can also occur during the mean stress relaxation process, where steel is loaded by asymmetric strain range [33] and the mean stress gradually reduces to zero.

d) Ratcheting. Ratcheting occurs when the stress range is higher than the yield stress range and the mean stress level is non-zero, as shown in Figure 1.6(d,i). The accumulation of directional plastic strains occurs following the mean stress direction [33]. The associated fatigue process can be considered as a special type of LCF, but it is more commonly referred to as ratcheting fatigue [33], [34] to be differentiated from plastic shakedown.

1

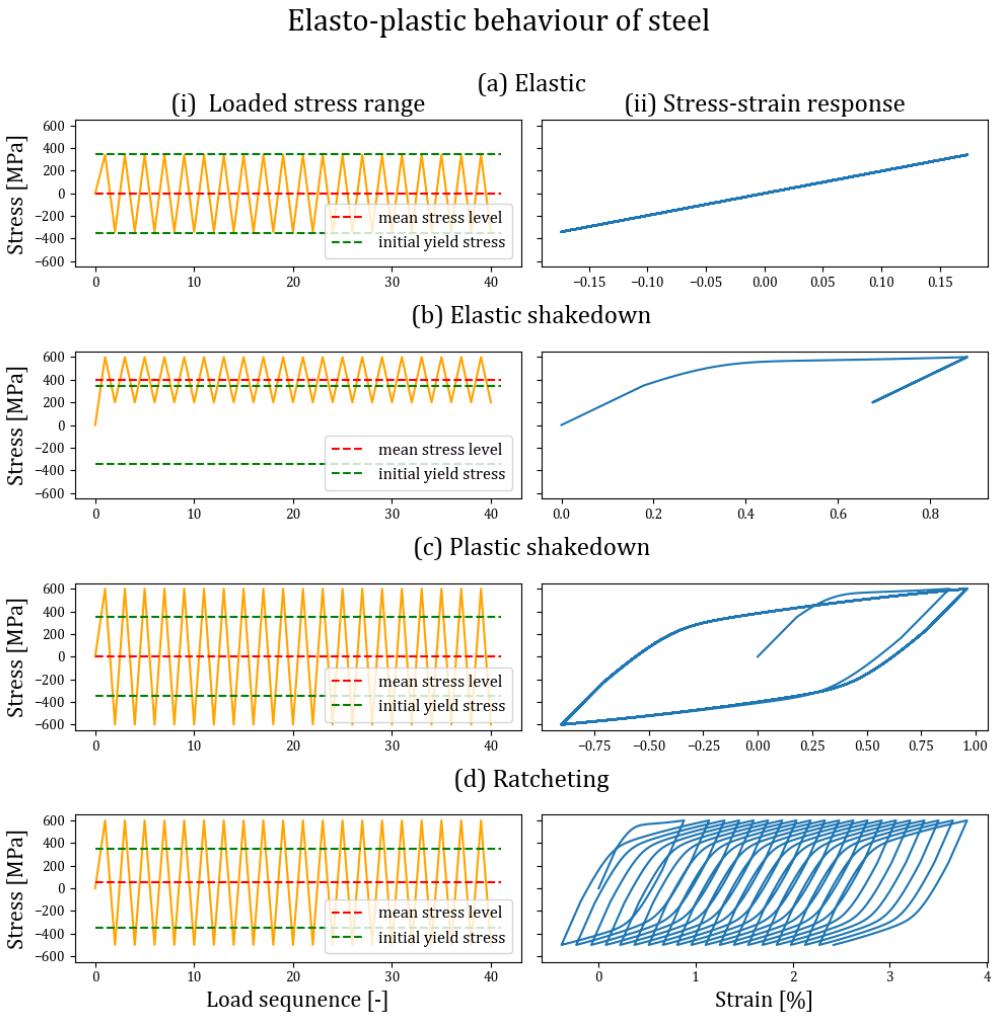

Figure 1.6: The simulated elasto-plastic behaviour of the R260MN rail steel, column. (i): the loaded stress ranges for each scenario, column (ii): the simulated stress-strain responses; row (a) elastic behaviour, row (b) elastic shakedown, row (c) plastic shakedown, row (d) ratcheting

1.3.2. RATCHETING

As discussed in Section 1.2.1, ratcheting has been directly attributed to the initiation of HC cracks. The ratcheting phenomenon can be classified into two types: material ratcheting and structural ratcheting [33], [35]. The material ratcheting is considered as an intrinsic elasto-plastic behaviour of steel (see Figure 1.6) and has been extensively investigated via material tests that load steel samples homogeneously with an asymmetric cyclic stress range (non-zero mean stress) [36]–[38], per Figure 1.6(d,i). In contrast, structural ratcheting refers to the accumulation of plastic strain under unevenly distributed and varying loading stress conditions, which does not necessarily require the consideration of material ratcheting [35]. The multiple loading-unloading case shown in Figure 1.5 demonstrates an example of structural ratcheting: the increases in the stress during the second and third loading effectively accumulate the plastic strain.

For the railway application, material ratcheting has been studied for many rail steel types, mainly the pearlitic steels [15], [39], by conducting material tests, while rail structural ratcheting has barely been addressed. During the real-life wheel–rail contact, normal and shear contact stresses are unevenly distributed, and both the contact patch and stresses alter during cyclic contacts [40]. Therefore, the rail ratcheting behaviour with the consideration of structural ratcheting may differ from those obtained with the material tests tests under simplified loading conditions and the simulations assuming line-contact or uniform contact stress. This Ph.D. research aimed to incorporate both the ratcheting forms into the ratcheting tests and simulations to accurately replicate the complete ratcheting effects in rails.

1.3.3. CONSTITUTIVE MODELLING

Constitutive models have been used to characterise the elasto-plastic properties of steels, including the material ratcheting, following three fundamental rules: the yield criteria, the normality flow rule and the hardening rule [36], [41]. The von Mises yield criterion is mostly used for metals [42], [43], which defines a yield surface consisting of deviatoric stresses and yield stress. Plasticity occurs when the deviatoric stresses are on or beyond the yield surface bounded by a radius equal to the yield stress. The normality flow rule stipulates that the plastic flow should follow the gradient of the yield surface with respect to the change in stresses, and determines the increment in plastic strain. The hardening rules specify the change in deviatoric and yield stresses with respect to the plastic strains.

Existing constitutive models generally consider two primary hardening processes in the elastoplastic behaviour of steels: isotropic and kinematic hardening. The sum of the yield stress of isotropic hardening/softening and the backstress of kinematic hardening equals the total stress (or equivalent stress) in a uniaxial loading case according to the von-Mises yield criterion [36], [42], as shown in Figure 1.7 (also applicable to a multiaxial case). Figure 1.7 also shows that the isotropic hardening/softening process alters the yield stress: the yield stress may increase (by hardening) or decrease (by softening) as a result of accumulating (effective) plastic strains [36], [44], corresponding to an expansion or a contraction of the yield surface, respectively. On the other hand, kinematic hardening is characterised by the introduction of backstresses into the yield function to account for the anisotropy [45], [46] or the Bauschinger effect that shifts the yield surface

as plastic strains accumulate [36], [43], [47]. The incremental backstresses can be formulated linearly or non-linearly with respect to the increment of plastic strain. To be able to accurately replicate material ratcheting, the non-linear kinematic hardening (NLKH) should thus be considered in the constitutive model that has both a linear and nonlinear term in the backstresses [43]. Various NLKH models have been developed with different formulations of the nonlinear parts in the backstresses [36], [37], [43], [47]–[49], which may be utilised for the material modelling of the rail steel in this dissertation.

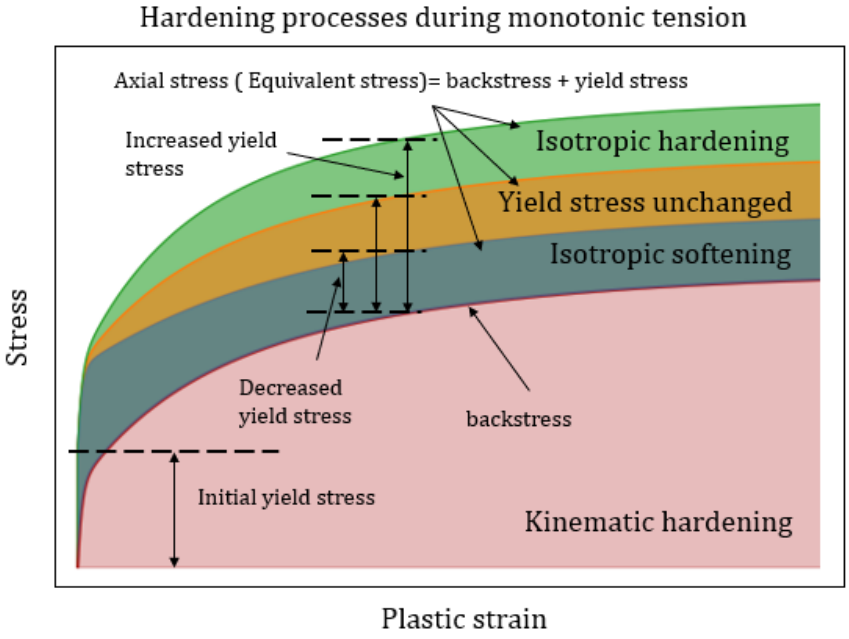

Figure 1.7: An overview of the stress-strain relation of steel during the hardening/softening processes

1.4. EXPERIMENTAL INVESTIGATION

RCF has been experimentally investigated with various test rigs [5], [50], [51], as shown in Figure 1.8, among which the twin-disc setup has been most widely used [14], [15], [50], [52]–[59]. The twin-disc tests were favoured with their simple setup consisting of two discs/rollers to represent the rail and wheel. Twin-disc test rigs have their advantage in fast testing speed, ease of handling, and control of the test parameters. By adjusting the rotation and alignment of the discs, the longitudinal and lateral creep can be easily generated and monitored during the tests. However, the contact conditions replicated during the twin-disc tests could differ significantly from the real-life wheel–rail contacts. Furthermore, the twin-disc test setup could hardly facilitate the testing of multiple rail types in one test. In addition, the disc-shaped rail representation may not avoid the unevenly-distributed hardness in a head-hardened rail [6], [60].

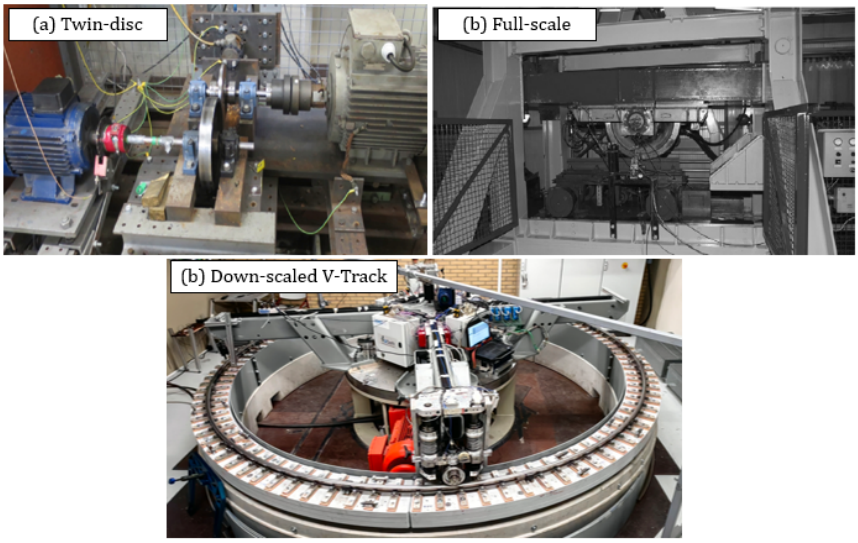

Figure 1.8: The test rigs used to study RCF, (a) twin-disc [55] (b) full-scale voelstapine test rig [5], and (c) down-scaled V-track test rig

Full-scale test rigs, as an example shown in Figure 1.8(b), have been used more recently to generate HCs [5], [9], [11], [22], [61], [62]. This type of test rig usually has the rail as the moving part, loaded vertically and laterally to contact with the wheel, at a relatively low speed, e.g. $1.0 m/s$ (the Voelstapine test rig [5]). These test rigs can generate more realistic contact conditions using the original wheel–rail profiles. Due to the large-scale nature, the tested rails are relatively short ($1.5 m$), possibly limited by the size and weight due to the full-scale nature. Furthermore, these test rigs do not incorporate an active torque in the wheels, which limits the control of traction conditions during the HC tests. In addition, the full-scale test setups with the original wheel–rail contact profile could result in a complex contact condition, e.g. with multi-point and various contact radii (Figure 1.9(a)), making the trace and control of the contact conditions much more complicated than a simple conical or cylindrical wheel (Figure 1.9(b)).

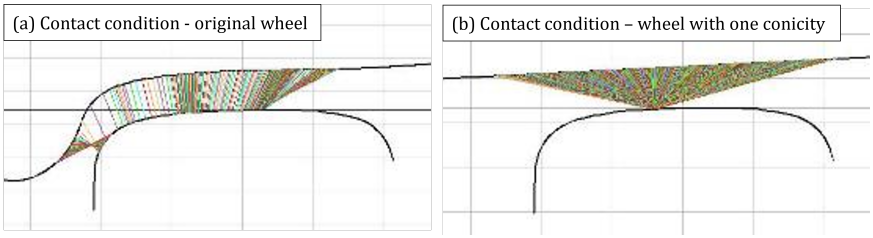

Figure 1.9: Comparison of contact conditions (a) original wheel–rail, and (b) one-conicity wheel–rail

The down-scaled V-Track test rig [63], as shown in Figure 1.8(c), has been developed at TU Delft to test various vehicle–track interaction-induced phenomena, such as wheel–

rail friction/adhesion behaviour [64], rail corrugation [58], wheel polygonisation [65], and HCs [51], [66]. The wheel–rail contact geometries and loading conditions can be well controlled and measured in the V-Track. In addition, the ring track design [63] (see Figure 1.8(c)) allows multiple rails to be tested simultaneously and under comparable loading conditions, greatly improving the productivity and effectiveness of fatigue tests of fatigue tests. This Ph.D. work extensively used the V-Track to generate HC damage, and to study the ratcheting and initiation mechanisms of HCs in different rail steels.

1.5. NUMERICAL INVESTIGATION

The problems of RCF crack initiation have also been numerically investigated using qualitative and quantitative approaches. The qualitative approaches use the (deformed) contact profiles to approximate contact conditions and examine the causes of squats or HC cracks [9], [10], [67]. The boundary element method (BEM) [68]–[70] and finite element method (FEM) [71]–[74] have been mostly employed to simulate a single-cycle wheel–rail contact assuming linear elasticity or simple bilinear plasticity, and to find the correlations among the contact-induced stress patterns and plastic strain or crack orientation [9], [10], [51], [67]. The influences of contact conditions (e.g. loading) on the initiation of RCF damage can then be estimated [2], [3], [75]. The qualitative approach is an effective way to identify the possible mechanism for RCF damage but is insufficient to quantify the actual effects of these mechanisms, e.g. ratcheting, or accurately predict the initiation of RCF-related cracks.

By simulating cyclic wheel–rail contact, quantitative approaches have been proposed to examine RCF, particularly HC, in a more precise way [34], [76]. To realise this, a material model that can replicate material ratcheting, e.g. the NLKH constitutive model, and a contact model to capture the real-life structural ratcheting in rails are essential. The constitutive material models discussed in Section 1.3.3 have been widely used in ratcheting simulations[34], [57], [76]–[80]. As for contact models, since the ratcheting simulations involve a large number of load cycles, simplification was often made, especially in the finite element (FE) models, for computational efficiency. These models, either simplified the 3D wheel–rail contact to a 2D line contact [34], [81], or only modelled one contact body subjected to prescribed contact stresses [57], [76], [82], [83]. The influence of structural ratcheting at the wheel–rail interface that comprises unevenly distributed and evolving contact stresses cannot be well treated with such simplifications.

In this Ph.D. research, both qualitative and quantitative approaches were used to study the ratcheting in rails. The CONTACT programme based on BEM was used to perform a quick contact stress analysis that can give qualitative predictions of plastic deformation patterns, which was compared with the results of the V-Track test. A reliable and efficient FE simulation procedure was then developed to quantitatively study the wheel–rail contact variation (in terms of contact geometry/patch and contact-induced stress amplitudes/distributions) with load cycles and ratcheting effects in different types of rail steel. The FE solutions were also validated against the V-Track tests.

1.6. RESEARCH QUESTIONS

This Ph.D. work aims to answer the following primary research question:

- How can we accurately predict rail ratcheting and enhance the understanding of HC initiation?

The following sub-questions are formulated to embody the primary research objective:

- How can the actual stress conditions and the ratcheting behaviour in the rails be accurately and efficiently captured in an FE simulation with a large number of wheel–rail contact cycles?
- How can the ratcheting behaviour and subsequent HC crack initiation be influenced by wheel–rail contact conditions?
- How can the elasto-plastic behaviours of rail steels under real-life operational conditions be experimentally investigated and characterised with classic constitutive models for ratcheting simulations?
- How can the material and HC experiments be used to calibrate and validate the rail ratcheting prediction models?

1.7. OUTLINE OF THIS DISSERTATION

This dissertation is structured into four subsequent main chapters (Chapters 2-5) , each focusing on one of the four sub-questions, with an overarching aim of building a framework to address the primary research question, and a concluding chapter (Chapter 6). Figure 1.10 shows an outline of the main chapters. Chapter 2 presents an efficient FE ratcheting simulation procedure that can automatically execute and post-process a large number of wheel–rail contact cycles. The proposed FE model features an optimised and accurate wheel–rail contact model and an NLKH material model. This FE simulation procedure formed the basis for the numerical studies of ratcheting in the following chapters. Chapter 3 combines the experimental (V-Track HC tests and microscopic analysis) and numerical approaches to investigate the initiation mechanisms of HCs and the influences of wheel–rail contact-induced stress conditions within and outside the contact patch. In Chapter 4, the material ratcheting properties of the three rail steels R220, R260MN and B320 are experimentally assessed and characterised by two widely-used constitutive material models, whose hardening parameters are further optimised to replicate the material ratcheting of the rail steels. Chapter 5 comprehensively investigates the ratcheting effects in the R260MN and B320 rails by incorporating the material ratcheting behaviour characterised in Chapter 4 and the structural ratcheting replicated with the accurate modelling approach developed in Chapter 2. The simulated ratcheting effects are in good agreement with the experimental observations. The ratcheting simulation also confirmed the findings in Chapter 3 that rail ratcheting may occur outside the running band. The final chapter wrapped up this dissertation by summarising the primary findings and proposing potential areas for future investigations.

1

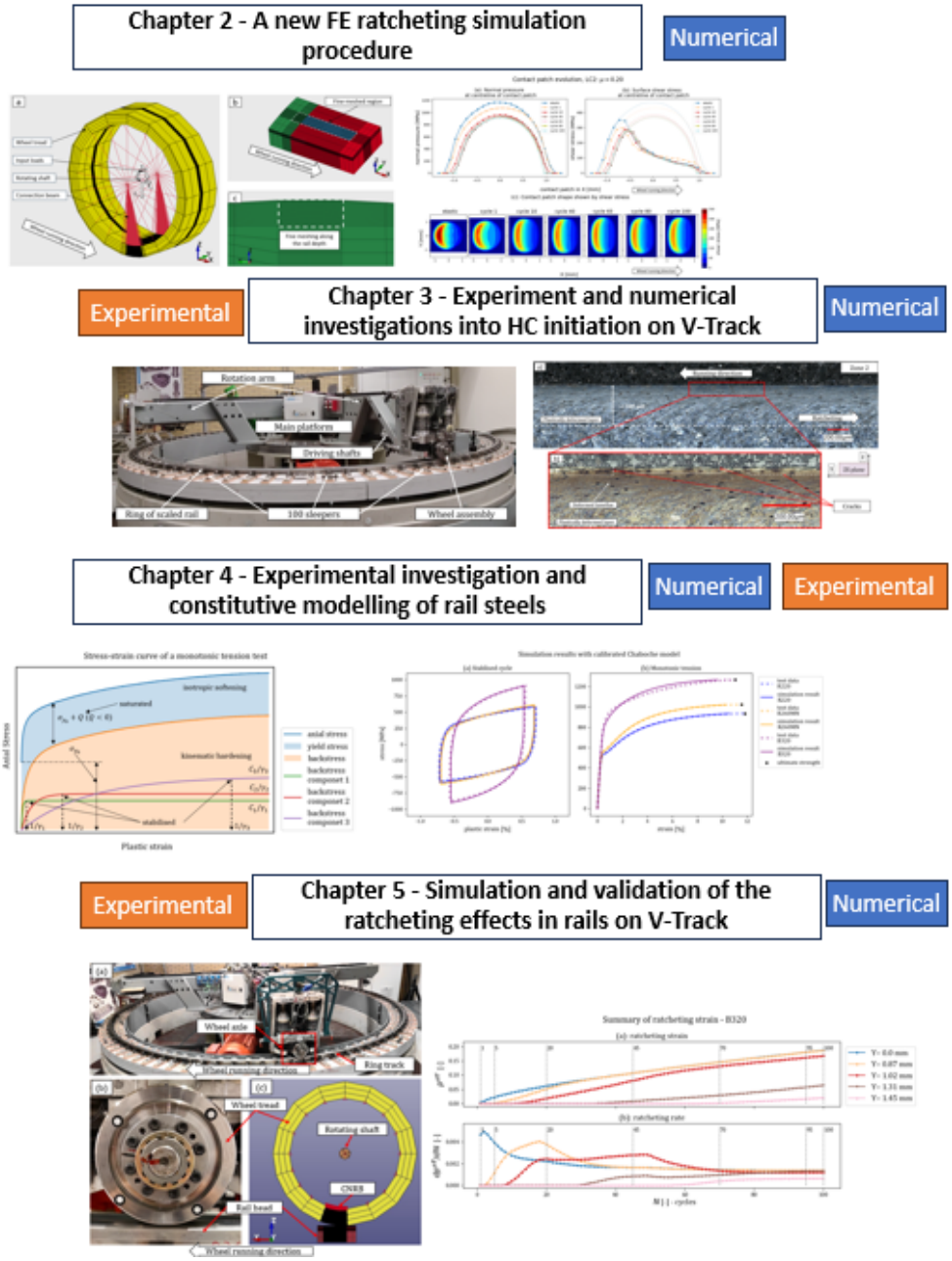

Figure 1.10: Outline of the main chapters in the dissertation

2

AN EFFICIENT 3D FINITE ELEMENT PROCEDURE FOR SIMULATING WHEEL–RAIL CYCLIC CONTACT AND RATCHETING

This chapter introduced an efficient 3D FE procedure to simulate ratcheting in rails subjected to numerous load cycles. The procedure simulates a wheel rolling repeatedly over a rail section with updated stress–strain states, enabling automatically executed cyclic loading simulation given a predefined number of cycles. To ensure the accuracy of the contact modelling, the effect of meshing schemes on subsurface stress distribution was examined. In addition, the FE contact model with the selected meshing scheme, which balances accuracy and computational efficiency, was verified against the widely accepted CONTACT program. Subsequently, a NLKH steel material was used in the FE model for ratcheting simulations with up to 100 wheel-loading cycles. The rail surface and subsurface stress states were replicated under partial-slip wheel–rail rolling contact conditions with traction coefficients of 0.1, 0.25 and 0.35, respectively. The ratcheting behaviour was extensively analysed in terms of plastic deformation, contact patch evolution, and ratcheting rates. The simulated plastic deformation was found to alter the contact geometry and thus contact stresses, which in turn affect further accumulation of plastic deformation and subsequent ratcheting strains. These findings highlighted the importance of considering the interplay between the rail ratcheting behaviour of the rail and evolving contact conditions for predicting ratcheting and and RCF damage in rails.

This chapter has been published in Tribology International **volume 198**, 109878 (2024) [84].

2.1. INTRODUCTION

Railway rails suffer from HC, a typical form of RCF that could lead to serious accidents [1]. The direct cause of HC has been attributed to the ratcheting induced by the wheel–rail contact [10], [13], [52]. At the wheel–rail contact interface, the significant shear stress caused by friction yields the rail steel and thus generates plastic strain in the rail surface. In the ductile rail surface, ratcheting occurs as plastic strain accumulates with increasing load cycles [18], [85]. Cracks initiate when the ratcheting strain or accumulated plastic strain reaches a critical level [15], [86].

To effectively simulate the ratcheting behaviour in rails, two key components should be carefully treated in the modelling: material and contact. The material properties of rail steels should be capable of accumulating plastic strains through cyclic loading to exhibit ratcheting behaviour. Material properties have generally been treated either with empirical formulations obtained from twin-disc tests [15], [87] or with constitutive models that incorporate NLKH [36], [43], [88], [89]. Constitutive models have been increasingly preferred owing to their adaptability across various modelling contexts [90]–[92], particularly RCF-related FE modelling [34], [78], [93]–[95].

In terms of the wheel–rail contact modelling, early research largely used (semi-)analytical models to simulate cyclic line contact under prescribed contact stresses [13], [40], [93], [96]–[98]. The FE contact modelling has been later introduced, which is capable of handling complex contact scenarios with arbitrary geometries [72], [73], [99], nonlinear material properties [81], [100], [101], and dynamic effects [102]–[104]. However, FE models are generally computationally demanding for cyclic wheel–rail contact, especially with a large number of loading cycles. Consequently, either simplified 2D [24], [34], [81] or partial 3D FE contact models (with only a FE rail model under prescribed wheel loads) [76], [82], have been employed for ratcheting simulations. The 2D line contact solutions differ from the 3D nature of real-life wheel–rail contact, whereas the approaches with prescribed contact stresses exclude the effect of contact patch evolution [40] with the accumulation of plastic deformation, i.e. the ratcheting, on the contact stresses distribution. A 3D FE contact model that comprises both the wheel and rail bodies was recently developed for ratcheting simulations [78]. The study shows the difference between the contact solutions obtained with the 2D and 3D contact models. However, it primarily focused on the ratcheting of the rail surface from a full-slip contact between a partial wheel and a partial rail models, with less emphasis on different traction conditions and the stress–strain states along the rail depth.

This study introduces a 3D FE contact model, consisting of a complete wheel assembly and a rail section, implemented in an automated procedure for reliably and efficiently simulating wheel–rail cyclic contact loading. The procedure simulates the wheel rolling repeatedly over the rail section with updated contact geometry and stress–strain states. The simulation can be automatically executed for a predefined number of load cycles. The effect of the meshing schemes on the subsurface stress distribution was examined, and the elastic FE contact model with the selected meshing scheme that balances accuracy and computational efficiency was verified against the widely accepted CONTACT programme [68]. Subsequently, the contact solutions for continuous 100 load cycles were reproduced by employing the constitutive material model of R260 rail steel under three loading conditions, corresponding to realistic material and traction conditions

tested on the V-Track test rig at TU Delft [63]. The accumulation in plastic deformation and evolutions of the contact patch and stress distribution were then investigated to assess the influence of the traction conditions on the rail ratcheting strains and rates. The next phase of this research will validate the relevant simulation results through physical tests designed to produce HC on V-Track [51].

2.2. METHODOLOGY

This section presents the automated simulation procedure developed to execute simulations for a large number of load cycles. Subsequently, the FE wheel-rail contact model is elaborated. The theoretical background of the NLKH material model and load cases with different traction conditions used in the FE contact model are also explained.

2.2.1. SIMULATION PROCEDURE

The study developed an automated simulation procedure, shown in Figure 2.1, to efficiently simulate cyclic wheel–rail rolling contact. The FE wheel-rail contact modelling was performed using the commercial software package LS-DYNA, and the automated procedure execution and post-processing of the FE solutions were programmed using Python. Each load cycle comprises two steps and takes approximately 25 minutes (with 16 threads at a 3.7 GHz CPU overclock speed), two times more efficient than the 3D FE model reported in [101]. This efficiency is notable, considering that the model employs very fine meshes (0.05 mm) at the possible wheel–rail contact region (discussed in Sections 2.3.1 and 2.3.2).

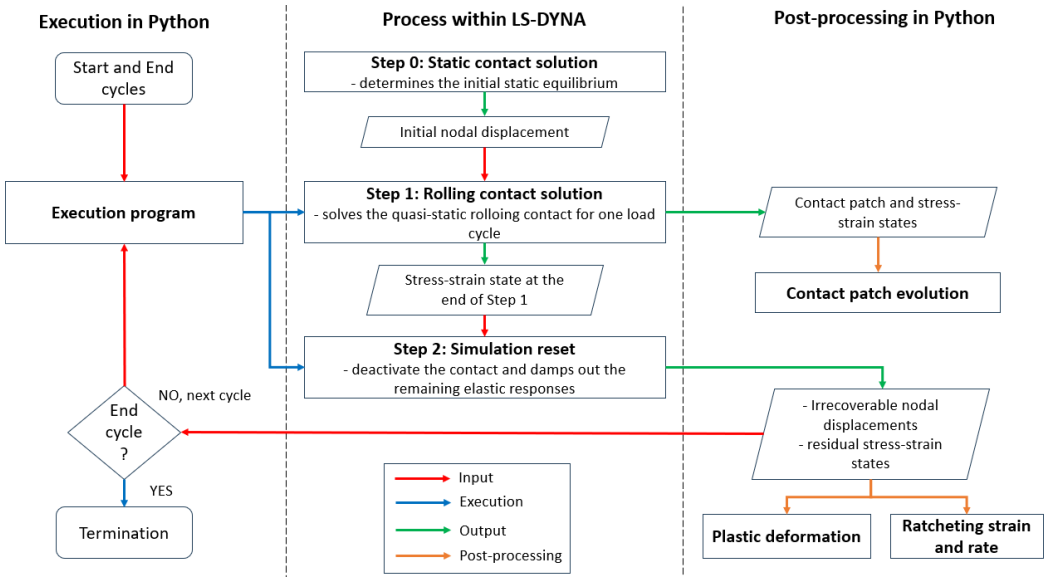

Figure 2.1: Automated simulation procedure for cyclic wheel–rail frictional rolling contact loading

As shown in Figure 2.1, each load cycle simulation comprises two steps in LS-DYNA (Step

1: Rolling contact simulation, and Step 2: Simulation reset). Before the cyclic loading simulation, the static contact was first solved to obtain the initial equilibrium position of the wheel at Step 0. With the simulation initialised at this static equilibrium position, the simulation duration for the dynamic relaxation, a process for damping out the oscillations caused by the wheel/rail initial kinematic and potential energy from the initial conditions and external loads, can be significantly shortened, enhancing the overall computational efficiency.

The rolling contact simulation can then proceed to Step 1 with a set of traction force and torque applied to achieve the desired traction condition. The FE simulation, with its finely tuned dynamic relaxation settings, can swiftly transition to steady-state rolling contact, which is then maintained to obtain the desired contact patch and stress–strain state (via post-processing with Python), as required for the RCF-related quasi-static analysis [34], [76], [78], [105]. The FE rolling contact simulation resets in Step 2 to prepare for the simulation of the next load cycle. The contact-induced wheel/rail elastic responses obtained in Step 1 are damped out, and the unrecoverable nodal displacements and residual stress–strain states are output. These serve as the initial conditions for the next-cycle rolling contact simulation (if the prescribed number of load cycle numbers has not be reached), and are used for calculating the rail plastic deformation and analysing the rail ratcheting behaviour (via post-processing with Python). The entire procedure for the wheel–rail cyclic loading simulation is automated for an arbitrary number of prescribed load cycles and terminations. It also provides flexibility for adjusting simulation parameters for each cycle, such as loading conditions and wheel speeds.

2.2.2. FE MODEL OF RAIL-WHEEL CONTACT

An FE model was built based on the wheel–rail interaction test rig V-Track [63], [106], as shown in Figure 2.2. V-Track (Figure 2.2 (a) and (b)) is developed at TU Delft to study wheel–rail contact and related problems [64], [65], [106] including HCs [51]. The contact geometries and loading conditions of the V-Track were replicated using the FE model. The FE model, comprising a wheel and a 20-mm-long rail (Figure 2.2(c)), was built using the LS-DYNA software package, widely used for rolling contact simulations [71], [73], [74]. The calculated FE contact stresses with elastic material were verified using Kalker's CONTACT [68], a boundary-element-based software that has been well acknowledged for solving steady-state rolling contact problems.

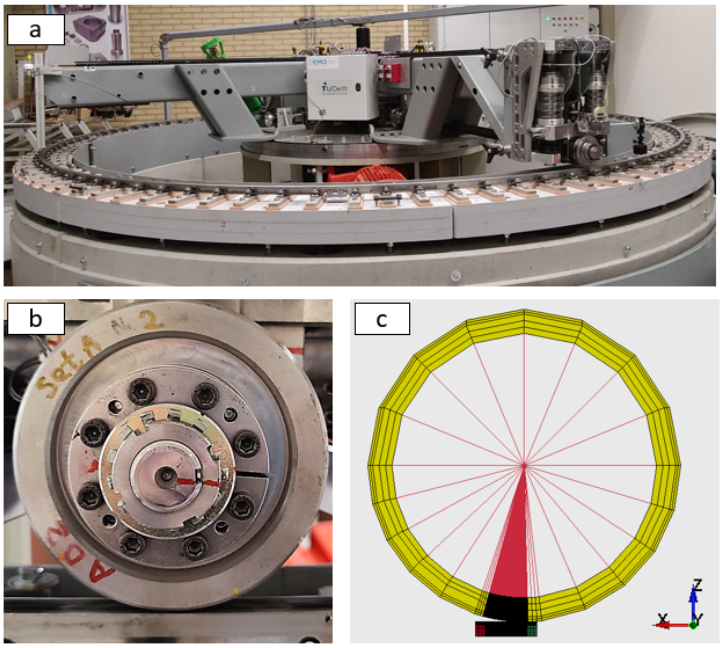

Figure 2.2: Test rig and corresponding FE model: (a) overview of the V-Track test rig, (b) close-up of the down-scaled wheel and rail, and (c) FE wheel–rail rolling contact model in LS-DYNA

To improve the computational efficiency of the FE model, the wheel was simplified to a layer of wheel tread to reduce the number of required element. The wheel tread was connected by rigid beams to a rigid rotating shaft at the centre, as shown in Figure 2.3 (a). Normal and traction forces, along with the driving torque were applied via the central rotating shaft to the contact interface. The complete circle of the wheel was retained to maintain the balance in inertia during the rolling motion. The rail was reduced to a section of rail head, and the partial model was divided into fine- and coarse-meshed regions on and beneath the rail top surface, as shown in Figures 2.3 (b) and (c), respectively. The fine mesh zones on the rail top specify the potential contact region to ensure the accuracy of the calculated contact stress and strain [71], as verified in Section 2.3.2. The fine mesh region was extended to the depth of the rail model, as shown in Figure 2.3(c), to precisely evaluate the shear stress and strain distribution in the rail subsurface [87]. This extension is crucial considering that ratcheting develops beneath the rail surface and the subsurface ratcheting strains are often assessed experimentally [15], [107]. The distributions of subsurface shear stresses calculated using different meshing schemes are compared and discussed in Section 2.3.1.

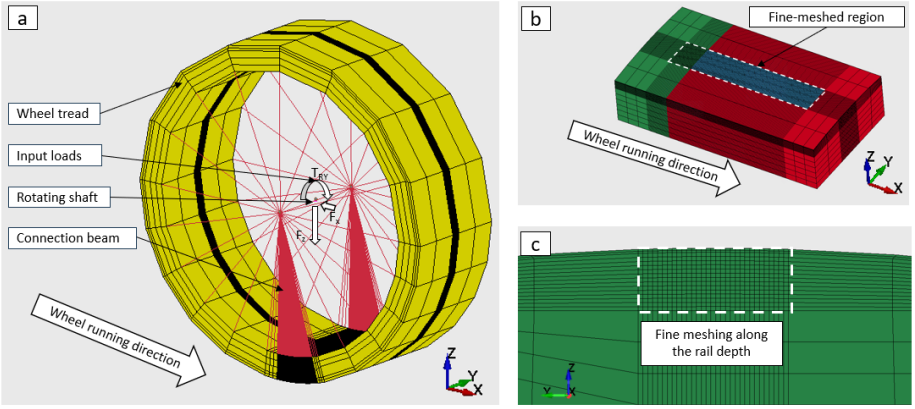

Figure 2.3: FE model in LS-DYNA, (a) details of the wheel FE model, (b) the partial rail FE model, and (c) fine meshing along the rail depth

2.2.3. MATERIAL MODEL

This study focussed on the ratcheting behaviour of the rail. Accordingly, the wheel was modelled using elastic material to reduce the computational demand. By contrast, the rail material was represented by a constitutive material model consisting of kinematic and isotropic hardening properties formulated by Chaboche [36], [43]. To consider the non-linear effects in kinematic hardening, Chaboche's formulation introduced an evanescent strain memory effect [36] in the change of the deviatoric backstress $d\boldsymbol{\alpha}$, associated with the incremental effective plastic strain, dp as

$$d\boldsymbol{\alpha} = \sum d\boldsymbol{\alpha_i} = \sum \frac{2}{3} C_i d\boldsymbol{\epsilon_p} - \gamma_i \boldsymbol{\alpha_i} dp \tag{2.1}$$

$$dp = \sqrt{\frac{2}{3}(d\boldsymbol{\epsilon_p} : d\boldsymbol{\epsilon_p})} \tag{2.2}$$

where the C_i and γ_i are the plastic modulus and constant, respectively, and $\boldsymbol{\epsilon_p}$ is the plastic strain tensor. The total back stress is the sum of several backstress terms, $d\boldsymbol{\alpha_i}$ that can be specified based on different pairs of C_i and γ_i as shown in Eq. (2.1).
For isotropic hardening or softening, the change in yield stress, R depends non-linearly on the change in effective plastic strain, dp as follows:

$$dR = b(Q - R)dp \tag{2.3}$$

where b and Q are isotropic constants that can be determined through cyclic tension–compression tests [108], [109]. The yield function incorporates both kinematic and isotropic hardening properties into the von Mises yield criterion Φ [36], [42], as follows:

$$\Phi = \sqrt{\frac{3}{2}(\boldsymbol{s} - \boldsymbol{\alpha}) : (\boldsymbol{s} - \boldsymbol{\alpha})} - (\sigma_{y_0} + R) \tag{2.4}$$

where $\boldsymbol{s}$ is the deviatoric stress tensor and σ_{y_0} is the initial yield stress.
Table 5.1 shows the material properties of R260 rail steel [110], used in the FE rail model,

considering three pairs of NLKH plastic modulus, C_i and constant γ_i (i= 1,2,3). The negative isotropic constant, Q, indicates that the R260 rail softens [39], [110] as the effective plastic strain accumulates. Isotropic softening dictates the contraction of the yield surface and tends to affect the ratcheting rate at the early stage [108], [111], whereas the kinematic hardening has a more significant influence in later cycles. The ratcheting rate converges when isotropic softening saturates and kinematic hardening stabilises [36], [112].

Table 2.1: Material properties of R260 rail steel

Variables	Value	Unit
Q	-189	MPa
b	500	-
C_1	24.7	
C_2	60.0	GPa
C_3	200.0	
γ_1	55	
γ_2	600	-
γ_3	2000	
σ_{y0}	379	MPa
E	206	GPa
v	0.3	-

2.2.4. LOAD CASES

Three load cases, LC1, LC2, and LC3, differentiated by the traction coefficient, μ, in Table 2.2, were simulated to study the influence of traction conditions on rail ratcheting. The traction coefficient is the ratio between the wheel–rail longitudinal and the vertical forces, and is bounded by the friction coefficient. The friction coefficient, f, was set to 0.4 in the study, corresponding to the dry, clean contact condition of the V-Track test rig. For each load case, the vertical force applied to the wheel was 2700 N, generating approximately 1 GPa of maximum wheel–rail contact pressure using the NLKH material.

Table 2.2: Simulated load cases and corresponding traction coefficients

Load case	LC1	LC2	LC3
traction coefficient, $\mu[-]$	0.10	0.20	0.35

2.3. RESULTS

This Section first demonstrates the accuracy and validity of the FE wheel–rail contact model by comparing the subsurface shear stress distributions across different meshing schemes and comparing the surface contact stresses calculated using the FE model and

CONTACT program. The rail ratcheting behaviour was subsequently analysed in terms of accumulated plastic deformation and contact patch evolution for up to 100 load cycles. The ratcheting strains and rates obtained from the three load cases are compared and discussed.

2.3.1. MESH EFFECTS AND MODEL SELECTION

Four mesh schemes along the depth of the rail model were compared to select an appropriate scheme for the FE ratcheting simluation. The fine-meshed region shown in Figure 2.3(c) was further divided into upper and lower parts, demarcated by dashed lines at a normalised depth of 0.1 as shown in Figure 2.5. The normalised depth is the depth under the rail surface, z, divided by the semi-axis of the wheel–rail contact area, a (in the X axis defined by the coordinate system in Figure 2.3 (a), and a = 1 mm, as shown in Figure 2.5). The FE models using the four mesh schemes were named Model 1 to 4, respectively, as shown in Figure 2.5(e). Model 1 had two layers of 0.05 mm-thick elements in the upper part of the fine-meshed region, and the element thickness in the lower part was 1 mm. For Model 2, the 0.05 mm-thickness of the element was kept uniform along the depth. The element thicknesses in the upper and lower parts of Model 3 were 0.025 and 0.1 mm, respectively. The 0.1 mm-thick elements were used in the upper and lower parts of Model 4. Model 4 and 3 had the lowest and highest computational cost.

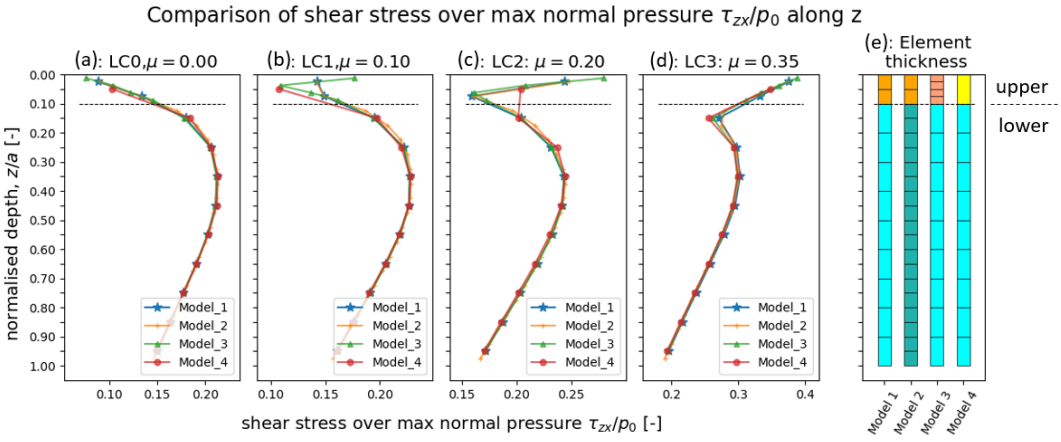

Figure 2.4: Normalised subsurface shear stress distributions calculated with different rail mesh densities and traction conditions. (a) traction coefficient μ = 0.00, (b)μ = 0.10, (c) μ = 0.20, (d) μ = 0.35, and (e) subsurface element thicknesses of the four models

Figures 2.4(a)–(d) compare the subsurface shear stress distributions normalised by the contact pressure ($\tau_{max,ZX}/p_{max}$) in the X-Z plane (coordinate system in Figure 2.3 (a)) calculated under four different traction conditions. The stress distribution is presented by the maximum shear stress under the contact patch at different depth positions. Figure 2.4(a) shows the case with zero friction force, i.e., traction coefficient $\mu = 0$, in which the four models provide similar shear stress distributions along the depth. With an increase of μ, a kink appeared in the shear stress distribution at a normalised depth of 0.05

(except Model 4) and moved downwards, as shown in Figure 2.4(b)–(d). Similar patterns in the subsurface shear stress calculations have been reported in [72], [87].
Discrepancies among the models appeared in LC1 and LC2 when the kink was located in the upper part of the fine-meshed region (normalised depth ≤ 0.1). The kink in the shear stress distribution could not be captured by Model 4 with a coarser mesh, resulting in an underestimation of the shear stress of the surface elements in Model 4, as shown in Figures 2.4(b) and (c). Figure 2.4(b) indicates that Models 1 and 2 could not fully capture the kink in LC1, however, the calculated shear stresses above and below the kink were well aligned with those of Model 3. Although Model 3 provided the most accurate solutions, its computational cost was two times higher than Model 1 and 1.6 times higher than Model 2. In addition, Model 2, with a finer mesh beneath the normalised depth of 0.1, provided relatively similar results compared with the others. Model 1 was selected for the ratcheting simulations, considering the trade-off between accuracy and computational efficiency.

2.3.2. FE MODEL VERIFICATION

The selected Model 1 was run with the elastic steel material and verified against CONTACT. The wheel–rail surface shear stresses calculated with CONTACT for LC1 – LC3 were compared with those calculated with FE Model 1 in Figure 2.5. The results indicated good agreement in the distribution and amplitude of the surface shear stresses within the contact patch. Slight deviations were caused by the intrinsic dynamic effects within the FE solutions[71], [74].

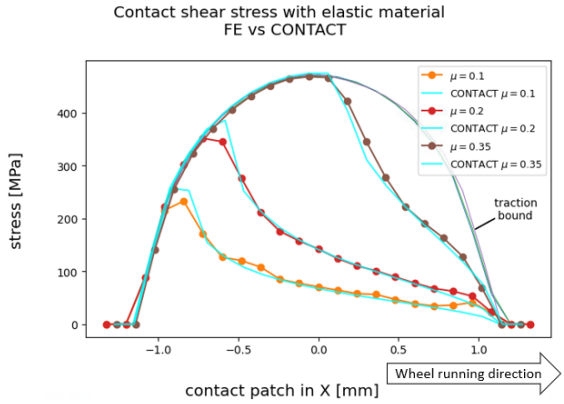

Figure 2.5: A comparison of the rail surface shear stresses calculated with FEM and CONTACT under different traction conditions

2.3.3. PLASTIC DEFORMATION

The verified model was then applied to study the plastic deformation accumulation induced by the wheel–rail contact. Figures 2.6–2.8 show the calculated results for the three load cases, LC1, LC2, and LC3, respectively. The pattern of plastic deformation accumulation is demonstrated by irrecoverable nodal displacements at the rail surface, which

can be extracted at every load cycle. In addition to the rail surface nodal displacements after the 1st load cycle, the results from load cycles 5, 35, 60, 75 and 95 are shown in Figures 2.6–2.8, and compared with those calculated after five additional cycles (i.e. from load cycles 10, 40, 65, 80 and 100). Figures 2.6–2.8 (a) and (b) show that in both the X-Y and X-Z planes, plastic deformation rapidly accumulated at the early stage (within cycle 10), after which the accumulation rate decreased, eventually stabilising with a minimal increment per cycle. For instance, the plastic deformation accumulation from load cycles 5–10 was less than that in the first five cycles and larger than that from load cycles 35 to 40.

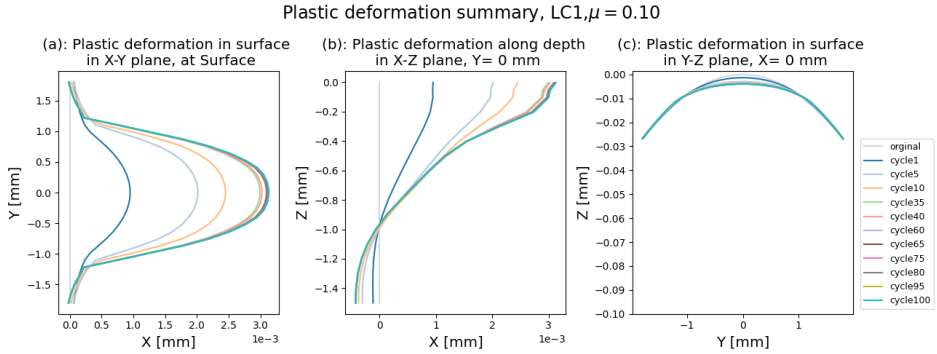

Figure 2.6: Accumulation of rail head plastic deformation for LC1 ($\mu = 0.10$): (a) in the X-Y plane, (b): in the X-Z plane, and (c): in the Y-Z plane. N.B. nodal displacement value is not on the same scale in the X and Y axes

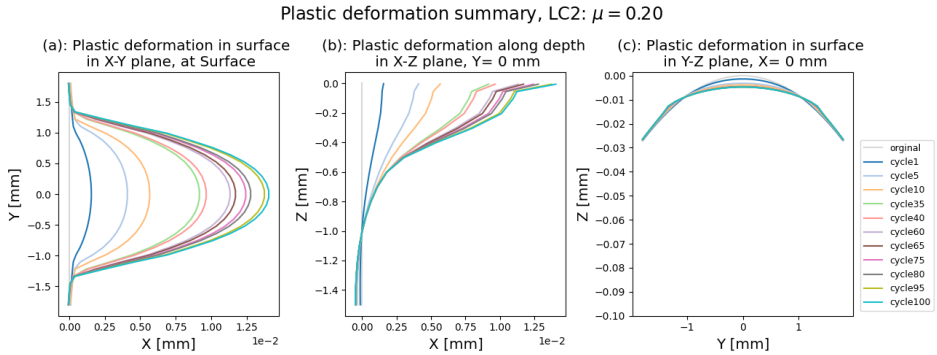

Figure 2.7: Accumulation of rail head plastic deformation for LC2 ($\mu = 0.20$): (a) in the X-Y plane, (b): in the X-Z plane, and (c): in the Y-Z plane. N.B. nodal displacement value is not on the same scale in the X and Y axes

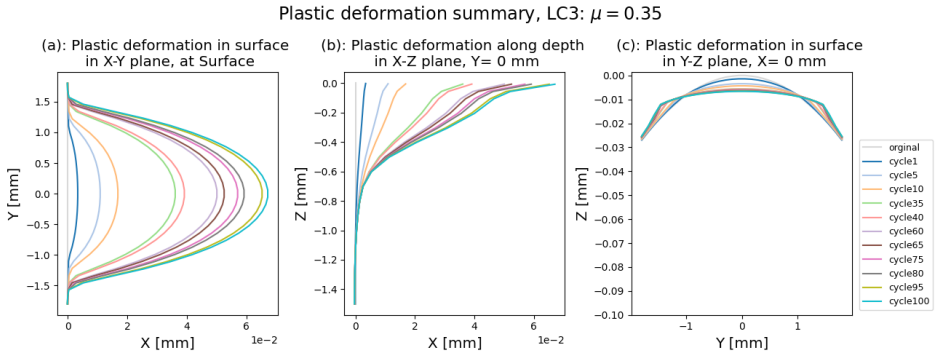

Figure 2.8: Accumulation of rail head plastic deformation for LC3 ($\mu = 0.35$): (a) in the X-Y plane, (b): in the X-Z plane, and (c): in the Y-Z plane. N.B. nodal displacement value is not on the same scale in the X and Y axes

A similar trend, albeit less significant, was observed for plastic deformation in the normal direction of the wheel–rail contact, as presented in the Y-Z plane in Figures 2.6–2.8(c). Figures 2.6–2.8(c) also indicate that the rail surface material was pushed down and outwards owing to the cyclic wheel loading. Consequently, the contact radii of the rail could increase with wheel passage. This could in turn increase the size of the contact patch and reduce contact stresses, slowing the plastic deformation accumulation.
A comparison of the results obtained from the three load cases revealed a significant influence of the traction coefficient, or shear stress, on the wheel–rail contact-induced plastic deformation. The simulated plastic deformation after 100 wheel-loading cycles for LC3 (with $\mu = 0.35$) was approximately 5 times of that for LC2 (with $\mu = 0.2$) and 20 times that for LC1 (with $\mu = 0.1$). The accumulation of plastic deformation slowed rapidly with an increase in load cycle and diminished after approximately 40 cycles when the traction coefficient was 0.1. This confirms that the occurrence of RCF can be effectively prevented by reducing the wheel–rail friction forces.

2.3.4. CONTACT PATCH EVOLUTION

The contact-induced plastic deformation in rail head affects the wheel–rail contact solutions. Figures 2.9–2.11 show the evolution of the contact patch and stress states obtained with the NLKH material model (i.e. Model 1 using the NLKH material) based on the results simulated in load cycles 1, 10, 40, 65, 80 and 100, under the three LCs, respectively. Elastic contact solutions are also provided for comparison. Higher amplitudes of the normal and shear surface stresses were obtained when the elastic material was used. In the NLKH case, the distribution of the contact pressure is less symmetrical, with the peak leaning forward, and the width of the contact patch on the X-axis was smaller. These results are consistent with those of previous studies [73], [100].

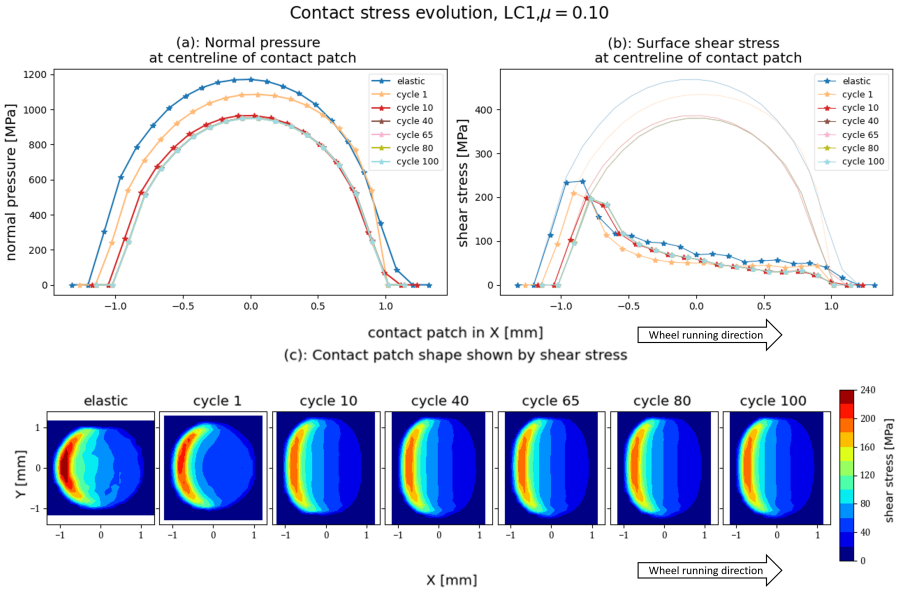

Figure 2.9: Evolution of wheel–rail contact stresses for LC1 $\mu = 0.10$: (a) the contact pressure at the centreline of the contact patch, (b)the shear stress at the centre-line of the contact patch, and (c) shear stress within the entire contact patch

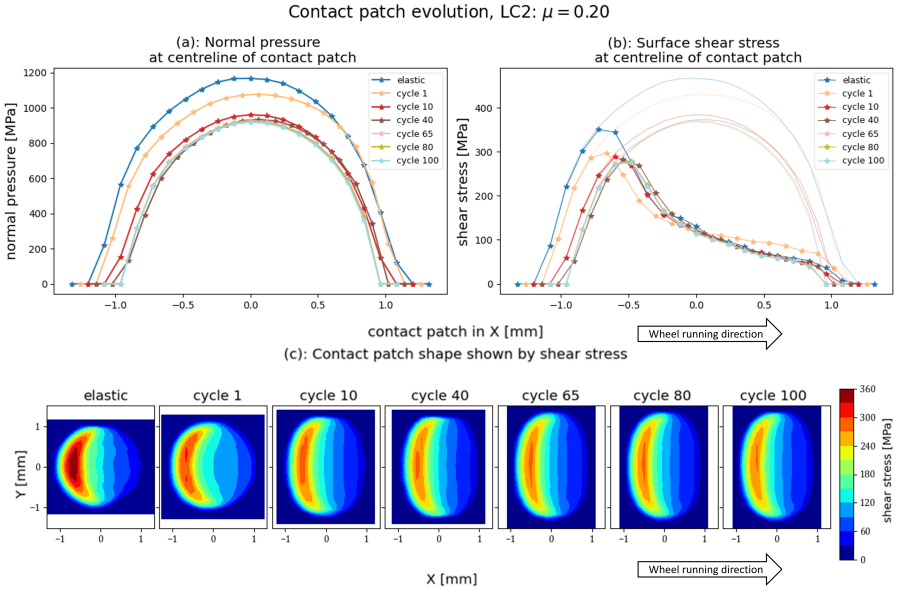

Figure 2.10: Evolution of wheel–rail contact stresses for LC1 $\mu = 0.20$: (a) the contact pressure at the centreline of the contact patch, (b)the shear stress at the centre-line of the contact patch, and (c) shear stress within the entire contact patch

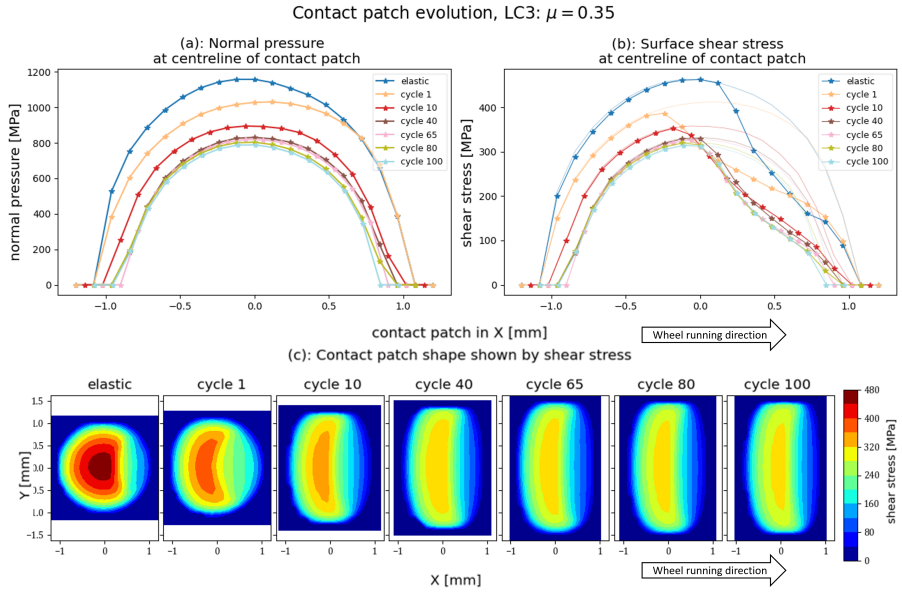

Figure 2.11: Evolution of wheel–rail contact stresses for LC1 $\mu = 0.35$: (a) the contact pressure at the centreline of the contact patch, (b)the shear stress at the centre-line of the contact patch, and (c) shear stress within the entire contact patch

The simulations were able to capture the evolution of the contact patch size at each load cycle. Figures 2.9–2.11 show that the contact patches shrank slightly along the X-axis and expanded significantly along the Y-axis with the load cycles. Contact patch expansion along the Y-axis was expected because the rail head material was pushed outwards due to the cyclic wheel loading, as presented in Figures 2.6–2.8(c), increasing the principal contact radius of the rail. Similar contact patch change patterns were observed in the RCF tests reported in [40]. Similarly, the of contact patch evolution was initially rapid and gradually stabilised with increased load cycles.

With the contact patch expansion, the magnitudes of the contact stresses (normal and shear stresses) decreased with increasing load cycles. This pattern was also followed by the stabilisation of the contact stresses after several cycles, corresponding to the change in the contact patch. The decreased contact stresses, in turn, induced less plastic deformation per load cycle until stabilisation was reached. Subsequently, changes in the stresses, plastic deformation, and contact patch size per cycle occurred at a steady but significantly smaller rate. This was observed in Figures 2.9–2.11(c) for the three load cases.

Furthermore, in LC1, the shear stress, size and shape of the contact patch remained nearly unchanged after cycle 40, resembling the shakedown effect [40], [77]. By contrast, for the other two cases, a decrease in the contact stresses was observed throughout all 100 cycles. This is because the contact shear stress induced by the low traction force in LC1 could hardly cause the rail material to yield further after 40 cycles. No significant plastic deformation accumulated in the following cycles (presented in Section 2.3.3) and

the ratcheting rate decreased to approximately zero (as shown in Section 2.3.5). The results align with field observations indicating that HC occurs more frequently on a curved track with higher wheel–rail contact shear stresses [10], [11] than on a tangent track.

2

2.3.5. RATCHETING RATE

This study further analysed the rail ratcheting behaviour by examining the simulated ratcheting strains and rates on the rail surface and beneath the surface at a depth of 150 μm, the same location as concerned in [15]. Because the actual surface ratcheting strains can hardly be measured, subsurface shear strains have often been used to indicate the intensity of ratcheting in rail [15], [98], [107]. Figures 2.12–2.14 show the results for each load case. Ratcheting was analysed in the ZX shear strains since the longitudinal wheel–rail friction forces predominantly generated contact shear stresses in this study. A common characteristic across the three different load cases was the significant decrease in ratcheting rate with the load cycles at the early stage, followed by stabilisation. Correspondingly, the ratcheting strain rapidly increased at the beginning and then increased linearly with a stabilised ratcheting rate.

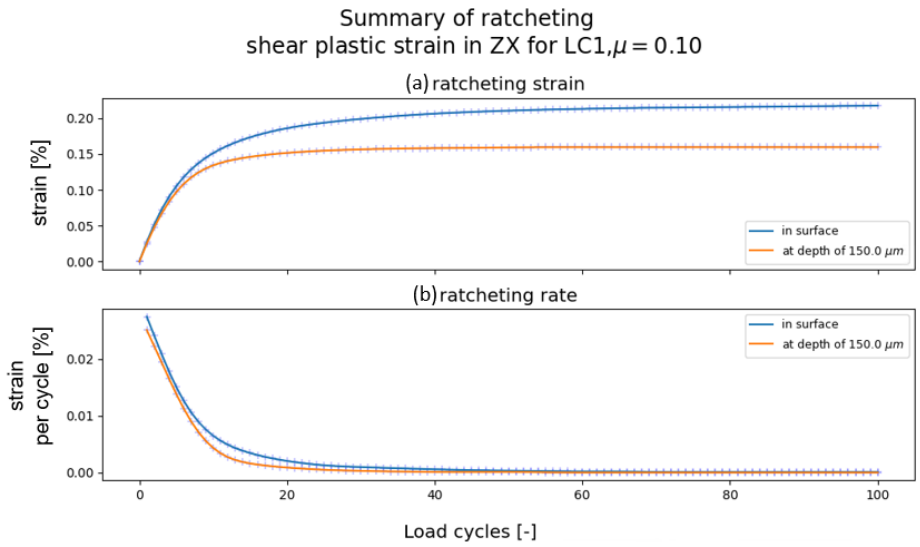

Figure 2.12: Ratcheting behaviour on and beneath the rail surface simulated for LC1 ($\mu = 0.10$): (a) ratcheting strain; (b) ratcheting rate

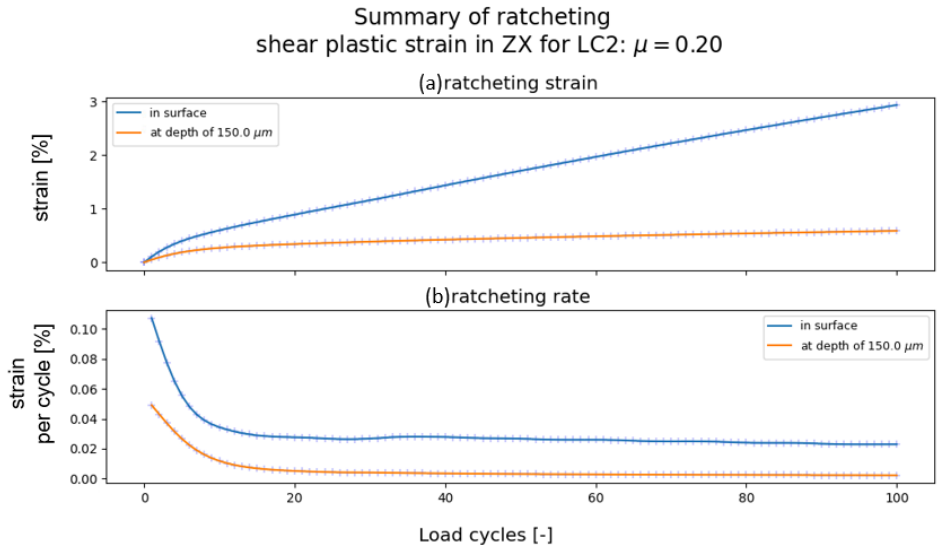

Figure 2.13: Ratcheting behaviour on and beneath the rail surface simulated for LC1 ($\mu = 0.20$): (a) ratcheting strain; (b) ratcheting rate

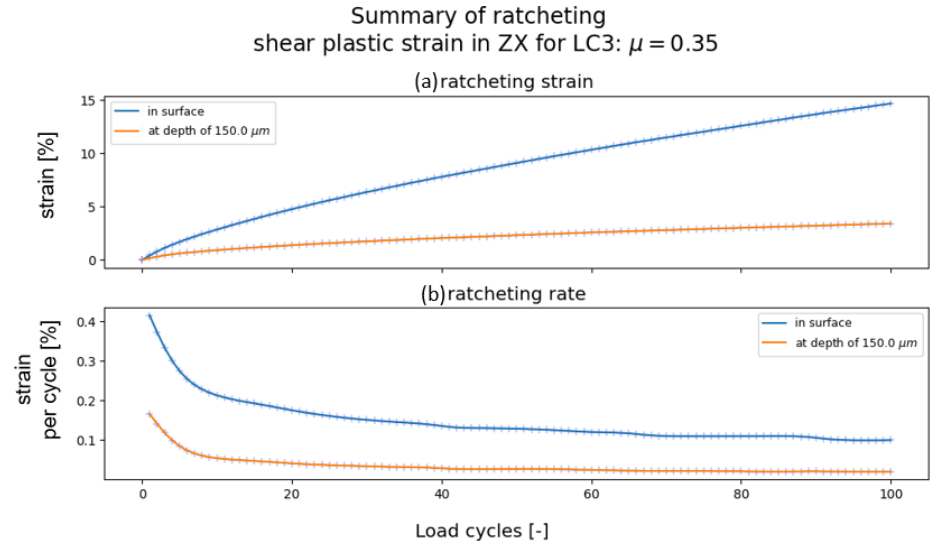

Figure 2.14: Ratcheting behaviour on and beneath the rail surface simulated for LC1 ($\mu = 0.35$): (a) ratcheting strain; (b) ratcheting rate

The magnitudes of the ratcheting rates for the same number of load cycles differ among the load cases. The simulation case with a higher traction force exhibited a significantly higher ratcheting rate at the initial stage compared with the results in Figures 2.12–2.14 (b). For LC1 with the lowest traction force and shear stresses, the converged ratcheting

rate was close to zero and no significant increase in the ratcheting strain was observed after cycle 45, as shown in Figure 2.12. The rail was effectively in a shakedown state, with no further plastic deformation accumulation [77]. This is also indicated in Figure 2.9, where the shear stress remained nearly unchanged after cycle 40. This confirms that the ratcheting behaviour can be substantially limited with a low traction coefficient under the given normal contact force.

Figures 2.12–2.14 also show the differences between the simulated ratcheting strains and rates in the rail surface and those at the subsurface with a depth of 150 μm. Higher ratcheting strains accumulated on the surface after the 100 load cycles. Notably, the gap between the surface and subsurface widened as the traction coefficient increased from 0.1 (LC1) to 0.35 (LC3). The subsurface also yielded lower ratcheting rate under stabilised conditions for LC2 and LC3. By contrast, for LC1, the ratcheting rate at both locations approached zero when the rail reached a shakedown after cycles 40 in the subsurface and 45 in the surface.

A common trend observed in the simulated plastic deformation accumulation and contact patch evolution is their rapid increase within the first few cycles , followed by slowing down and stabilisation, as discussed in Sections 2.3.3 and 2.3.4. This trend can be attributed to the ratcheting behaviour characterised by the NLKH material applied in this study. In the first few load cycles, the isotropic softening/hardening properties of the material explained in Section 2.2.3 had more significant influence on the softening process of R260 rail steel with the contraction of yield surface; thus, rapid accumulation of plastic deformation was expected. Isotropic softening tended to saturate with a relatively low effective plastic strain [108], and the kinematic hardening became more dominant in the latter cycles. The small and steady incremental change in the plastic deformation and contact patch can be atrributed to the stabilised kinematic hardening.

The ratcheting trend observed in this study is consistent with the findings of previous studies [13], [76], [83]. However, in contrast to the previous studies suggesting that the ratcheting tends to stabilise within a relatively small number of load cycles in the wheel–rail contact [76], [83], this study indicates that the ratcheting rate stabilised at a higher number of load cycles. This difference can be attributed to the interplay between the ratcheting behaviour of the rail steel presented by a NLKH material and the evolving contact patches, reproduced in this study but overlooked in previous analyses. In particular, for LC3, where the shear stress was high and the contact patch changed significantly, the ratcheting rate shows a declining trend until cycle 80 in Figure 2.14(b). This indicates the significance of considering the interplay between ratcheting behaviour and contact patch evolution for accurate rail ratcheting predictions.

2.4. CONCLUSIONS

2.4.1. CONCLUSION

This study introduced an efficient 3D FE modelling procedure for simulating rail ratcheting with a large number of wheel-loading cycles. The FE wheel–rail contact model was verified using the CONTACT program, and its meshing scheme was optimised. By applying a NLKH steel material to the FE contact model, the rail ratcheting behaviours with up to 100 partial-slip wheel passages were simulated under different traction con-

ditions. The simulated rail head plastic deformation, wheel–rail contact patch evolution, and ratcheting strains on both the rail surface and subsurface were analysed.
The results revealed that under the cyclic wheel loading the rail surface material was pushed down and outwards and deforms plastically. Consequently, the plastic deformation increased the size of the contact patch, reduced contact stresses, and slowed the plastic deformation. This indicates that the rail plastic deformation accumulation, or ratcheting behaviour, interacted with the contact patch evolution, which expanded in the lateral direction and slightly shrank in the rolling direction. This interplay between the ratcheting behaviour and contact patch evolution should be considered for accurate rail ratcheting and subsequent HC crack initiation predictions.
In addition, the results revealed the accumulation of plastic deformation, evolution of contact patch and increase of ratcheting strain are rapid at the early stage (with a small number of load cycles), and then they become slower with the increase of wheel load cycles and eventually stabilises. Moreover, the study showed that the ratcheting behaviour can be substantially influenced by the traction condition: a larger traction coefficient (0.35) induced substantially higher ratcheting strain and stabilised strain rate, in both the rail surface and subsurface, than a lower traction coefficient (0.1 or 0.2).

2.4.2. DISCUSSION AND FURTHER RESEARCH

The basic Chaboche formulation used in this study to represent the NLKH rail material may have overestimated the plastic strains under multiaxial loading conditions [38], [89], [111], typically the case for wheel–rail rolling contact. This implies that the ratcheting rate determined in this stduy may not entirely correspond to the actual HC crack initiation process. A more advanced NLKH material model can be developed and incorporated into the presented modelling procedure to further increase the accuracy of reproducing the rail ratcheting behaviour and subsequent RCF process. Furthermore, the numerical simulation results should be experimentally validated, and tests under loading conditions similar to the simulations presented in this stduy will be conducted on the V-Track test rig at TU Delft.

3

EXPERIMENTAL AND NUMERICAL INVESTIGATION INTO HEAD CHECK INITIATION ON THE V-TRACK TEST RIG

This chapter experimentally and numerically investigated wheel-rail RCF, focusing on the initiation mechanisms of HC. The experimental study was conducted using V-Track, a scaled test rig developed at TU Delft that is able to simulate real-life wheel–rail contact with controllable contact geometries and loading conditions. Ratcheting and HCs were generated on the V-Track rails with wheel–rail frictional rolling contact loading for up to 60,000 cycles. Rail samples with HCs were then examined with a microscopic analysis. The BEM and FEM were then applied to calculate wheel–rail contact-induced stress states in and below the rail surface under the same contact conditions as the experiment. The rail surface shear stresses calculated with BEM exhibit a strong correlation to the ratcheting observed within the rail running band in the microscopic analysis. Moreover, the plastic flows and cracks outside the running band identified by the microscopic analysis were correlated to the rail surface stress, especially outside the contact patch, and subsurface stresses calculated with FEM: the results suggest that the accumulation of residual stresses could also contribute to plastic flow and the consequent initiation of cracks outside the running band.

This chapter has been submitted to international journal for potential publication.

3.1. INTRODUCTION

HC, a typical type of RCF, has been a persistent issue for modern railways. The HC damage is characterised as groups of regularly spaced cracks that appear in the rail head. Once the cracks initiate, they can propagate [7], [18], leading to shelling or forced fracture of rails [19]. Grinding has been widely used as a means to control the damage, whereas its cost effectiveness remains a challenge in terms of the timing and extent of material removal or even rail replacement. Untimely or inadequate treatment of HC damage may cause substantial economic consequences and even fatal accidents [1]. To avoid these, an accurate prediction of HC crack initiation is desirable.

Multiple factors have been found to contribute to the initiation of HC. HC cracks are generally observed on curves [5], [6], [10], where lateral creep force introduced by the curving behaviour of bogie causes the shift of contact from rail top toward gauge corner. Large geometrical spin then rises when the wheel flange root with large conicity comes into contact with the rail shoulder or gauge corner. The large shear stresses induced by the lateral creep force and geometrical spin contribute to the initiation of HC[10]. Furthermore, under the cyclic loading that is essential for material fatigue problems, ratcheting, i.e. the directional plastic strain accumulation [33], occurs when the plastic shakedown limit is exceeded [13]. Cracks can initiate within the layer of plastic deformation following the direction of plastic flow [85] when the ratcheting reaches a critical level [14].

To investigate the mechanisms of RCF damage including HC, various tests have been performed to generate RCF. Twin-disc tests have been widely conducted to simulate the contact between the wheel and rail, resulting in clusters of RCF cracks [15], [16], [54], [55], [87]. The twin-disc tests offer the advantages of easy setup and control of test parameters, e.g., allowing for the adjustment of rotational velocity and alignment of the discs to control and monitor the longitudinal [54] and lateral creepage [113]. RCF cracks, HC in particular, have been successfully generated on the Voestalpine test rig [5], [9], [10] , which consists of a full-scale wheel and a 1.5-m-long straight rail in reciprocating motion with the maximum speed of 0.5 m/s [5]. This test rig can apply vertical and lateral loads on the test track without longitudinal traction force [11]. Nonetheless, the twin-disc test rigs might not properly represent the hardness of a head-hardened rail due to the ways the discs/rollers were manufactured [6], [60], while the full-scale, e.g. Voestalpine, test rigs have limitations in terms of operational speed, accurate control of wheel–rail contact loading conditions, and potentially high costs. Furthermore, none of the aforementioned test rigs can simultaneously test rail samples with different materials. It has been reported that the head-hardened rail exhibits greater resistance to RCF [5], and new rail steel materials such as bainitic steel possess improved mechanical properties [114]. To efficiently investigate the effects of material properties on RCF initiation under a large number of load cycles, a test rig capable of simultaneously testing multiple rail materials is desirable.

In this study, the V-Track test rig [63] is employed to produce HC crack initiation under controlled and monitored loading conditions. This scaled test rig is developed by the Section of Railways Engineering at TU Delft for the study of vehicle–track interaction with frictional rolling contact. Compared to the twin-disc tests, the V-Track rails, when extracted from the head-hardened real-life rails, can accurately represent the hardness

distribution in the rail head. The contact geometry can be flexibly controlled by using customised profiles of rail and wheel [106], [115]. Moreover, multiple rail steel grades can be incorporated into one setup and tested simultaneously, facilitating the study of HC crack initiation and propogation in different rail steels. Applying the same loading condition and contact geometry as in the V-Track test, this study then numerically analysed wheel–rail contact-induced stress states on the rail surface and subsurface with the BEM and the FEM. The BEM [9], [10], [68] is favoured for its rapid and accurate rolling contact solutions, but limited by the assumption of linear elasticity and cannot address the stress states beyond the contact patch. The FEM is thus employed complementarily. To investigate the mechanisms of HC initiation, the numerical solutions were then correlated to the V-Track rail cracks and plastic flow patterns observed via a microscopic analysis.

3.2. METHODOLOGY

3.2.1. HC TEST

V-TRACK TEST RIG

Figure 3.1 shows the V-Track test rig that was used to generate HC damage in this study. It features compact and lightweight rails and wheels, and is thus convenient for sample cutting for the further microscopic analysis. The scaled rails were bent to form the ring track, which is with a radius of 2 metres and supported by 100 steel sleepers. In this study, four steel grades were tested simultaneously, each spanning over 25 sleepers. The tested grades include three pearlitic steels: R220, R260MN, MHH, and one bainitic steel: B320. The grades B320 (on sleepers NO.1- 25), R220 (on sleepers NO. 26-50) and R260MN (on sleepers NO. 51-75) are naturally hard steels, while the grade MHH (on sleepers NO. 76-100) is head-hardened. The R260MN and MHH were selected due to their wide application in Dutch railways, while the inclusion of R220 and B320 aimed to examine the competing effects of RCF and wear on softer rail steel [5], [116] and to improve knowledge on the RCF resistance of bainitic steel, respectively.

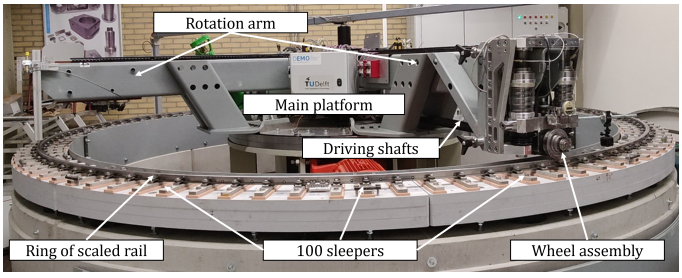

Figure 3.1: The V-Track test rig

The V-Track can accommodate four wheel assemblies for testing, each equipped with multiple sensors capable of measuring wheel/rail dynamic responses and contact forces at the wheel–rail interface. The wheel assemblies are driven by rotation arms of the main platform and can run at a speed of up to 40 km/h. The wheels can also be connected to

an actuation motor via driving shafts. The torque applied to the wheel through the driving shaft can produce traction or braking force, and thus the longitudinal creepage, at the wheel–rail interface to simulate wheel–rail contact under desired traction conditions.

CONTACT GEOMETRY

For the HC generation in this study, the wheel and rail profiles of the V-Track were carefully designed and customised to reproduce real-life wheel–rail contact geometries at locations prone to HC damage, such as the rail shoulders and gauge corners [5], [6], [11]. The wheel and rail profiles used in this study and their design process are presented in Figure 3.2. The CONTACT program [68] was used to match the contact stress conditions between the scaled and real-life contact geometries as indicated in Figure 3.2. Geometrical spin was also introduced by adopting a conical wheel profile to study its influence on the initiation of HC, as suggested by [10]. Unlike the real-life wheels with certain curved profiles (e.g. S1002), the V-Track wheels applied in this study were fabricated with constant conicity to simplify the loading condition control and to facilitate the comparison between the measurement and numerical simulation results.

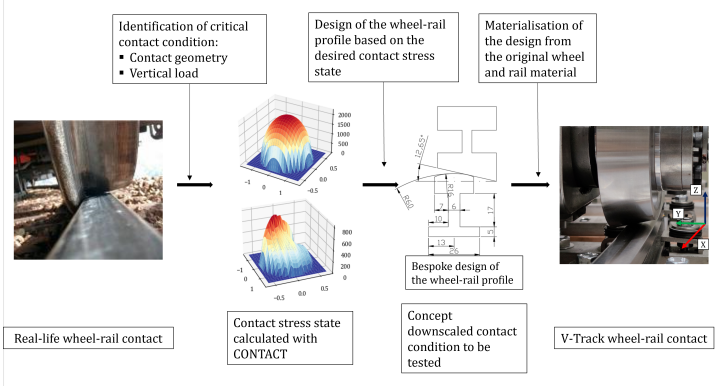

Figure 3.2: The scale wheel and rail design process for V-track

The scaled wheels and rails used in V-Track were carefully fabricated from the original materials as indicated in Figure 3.3. Figure 3.3(a) shows that scaled rails were cut at 1mm below the original rail head surface to capture the hardness close to contact interface. This practise is particularly crucial for the head-hardened MHH steel grade due to its inhomogeneously distributed hardness in rail head [6], [60]. The scaled wheels were made from the tread of the original wheel with their contact surface close to the original contact locations on tread and flange as shown in Figure 3.3(b)

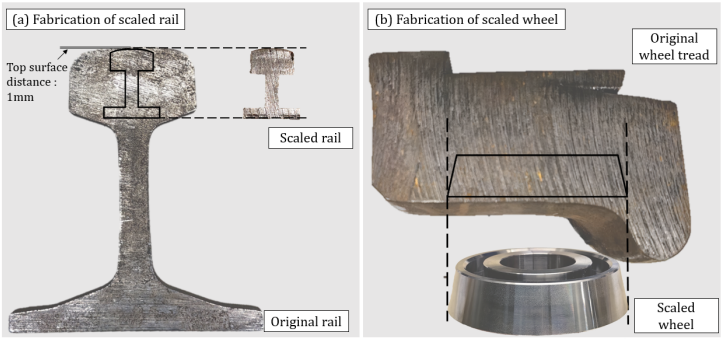

Figure 3.3: Fabrication of scale wheel and rail: (a) scaled rail from the original rail profile, and (b) scaled wheel from the original wheel tread

LOADING CONDITION

The loading conditions were also controlled to closely mimic the real-life wheel–rail contact during curving. The normal Hertzian contact stress of about 2 GPa that matches the previous research on HC initiation [11] was used in this study to produce plastic deformation and ratcheting. Based on the designed contact geometry, the vertical load of 3500N was determined. To simulate a driving wheel, a positive wheel torque was applied in the test, resulting in a steady-state traction force and an average traction coefficient (traction force over normal contact force) of 0.17, with some variation in the forces from dynamic effects (see in Figure 3.5 of Section 3.3.1). The presence of wheel conical angle ityof 12.65 degrees [11] led to geometrical spin and a lateral frictional force of about 250 N. The average coefficient of adhesion was approximately 0.22, which is the resultant friction forces (traction and lateral forces) divided by normal contact force. The measured time histories of the wheel–rail contact loads can be found in Section 3.3.1.

3.2.2. NUMERICAL ANALYSIS

Numerical analyses were performed in this study at two stages. At the first stage, a BEM analysis was performed using the CONTACT program [68] to estimate the rail surface stress state within the wheel–rail contact patch. The wheel–rail contact loads measured from the V-Track were used as the inputs for the CONTACT program. The contact patch size, magnitude of the normal and shear stresses, and orientation of the surface shear stresses can then be calculated.

Since the CONTACT program is limited by assuming linear elasticity and the solutions are constrained within the contact patch on the contact surface, FEM was employed at the second stage to investigate the stress states on the rail surface beyond the wheel–rail contact patch and beneath the rail surface with considerations of nonlinear material properties (as elaborated in Section 3.3.5). The FEM has been proven to be reliable for solving wheel–rail contact problems [71], [117] incorporating material plasticity [72], [73], [103], which is critical for the analysis of RCF.

Two FE models were built in this study to calculate the rail surface contact and subsurface stress states with its FE modelling procedure verified in [84]. The first model duplicated the conical wheel–rail contact at the V-Track test rig (see Figure 3.2) with the

same loading condition measured at sleeper NO. 72. The second model simulated the contact between a cylindrical wheel and a rail with the radius of the wheel matching the exact contact radius of the conical wheel. By comparing the results obtained with the two models, the effects of wheel conicity and consequent geometrical spin can be identified. In both FE models, the wheels were modelled with elastic material. The elastic material was first used in the rail model to identify subsurface stress patterns and verify surface contact stresses against CONTACT solutions. Subsequently, the bilinear kinematic hardening (BLKH) material was applied in the rails of both FE models to examine the distribution of (residual) stresses in the rail during and after the contact. The BLKH material was represented by an elastic part with a Young's modulus of 200 GPa and a yield stress of 500 MPa, and a plastic part with a plastic modulus of 1.4 GPa for stress values above the yield stress.

3.2.3. MICROSCOPIC ANALYSIS

Microscopic analysis was performed to examine the plastic deformation and crack initiation induced by rolling contact. The rail samples were selected following the observation of surface damage and cut from the tested R260MN steel grades from the V-Track. Since R260MN is one of the most widely used steel grades in the Netherlands, priority was given to it in our microscopic analysis of this study, with the rest of the steel grades to be processed. Two types of rail head samples were prepared: the longitudinal and transverse samples, as shown in Figure 3.4. Two longitudinal samples were cut along the wheel running direction based on the findings from surface observation (to be discussed in Section 3.3.3). The transverse sample was cut perpendicularly to the running direction. The Keyence VHX-5000 LOM was employed to first inspect the surface damage before sample preparation, and then investigate plastic deformation along the depth of rail head in the longitudinal and transverse directions in the rail samples. The two types of samples provide a comprehensive observation of plastic deformation of the rail head material, which is critical for the in-depth investigation of HC damage.

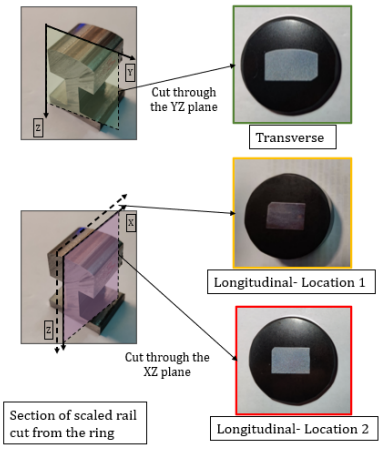

Figure 3.4: Overview of the selection of the transverse and longitudinal samples

3.3. RESULTS

3.3.1. WHEEL–RAIL CONTACT LOADS

Figure 4 shows the wheel–rail contact loads measured on the V-Track above sleepers No. 71-73 (R260MN steel) at different load cycles. The longitudinal and vertical loads and the resultant traction coefficients demonstrate good repeatability. There are some variations in the lateral forces. That can be resulted from the changes of wheel profile in the transverse direction, including the conicity, due to wear and plastic deformation under the cyclic loading.

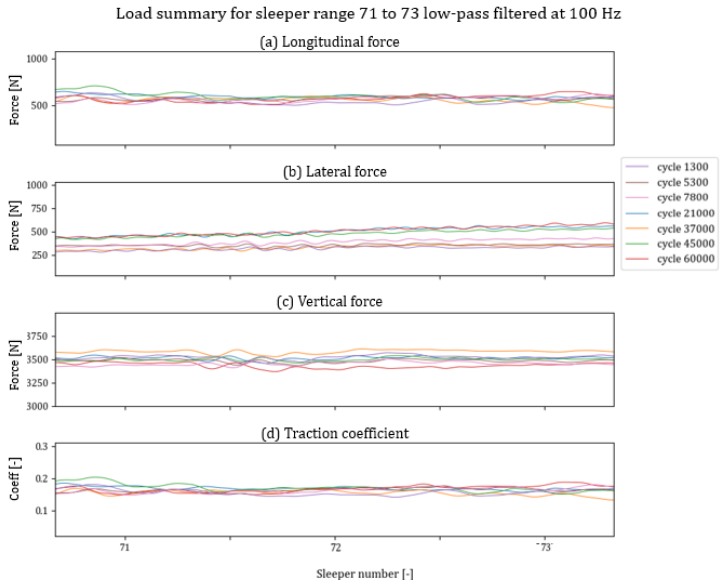

Figure 3.5: Overview of the loads measured from V-Track at different cycles: a) longitudinal force b) lateral force c) vertical force d) the traction coefficient

3.3.2. CONTACT ANALYSIS USING BEM

The measured wheel–rail contact forces and the geometric spin were then used as inputs for the CONTACT program to calculate the elastic contact solutions on the rail above the sleeper NO. 72. The steel grade at this location of interest is R260MN. The calculated elastic contact stress states inside the running band are shown in Figure 3.6. Due to the presence of geometrical spin [10], [72], the orientation of the surface shear stress exhibits a rotational pattern, as indicated in Figure 3.6(b). In addition, because a positive torque was applied to the wheel to simulate a traction loading case, the longitudinal components of the surface shear stress orientate to the opposite direction of the running direction of the wheel.

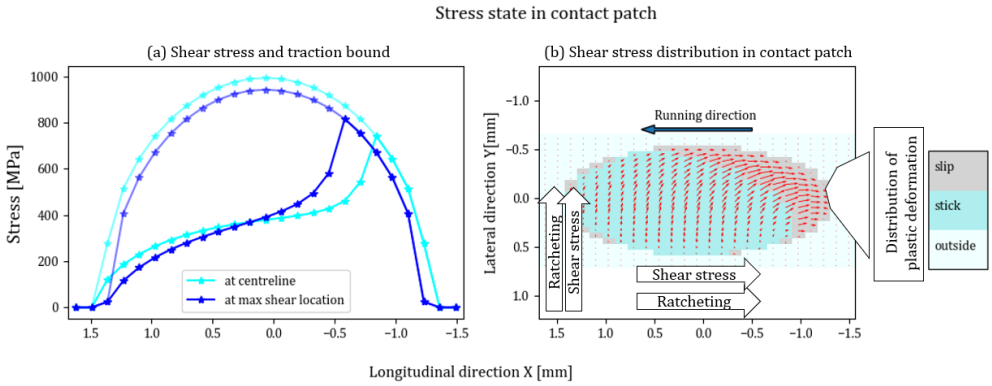

Figure 3.6: Contact analysis results and predictions of ratcheting: a) shear stress magnitude in the contact patch determined by CONTACT b) orientation of the shear stress within the contact patch and ratcheting patterns predicted based on the shear stress.

Although the elastic contact stress state cannot be used to accurately predict plastic deformation and ratcheting, it can provide valuable insights into a potential ratcheting pattern within the running band, as depicted in Figure 3.6(b). The ratcheting, as a consequence of contact-induced plastic flow, is expected to be produced following the directions of contact shear stresses, because the contact shear stresses are the key components in the deviatoric stresses [36], [42] that governs the plastic flow in wheel–rail contact [13]. Notably, as the longitudinal component of the shears stress is opposite to the running direction of the wheel, ratcheting is expected to orientate against the wheel running direction. The plastic deformation in the lateral direction is anticipated to orient to the right when observing along the running direction. In addition, more plastic deformation can be expected to accumulate on the right side of the running band where the shear stress magnitudes are higher. This anticipated distribution of the plastic deformation accumulated in rail is depicted on the right in Figure 3.6(b). The corresponding experimental results of the ratcheting and plastic deformation will be presented in Section 3.3.4 through a microscopic analysis.

3.3.3. RAIL SURFACE OBSERVATION

A visual inspection was conducted to identify the possible damage on the rail surface and to decide the locations to cut rail samples for the subsequent microscopic analysis. Surface damage was found to emerge in the form of cracks and visible irregularities after about 10,000 load cycles. Upon termination of the test at 60,000 cycles, significant surface damage was observed on the R260MN rail, as shown in Figure 3.7. Zooming in on the surface damage under LOM(Figure 3.7(b), we can observe two distinctive zones with the surface damage: Zone 1, within the yellow rectangle frame in Figure 3.7, exhibited notable surface irregularities with a wobbly pattern; and Zone 2, within the red rectangle frame, can be identified as a flatter and more reflective surface than that in Zone 1. Cracks were observed in both zones. The microscopic analysis presented in the next section focused on two longitudinal samples respectively at these two zones in the ZX plane and a transverse sample covering both zones in YZ plane per Figure 3.4.

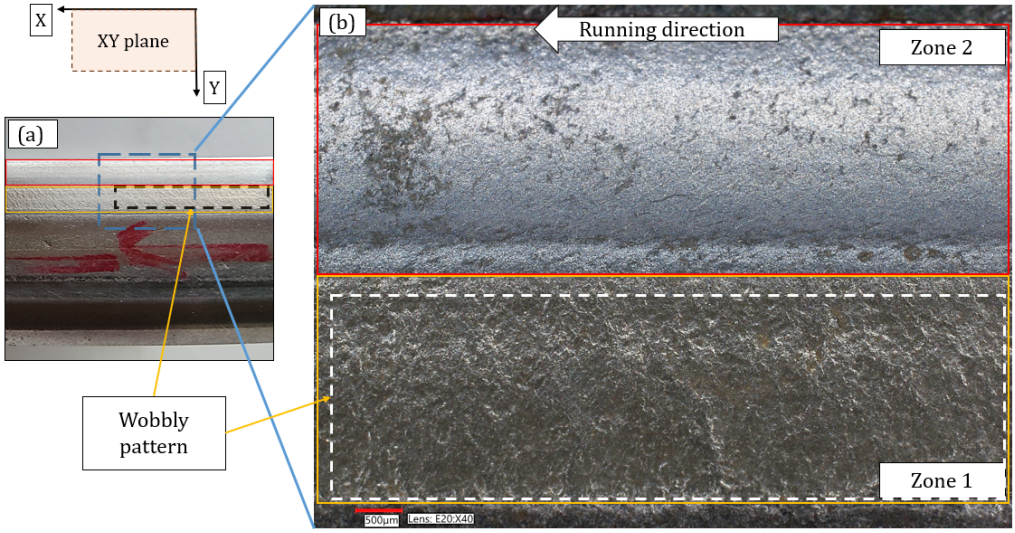

Figure 3.7: Identified Zone 1 and Zone 2 from the surface observation, a) the observed surface damage b) the microscopic view of the surface damage to identify the Zone 1 and Zone 2

3.3.4. MICROSCOPIC ANALYSIS

The plastic flow observed from a longitudinal rail sample cut at the centreline of Zone 1 is shown in Figure 3.8. It can be seen that the plastic flow direction aligns with the wheel running direction. This contradicts the elastic wheel–rail contact solutions presented in Section 3.3.2 predicting that ratcheting opposes the wheel running direction. The reason is that Zone 1 is out of the rail running band (i.e. no wheel–rail contact occurs here), to be explained later. In the plastically deformed layer that is shallower than 150 μm as shown in Figure 3.8(b), surface cracks were visible and developed along the direction of plastic deformation. Furthermore, surface irregularity can be seen at the top edge of the sample, corresponding to the patterns observed in Zone 1 in Figure 3.7.

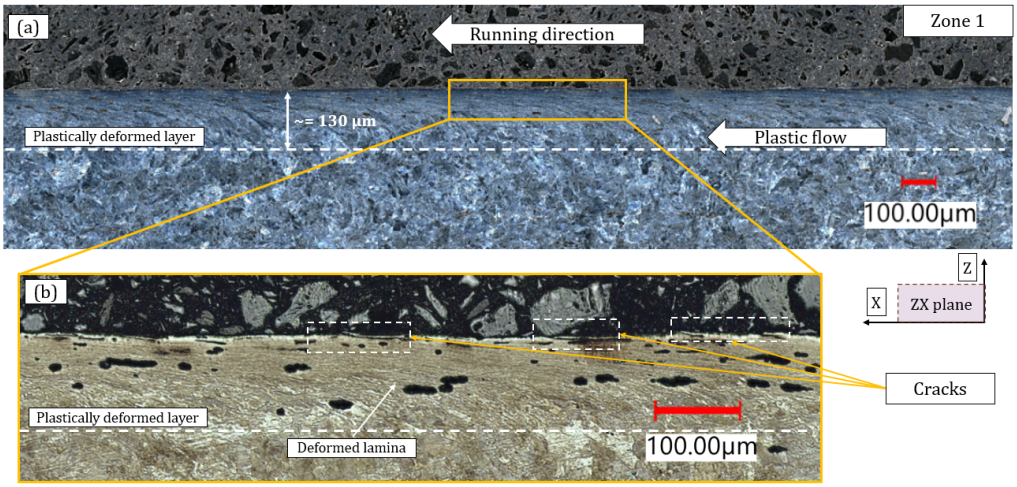

Figure 3.8: The microscopic analysis results in Zone 1 a) an over view of the plastic deformation in Zone 1 b) ta close-up view of the cracks in Zone 1

In contrast to the results observed in Zone 1, the sample from Zone 2 exhibited plastic flow opposite to the running direction, as depicted in Figure 3.9. This observation aligns with the ratcheting direction predicted based on wheel–rail contact solutions presented in Section 3.3.2. Cracks can be observed to develop also opposite to the running direction between the plastically deformed lamellae. The plastically deformed layer in Zone 2 is about 300 μm, deeper than that in Zone 1 (c.a. 130 μm), indicating that Zone 2 experienced a more severe plastic deformation due to higher shear stresses.

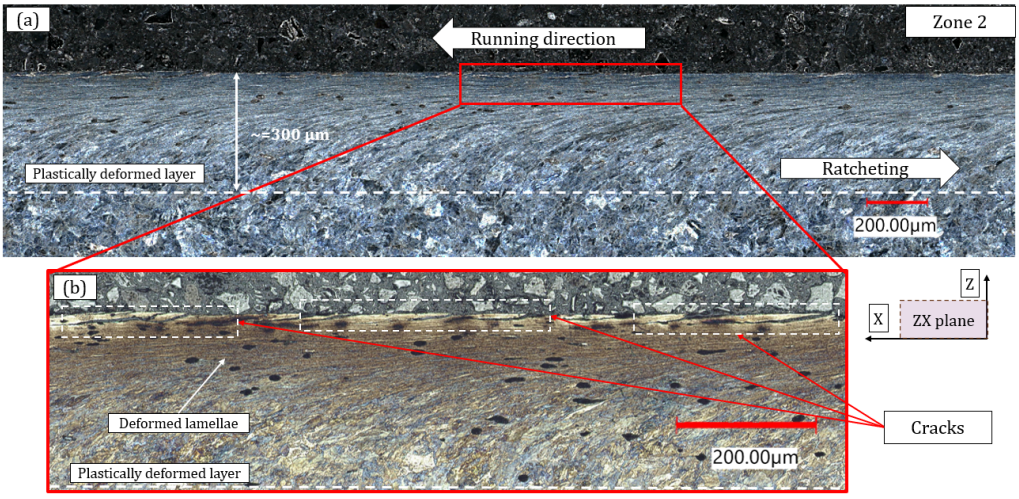

Figure 3.9: The microscopic analysis results in Zone 2 a) an overview of the plastic deformation in Zone 2 b) a close-up view of the cracks in Zone 2

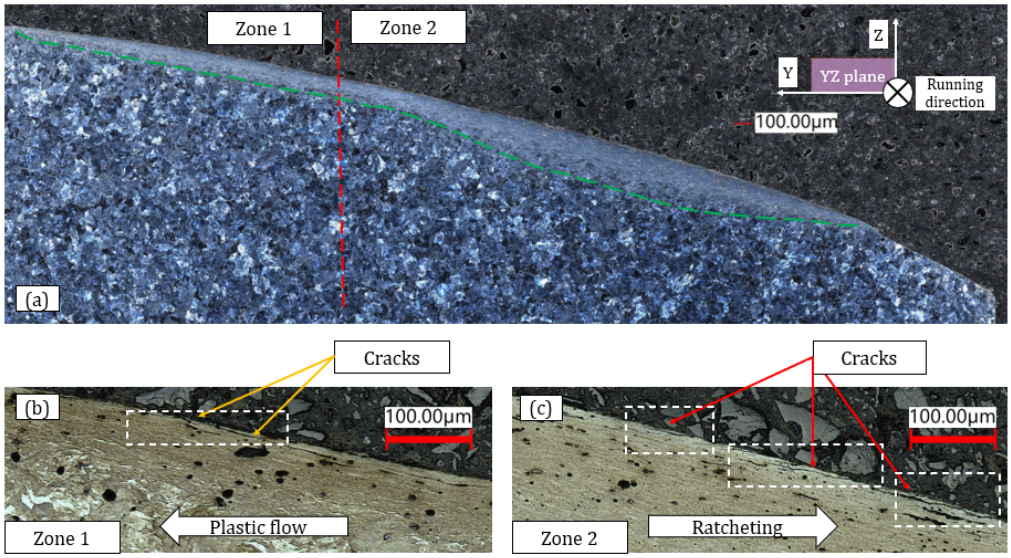

Figure 3.10: The microscopic analysis results from the transverse sample a) an overview of the range of the plastic deformation in both Zone 1 and Zone 2 b) a close-up view of Zone 1 with cracks and plastic flow c) a close-up view of Zone 2 with cracks and ratcheting

The microscopic results of the transverse sample in Zone 2 per Figure 3.10 demonstrate strong correlation with the contact solutions presented in Section 3.3.2. As shown in Figure 3.10(a), deeper plastic deformation was observed on the right side of the running band, following the running direction. This corresponds to the high shear stress region shown in Figure 3.6. The ratcheting exhibited the same orientation as the lateral component of the shear stress in the contact patch. Cracks were also visible and followed the direction of plastic deformation in the transverse sample. The layer of plastic deformation, whose region is distinguished in Figure 3.10(a) by a green dashed curve, in Zone 1 appeared shallower than that in Zone 2 (same as observed in the longitudinal samples), and looked like a 'tail' or an extension of plastic deformation in Zone 2. In addition, the analysis of the lateral sample also indicates that the plastic flow in Zone 1 exhibited a direction opposite to that in Zone 2, which is in line with the findings obtained from the longitudinal sample cuts.

The microscopic analysis results show that in Zone 2, the plastic flow orientation agrees well with the shear stress pattern obtained with BEM presented in Figure 3.6. This demonstrates that the orientations of the shear stresses within the contact patch determine the directions of plastic flow or ratcheting generated in the running band. The cracks observed in this zone are then expected to develop into HC cracks. In Zone 1, however, the plastic flow shows an opposite trend, which was not in line with the contact analysis. One possible reason is that Zone 1 was outside the running band, and the plastic deformation in Zone 1 was generated mainly by subsurface stresses, instead of surface contact stress, under the wheel–rail rolling contact. A further analysis using the FE method was conducted to examine this phenomenon, and the results are presented in the next section.

3.3.5. FEM ANALYSIS

Figure 3.11 compares the surface contact shear stress and subsurface von-Mises stresses of the elastic rail in contact with the cylindrical (Figure 3.11(a) and conical wheels (Figure 3.11(b). The YZ cross-section stresses are presented in five phases of a wheel–rail rolling contact cycle in the simulation (from left to right in Figure 3.11): before contact, at the initial contact, at the location of the maximum normal contact pressure and thus traction bound, at the location of the maximum surface shear stress, and after contact. By comparing the surface shear stresses and traction bounds solved by the FE conical contact model (the 3rd and 4th phases in Figure 3.11(b) to CONTACT solutions (see, Figure 3.6), they align well with each other in terms of amplitudes and patterns, demonstrating the accuracy of the FE model.

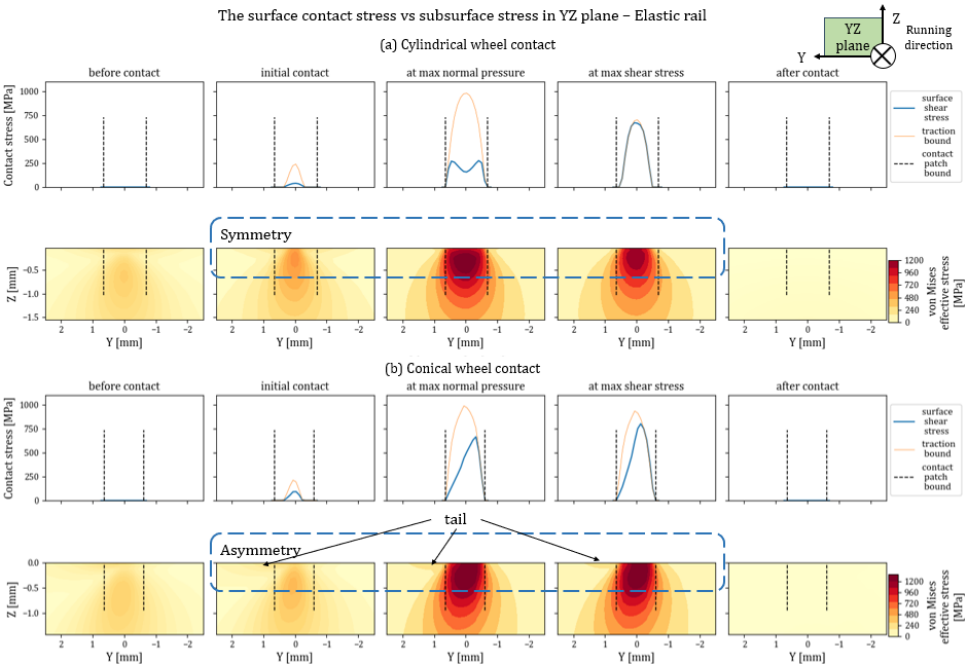

Figure 3.11: Comparison of the surface contact shear stress and subsurface von-Mises stress between cylindrical and conical wheel contacts based on elastic rail material a) the cylindrical wheel contact - without geometrical spin b) conical wheel contact - with geometrical spin

For the cylindrical wheel case, symmetrical patterns of stress distributions were observed on the surface and in the subsurface, since there was no influence of the geometrical spin. With the conical wheel contact, however, the asymmetry in the surface contact shear stress due to geometrical spin caused the asymmetric reactions of subsurface stresses as well. In Figure 3.11(b), we can see a 'tail' in the subsurface von-Mises stress outside and to the left of the contact patch during the contact (the 2nd, 3rd and 4th phases), with the running direction pointing into the paper. Notably, the location of the tail found in the FE simulation corresponds well to the location of Zone 1 observed in

the microscopic analysis, as shown in Figure 3.10. The magnitude of von-Mises stresses in this 'tail' is significantly lower than that within the contact patch, indicating a weaker effect to yield the rail material. This also corresponds to the shallower plastic deformation observed in Zone 1 in Figure 3.10.
Considering that the ultimate strengths of pearlitic rail steels are rarely above 1200 MPa [27], [29], the consideration of rail plasticity is necessary to represent a more 'realistic' situation. The von-Mises stresses obtained from the simulations of BLKH rails in contact with the cylindrical and conical wheels are presented in Figure 3.12. Compared to elastic FE contact results presented in Figure 3.11, the peak von-Mises stresses were significantly lower when the BLKH rail was used. Figure 3.12(b) shows a similar left 'tail' for the case of the conical wheel–rail contact (the 2nd, 3rd and 4th phases). Another difference lies in the stress states after the contact (the 5th phase), where we can see residual stress in the subsurface region in Figure 3.12. The difference in the distribution symmetry between the contacts with the cylindrical and conical wheels was also present for the residual von-Mises stresses.

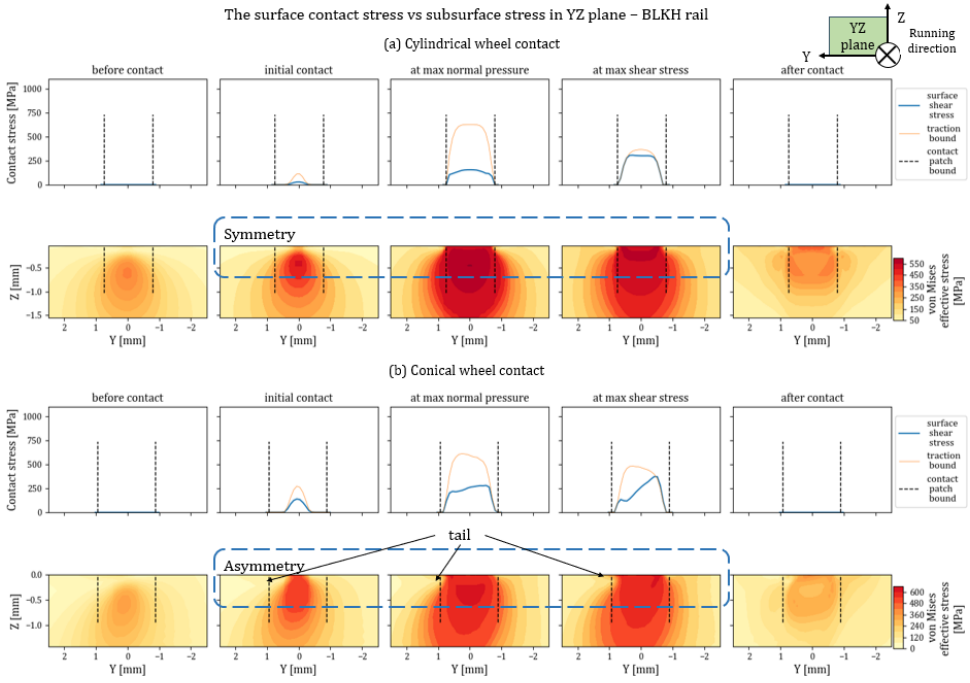

Figure 3.12: Comparison of the surface contact shear stress and subsurface von-Mises stress between cylindrical and conical wheel contacts based on BLKH rail material a) the cylindrical wheel contact - without geometrical spin b) conical wheel contact - with geometrical spin

To further investigate the changes in stresses over one contact cycle, the normal and shear stresses of the surface elements were presented in the XY plane in Figure 3.13. The stresses within the contact patch boundary in Figure 3.13, are directly induced by the surface contact stresses, whereas those outside are considered as the secondary ef-

fect as the rail responds to the rolling contact. The stresses were compared between the cylindrical and conical wheel contact cases. The cylindrical contact results (the left column) exhibited symmetric patterns with respect to the longitudinal central line, whereas asymmetry in the stress distribution was observed in the conical contact case (the right column). As shown in Figure 3.13(a), (b) and (c), the wheel–rail contact-induced compressive stress within the contact patch is much higher than that beyond. The normal stresses are predominantly compression in the X, Y, and Z directions within the contact patch indicated by the negative values; and those with positive values suggest tensile stresses outside, especially adjacent to the running band for the cylindrical contact and to the left boundary of the running band for the conical contact case. The latter corresponds well to the location of Zone 1 observed in the microscopic analysis shown in Figure 3.8(a).

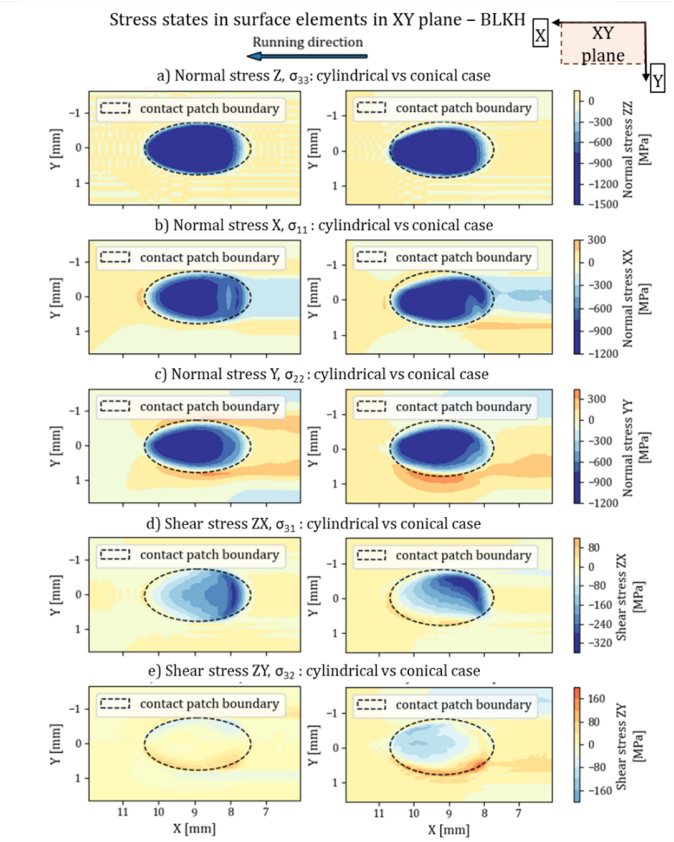

Figure 3.13: Stress states in the XY plane of the rail elements close to surface induced by the cylindrical and conical wheels : a) normal stress in Z, b) normal stress in the X direction c) normal stress in Y d) shear stress along X perpendicular to Z, and e) shear stress along Y perpendicular to Z

Furthermore, the 3 compressive normal stress components (σ_{11}, σ_{22}, σ_{33}) within the contact patch are quite close to one another in magnitude, resulting in a relatively high

hydrostatic stress, σ_p, [42], as shown in Eq.(3.2):

$$\boldsymbol{\sigma} = [\sigma_{ij}] = \begin{bmatrix} \sigma_{11} & \sigma_{12} & \sigma_{13} \\ \sigma_{21} & \sigma_{22} & \sigma_{23} \\ \sigma_{31} & \sigma_{32} & \sigma_{33} \end{bmatrix} \tag{3.1}$$

$$\sigma_p = \frac{1}{3} Tr(\boldsymbol{\sigma}) = \frac{1}{3}(\sigma_{11} + \sigma_{22} + \sigma_{33}) \tag{3.2}$$

Where $\boldsymbol{\sigma}$ is the stress tensor, $Tr(\cdot)$ is the trace of the tensor. This high hydrostatic stress diminishes the contribution of the normal stresses to the deviatoric stresses, s_{ij}, as demonstrated in Eq.(3.3), and consequently yield of the material according to von-Mises J2 criterion [36], [42] in Eq.(3.4) and (3.5):

$$s_{ij} = \sigma_{ij} - \sigma_p \delta_{ij} \tag{3.3}$$

$$f = \frac{3}{2} s_{ij} s_{ij} - \sigma_y^2 \tag{3.4}$$

$$\sigma_{vm} = \sqrt{\frac{3}{2} s_{ij} s_{ij}} = \sqrt{\frac{3}{2}[s_{11}^2 + s_{22}^2 + s_{33}^2 + 2(s_{31}^2 + s_{32}^2 + s_{12}^2)]} \tag{3.5}$$

Where the Kronecker delta $\delta_{ij} = 1$ if $i = j$, or 0 if $i \neq j$. Therefore, within the contact patch, shear stresses exert the most significant influence among the deviatoric stresses that decide the plastic flow or ratcheting. This can be further explained by the normality flow rule of constitutive plasticity theory [13], [30], [36], as shown in Eq.(3.6):

$$d\epsilon_{ij}^p = \frac{3}{2} \frac{1}{h} \langle n_{ij} d\sigma_{ij} \rangle n_{ij} \tag{3.6}$$

$$n_{ij} = \frac{\frac{\partial f}{\partial \sigma_{ij}}}{\sqrt{\frac{\partial f}{\partial \sigma_{kl}} \frac{\partial f}{\partial \sigma_{kl}}}}, \frac{\partial f}{\partial \sigma_{ij}} = \frac{\partial f}{\partial s_{ij}} \tag{3.7}$$

$$= \frac{s_{ij}}{\sqrt{s_{kl} s_{kl}}} \tag{3.8}$$

Where $d\epsilon_{ij}^p$ is the incremental plastic strain tensor, h is the scalar plastic modulus, and n_{ij} is the unit tensor of the gradient of the yield surface with respect to stress, $\partial f / \partial \sigma_{ij}$, as specified in Eq.(3.7). The Macaulay bracket $\langle \cdot \rangle$ returns 0 if the scalar $n_{ij} d\sigma_{ij}$ is negative, and therefore stipulates that plastic flow occurs only when the change in stresses aligns with the gradient of the yield function, f. Eq.(3.6) and (4.5) indicate that the deviatoric stress tensor is directly linked to the increment plastic strain tensor.

According to the plasticity theory explained above, the stress states determined from the FEM thus support our findings in Section 3.2.3 that the ratcheting and shear stress within the running band are highly correlated. In contrast, outside the contact patch, the (residual) tensile stress in the Y direction, σ_{22}, is higher in magnitude than those in the X and Z directions (σ_{11}, σ_{33}), with the latter being negligible. This disparity in the normal stresses outside the contact patch leads to a low hydrostatic stress (Eq.(3.2)), and thus elevates the weight of the X and Y normal stresses in the deviatoric stress (Eq.(3.2)) and von-Mises stress (Eq.(3.5)), whereas the influence of the shear stresses is less pronounced compared with those inside the contact patch as shown in Figure 3.13.

The asymmetry in the shear stresses displayed in Figure 3.13(d) and Figure 3.13(e) shows that higher shear stresses took place to the right of the running direction. Furthermore, the lateral friction force resulting from the wheel conicity created higher lateral shear stresses in the contact patch than that in the cylindrical contact case. For both shear stresses in the conical contact case, components in the positive X and Y axes were present close to the left boundary of the running band, again aligning with the direction of plastic deformation in Zone 1 observed in the microscopic analysis, as shown in Figures 3.8 and 3.10(b).

Although the normal and shear stresses outside the contact patch are not as high as that within the contact patch for a single load cycle, the residual normal stresses may accumulate with increasing load cycles, especially in view that during cyclic loading, plastic deformation may accumulate in the running band, changing the contact geometry, so that the stresses outside the contact patch may increase and plastic deformation may accumulate there, too. Given the substantial normal stresses occurring outside the running band over one contact cycle, the yield of the material in Zone 1 can be caused by the deviatoric components from the accumulated normal stresses combined with the shear stresses. This could explain the smaller shear strain (smaller inclination of the lamellae) and the shallower plastic deformation layer in Zone 1 compared to Zone 2 as depicted in Figure 3.8, 3.9, and 3.10(b). It is thus interesting to investigate the effects of multiple cyclic contacts in further studies.

3.4. CONCLUSION AND DISCUSSION

This study demonstrated the capability of the V-Track test rig to generate RCF-induced damage in the rail surface under controlled contact conditions. The measured wheel–rail contact forces showed good repeatability, ensuring consistent loading conditions for a large number of load cycles. The contact shear stress under the same loading condition was calculated using BEM to predict the orientation of plastic flow within the running band. Subsequently, a microscopic analysis confirms the strong correlation between the contact shear stress and ratcheting patterns in both the longitudinal and lateral directions. The decisive role of contact shear stress in ratcheting formation was further supported by the FEM analysis. Moreover, the microscopic analysis shows an opposite pattern of plastic flow outside the contact patch. The phenomenon was further investigated and explained via FE wheel–rail contact simulations incorporating plasticity in the rail material. The asymmetry distribution of the subsurface stress states during the conical wheel contact gives rise to significant normal and shear stresses beyond the running band. The directions of the stresses are opposite to those within the running band. This distribution of the normal and shear stresses indicates the possibility of material yield and plastic flow opposite to the ratcheting orientation within the running band when their residuals accumulate with the wheel–rail load cycles.

The application of the BLKH material model has demonstrated a more reasonable contact stress states for the wheel–rail contact compared to the elastic material model. The stress states determined with the FE simulations, especially using the BLKH material model, shed lights on the possible cause of the plastic flow outside the running band observed from the HC test. Nonetheless, the BLKH material model can only account for elastic shakedown, and hence is not ideal for simulating the accumulation of plastic

deformation under cyclic loading. To address this limitation, the NLKH material should be used instead for accurate simulations to study RCF initiation [18], [36]. Therefore, the next step of this study involves calibrating the rail steels used in the V-Track HC tests with constitutive material models capable of representing the NLKH behaviour of the material [36], [89]. Furthermore, the simulations of RCF should incorporate cyclic loading, e.g. following the approach outlined in [84], enabling the simulations of residual stress accumulation and further investigation into the crack initiation mechanism within and beyond the running band.

4

EXPERIMENTAL INVESTIGATION AND CONSTITUTIVE MODELLING OF THE MECHANICAL AND RATCHETING PROPERTIES IN RAIL STEELS

This chapter presented the experimental research focusing on elucidating the mechanical, hardening, and material ratcheting properties of one bainitic (B320) and two pearlitic (R220 and R260MN) rail steels. The experiment consisted of monotonic tension, uniaxial cyclic strain range, and uniaxial cyclic stress range tests. Two load cases representing the equivalent stresses experienced by rails under real-life wheel–rail contacts were used in the cyclic stress range tests to assess the rail ratcheting behaviour in railway operating conditions. The test results highlighted that the two pearlitic steels showed similar mechanical strength and ratcheting behaviour; and by contrast, the bainitic steel exhibited superior mechanical strengths and yielded significantly weaker ratcheting responses for both load cases. The study then characterised the three rail steels by calibrating for them the hardening parameters of two classical constitutive models: Chaboche and Ohno-Wang II (OWII) based on the monotonic and cyclic strain range tests. The hardening parameters of the constitutive models were then optimised based on the cyclic stress range tests to represent the material ratcheting behaviours of rail steels for each load case. Notably, the OWII model demonstrated higher precision in reproducing ratcheting strains and rates than the Chaboche model that faced limitations in simulating relatively low ratcheting rates. This study enhanced the understanding of the mechanical and ratcheting properties of the investigated rail steels and provided insights into the applicability of constitutive models for predicting and mitigating rail ratcheting effects.

4.1. INTRODUCTION

HC, a typical type of RCF, poses a persistent challenge in modern railway systems. HC originates from frictional contact at the wheel–rail interface [13], [77]. Repeated loading and unloading of wheels create cyclic contact stresses on the rails, and cause rail ratcheting, i.e. progressive accumulation of plastic strain in the rails RCF[13], [33]. When the accumulated plastic strain exceeds the ductility limit of the rail steel, cracks initiate in the severely deformed layer in the rail surface or subsurface [7], [116]. Therefore, understanding the ratcheting behaviour of rail steels is desirable for investigating HC damage in rails.

The rail ratcheting can be classified into material and structural ratcheting [33], [35]. Material ratcheting, an intrinsic elastoplastic behaviour of steels, can be observed in a cyclic tension–compression test that proportionally and homogeneously loads samples under asymmetrical stress conditions [33], [38], whereas structural ratcheting is related to the plastic strain accumulated in the non-uniformly distributed and altering stress conditions during cyclic loading. At the wheel–rail interface, the structural ratcheting is marked by the changing contact stresses as a result of evolving contact geometry in relation to the material ratcheting [84], with the material ratcheting induced by the asymmetric loading and unloading from the repeated wheel passages [76], [84], [104]. Although both ratcheting forms are significant in rail steels, this study focussed primarily on the material ratcheting, which is essential to define rail properties in the RCF-related ratcheting studies RCF [13], [15], [34], [76], [78], [79], [83], [84], [104]. Moreover, material ratcheting in rail steels, induced by the loading and unloading of contact stresses, causes the accumulation of plastic deformation in the rail surface. Consequently, the accumulation of plastic deformation alters contact profiles and causes structural ratcheting [84], which thus creates an interplay between the two ratcheting processes. Therefore, understanding the material ratcheting of rail steels is crucial as the first step towards a better understanding of the complete ratcheting effects in rails.

To accurately reproduce material ratcheting in rail steels, constitutive models that can capture the hardening processes of rail materials and characterise their elastoplastic behaviours are needed [36], [37], [41], [43], [47], [88], [118]. Most of the proposed constitutive models aimed to identify a single set of hardening parameters, to describe ratcheting behaviours across predefined general loading patterns in tension–compression tests. This approach, however, resulted in complex constitutive models, raising a concern about computational efficiency when applied to numerical cyclic contact simulations, particularly when using the FE method to simulate a large number of wheel–rail contacts [84]. Furthermore, general loading patterns in the uniaxial tension–compression tests might not align well with the specific loading and unloading patterns of the wheel–rail contact stresses in railway operating conditions. This mismatch may reduce the effectiveness of these models in approximating the ratcheting effects in the rails. To study the ratcheting effects in rails more efficiently and effectively under cyclic wheel–rail contacts, it is beneficial to calibrate well-established and less complex constitutive models such as the Chaboche and OWII models to reproduce the material ratcheting of rail steels. In addition, it is also essential to optimise their hardening parameters for specific load cases that closely resemble real-life wheel–rail contacts in railway operating conditions.

To calibrate the constitutive models for rail steels, their mechanical and hardening properties need to be identified through experimental investigations. Pearlitic rail steels have been widely used in modern railway systems, leading to numerous tests to investigate their mechanical properties and resistance to RCF [5], [9], [15], [26], [60], [119]. To improve the RCF resistance of the rails, bainitic rail steels have recently been introduced. Although it has not yet been widely applied in the field, its mechanical properties and microstructure have been evaluated in various tests and compared to pearlitic steels [22], [29], [114]. However, existing research focused mainly on RCF damage and resistance through roller-rig tests [5], [15], field observations [5], [6], and microscopic analyses [22], [26], but few experimental investigations addressed the rail material ratcheting behaviours via cyclic tension–compression tests and the subsequent analysis of their hardening characteristics, especially for bainitic rail steels. This underscores the need for more in-depth experimental investigation and constitutive modelling of the ratcheting behaviours of rail steels.

This study focused on testing, characterising, and comparing the mechanical and material ratcheting properties of two pearlitic rail steels used in the Dutch metro (R220) and railway (R260MN), along with a new bainitic rail steel (B320). The experimental investigation was conducted in three stages: monotonic tension, uniaxial cyclic strain range, and uniaxial cyclic stress range tests. The results of the former two tests formed the basis for calibrating the Chaboche and OWII constitutive models to account for the NLKH and isotropic hardening properties of the steels. The initially calibrated constitutive models were further optimised for the material ratcheting behaviours of the rail steels by considering stresses induced by real-life wheel–rail contact in railway operating conditions, in the cyclic stress range test. Finally, this study compared the results of the ratcheting simulations using the optimised constitutive models across the different rail steels.

4.2. EXPERIMENTAL INVESTIGATION

This section explained the design, load cases, and outcome of the experiment investigation. Three tests were performed sequentially at three stages: monotonic tension tests, uniaxial cyclic strain range tests, and uniaxial cyclic stress range tests, to examine the mechanical, hardening, and ratcheting properties of the rail steels of interest, respectively. The test results were also compared and discussed.

4.2.1. TEST DESIGN AND LOAD CASE

The chemical compositions of the rail steels tested in this study are detailed in Table 4.1. Test samples of these rails were carefully fabricated from the real-life rail head, as illustrated in Figure 4.1(a), aligning with the material properties close to the rail top surface, where wheel–rail contact predominantly occurs. The dimensions of the test samples are detailed in Figure 4.1(b). The uniaxial tension–compression tests were conducted on a specialised in-house fatigue test machine with a 100 kN gripping capacity, capable of delivering up to 60 kN of both tension and compression forces. An MTS axial dynamic extensometer was used to measure the axial strain up to 20%.

Table 4.1: Chemical composition of the three rail steels. Information of R220 and R260MN is from batch specification, and B320 from [22]

Steel grade	C [%]	Si [%]	Mn [%]	P [%]	S [%]	Al [%]	Cr [%]	Cu [%]	Mo [%]	Ni [%]
R220	0.58	0.26	1.03	0.013	0.024	0.001	0.03	0.01	0.003	0.003
R260MN	0.65	0.31	1.39	0.010	0.012	0.001	0.03			0.020
B320	0.13-0.27	1.00-1.50	1.35-1.75	≤ 0.025	≤ 0.025	≤ 0.004	0.30-0.70	≤ 0.15	0.10-0.30	≤ 0.100

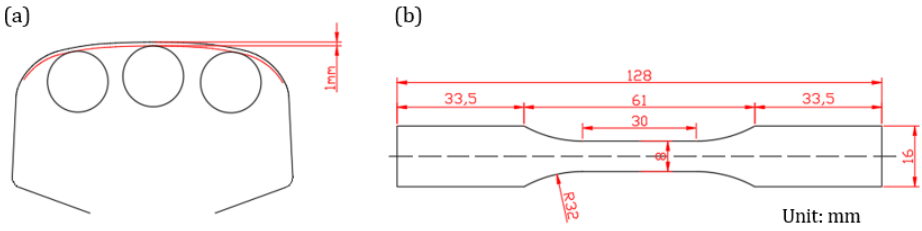

Figure 4.1: Design of the test sample: (a) the location of sample cutting from the original rail profile, and (b) dimension of the samples

The experiment investigation was conducted at three stages, with the tests and processes outlined in Figure 4.2. At stage 1, the samples were loaded monotonically in tension until fracture to obtain mechanical properties, including Young's modulus E, the 0.2%-offset yield strength (OYS) R_y, the ultimate strength Rm , and toughness (area under the stress – strain curve, see Figure 4.3). The tests were performed at least three times per rail steel to account for variations in these parameters. Elastic limits were also obtained at the upper boundary of the elastic range within the stress-strain curve. Elastic limits are generally lower than OYS and applied as yield stresses σ_y in constitutive models [36], [47] to accurately capture the elastic response of the material (as demonstrated in 4.3)).

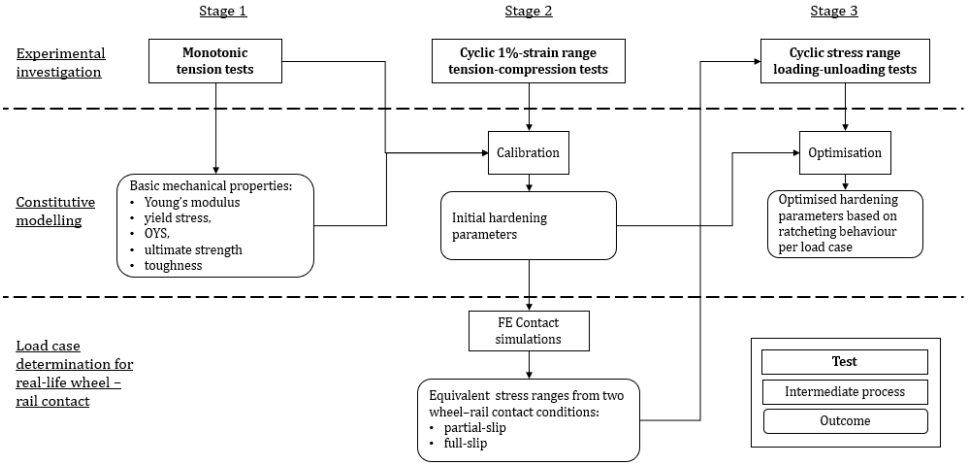

Figure 4.2: Overview of the experimental investigation at three stages, the consititutive modelling and the outcomes

At stage 2, cyclic tests with a symmetric loading pattern were performed within a ±1% strain range at a strain rate of 0.1 $\%s^{-1}$. Each sample was tested for 100 cycles with the isotropic hardening saturated and kinematic hardening stabilised in plastic shakedown [33], [39](theoretical background and explanation in Sections 4.3 and 4.4.1). Based on the results of the stabilised cycle and the monotonic tension test, the initial NLKH and isotropic hardening parameters of constitutive models can be calibrated for the rail steels [38] (presented in Sections 4.3 and 4.4). In addition, to determine the load cases for the cyclic stress range test at stage 3, i.e. the stress ranges that may induce rail ratcheting behaviours in real-life railway operating conditions, wheel–rail contact simulations were performed using an FE model [84] with the initial calibrated hardening parameters, as indicated in Figure 4.2. Two load cases were determined to represent partial- and full-slip contact conditions, respectively, for all three rails, as to be elaborated in Section 4.4.3.

Cyclic stress range tests were performed at stage 3 in which the samples were loaded and unloaded over 300 cycles. The two load cases LC1 and LC2 are presented in Table 4.2. The load cases comprise peak and residual stresses indicating the stress levels when the samples are loaded and unloaded. LC2 has larger stress ranges (peak minus residual stress) than LC1 and higher level of means stresses as shown in Table 4.2. The loading-unloading patterns result in mean stresses of the asymmetrical stress ranges that can induce material ratcheting behaviour of the rail steels [33], [38]. The analysis at this stage facilitated the optimisation of the hardening parameters obtained from stage 2, based on wheel-rail contact simulations, to closely capture the material ratcheting behaviour of the rail steels, which were elaborated in Section 4.5.

Table 4.2: Summary of load cases for cyclic stress ranges tests of Stage 3

Load case	Steel grade	R220	R260MN	B320
LC1	peak stress - loaded [MPa]	570.0	617.0	880.0
	residual stress - unloaded [MPa]	70.0	30.0	83.0
	mean stress [MPa]	320.0	323.5	481.5
LC2	peak stress - loaded [MPa]	770.0	820.0	1015.0
	residual stress - unloaded [MPa]	25.0	20.0	125.0
	mean stress [MPa]	397.5	420.0	570.0

4.2.2. MONOTONIC TENSION TEST

The results of the monotonic tension test conducted on the three rail steels are shown in Figure 4.3 with the elastic limits (σ_y),OYS's (R_y), ultimate strengths (R_m) and fracture point indicated. The results show that among the rail steels tested, B320 has the highest OYS and ultimate strength of 870 MPa and 1288 MPa, respectively. This aligns with the results reported in [22] that B320 has a much higher mechanical strength than R260 (similar to R260MN [27]). B320 also shows higher toughness than the two tested pearlitic steels. The mechanical properties obtained from the tests are summarised in Table 4.3, shown as mean values of the parameters with upper and lower bounds indicated in ± mean value.

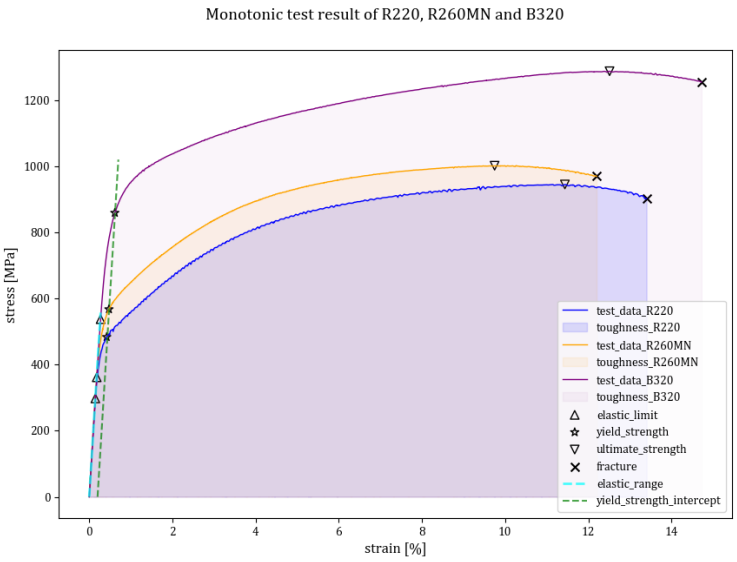

Figure 4.3: Monotonic behaviour of the tested rail steels (shown with the median values from the tests)

Table 4.3: Summary of the mechanical properties of the tested rail steels (average value provided)

Steel grade	Young's modulus $[GPa]$	Elastic limit $[MPa]$	Yield strength $[MPa]$	Ultimate strength $[MPa]$	Toughness $[MJm^{-3}]$
R220	200	290 ± 25	512 ± 22	946 ± 15	118 ± 15
R260MN	198	348 ± 20	568 ± 25	1022 ± 10	125 ± 12
B320	196	538 ± 35	870 ± 20	1288 ± 12	180 ± 30

4.2.3. CYCLIC STRAIN RANGE TEST

The strain range test results at the 100th stabilised load cycle of the three rail steels are presented in Figure 4.4. Figure 4.4(a) shows that the total strains fell within the $\pm$ 1% strain range required for the tests. Figure 4.4(b) indicates that B320 can achieve a high stress level of approximately $\pm$ 918 MPa within a relatively low plastic strain range of about $\pm$ 0.55%. This remarkable performance can be attributed to its superior mechanical strength, e.g. the high yield strength. In contrast, the R220 and R260MN steels behaved similarly with higher plastic strains at lower stress levels compared to B320. R260MN, with a stress level of 607 MPa and a plastic strain of 0.69%, marginally outperformed R220, with a stress level of 575 MPa at 0.71% plastic strain.

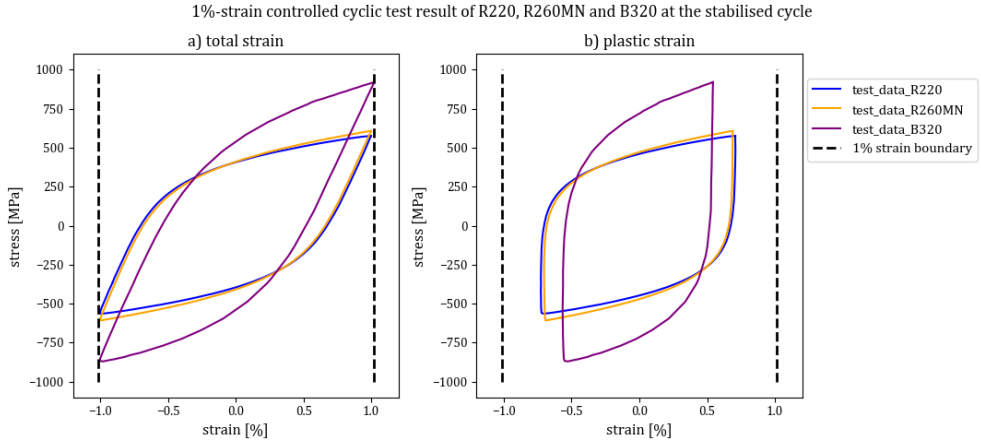

Figure 4.4: 1% cyclic test results of the R220, R260MN and B320 rail steels: (a) stress–total strain plot at the stabilised 100th cycle, and (b) stress–plastic strain plot at the stabilised 100th cycle

4.2.4. CYCLIC STRESS RANGE TEST

Figure 5 presents the cyclic stress range test results for LC1. Among the three rail steels tested, R220 reached the highest ratcheting strain in the first cycle as shown in Figures 4.5(a), with both R220 and R260MN registering a total strain exceeding 1%. In contrast, B320 achieved a considerably lower strain of around 0.5% in the first cycle, despite being subjected to a higher stress level. Subsequent cycles reveal further ratcheting strain accumulation in R220 and R260MN, as shown in Figure 4.5(b), while B320 demonstrated limited accumulation. Overall, the ratcheting effects in LC1 were relatively modest for all three steels, with their ratcheting rates, i.e., change in ratcheting strain per cycle, rapidly reducing to very low levels, as illustrated in Figure 4.5(c). A small average ratcheting rate remains between 1.5×10^{-4}% and 2×10^{-4}% from 200 cycles on for R220 and R260MN, while that is nearly negligible about 4.24×10^{-5}% for B320. This trend is also visible in Figure 4.5(b) as the curves of ratcheting strain for R220 and R260MN still show a small upward trend after 100 cycles, whereas it is almost flat for B320 from 20th cycle on. The results indicated the behaviour of the B320 steel resembled the elastic shakedown with no plastic strain accumulated after a few cycles [13], [15], [33].

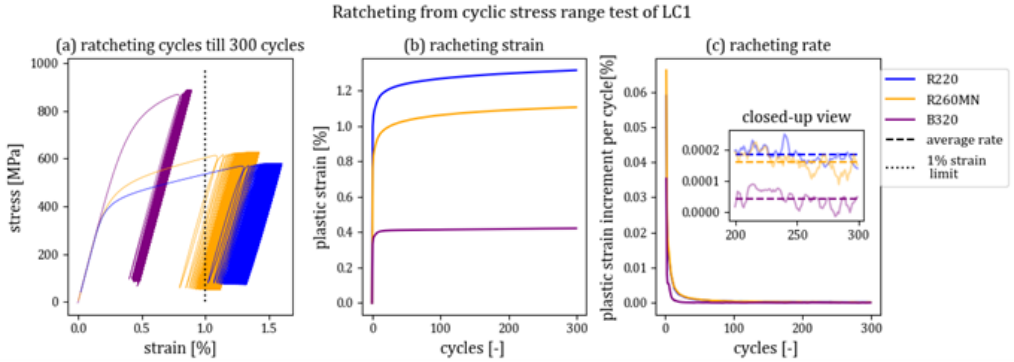

Figure 4.5: Cyclic stress range test results of the R220, R260MN and B320 rail steels for LC1: (a) stress-strain results till 300 cycles, (b) ratcheting strain plotted against load cycles, and (c) ratcheting rate plotted against load cycles

For the results of LC2 with larger stress ranges applied, more pronounced ratcheting effects can be observed. R220 and R260MN exhibited significant material ratcheting effects, as evidenced by a considerable accumulation of plastic strains, with their first-cycle plastic strain exceeding 2%, as illustrated in Figure 4.6(a). In contrast, B320 showed markedly less ratcheting effect, as shown in Figures 4.6(a) and (b), with initial and final plastic strains below 1%. When comparing ratcheting rates, R220 and R260MN stabilised at about 0. 0075% and 0. 01%, respectively, from the 200th cycle onwards, while B320 stayed at approximately 6.45×10^{-5}% after 50 cycles. The low ratcheting rate of B320 suggests that its behaviour is still close to elastic shakedown rather than fully activated ratcheting in LC2, especially considering that it endured a significantly higher stress range than the other two rail steels, as indicated in Table 4.2.

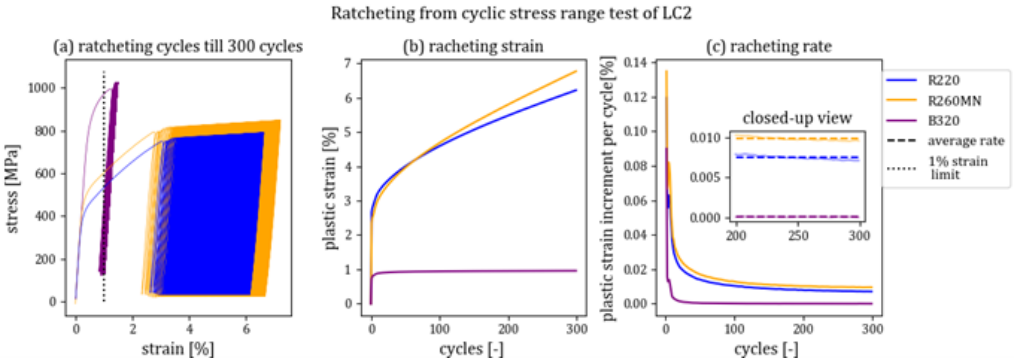

Figure 4.6: Cyclic stress range test results of the R220, R260MN and B320 rail steels for LC2: (a) stress-strain results till 300 cycles, (b) ratcheting strain plotted against load cycles, and (c) ratcheting rate plotted against load cycles

This experimental investigation confirmed that the bainitic B320 steel has markedly superior mechanical strength compared to the two pearlitic steels R220 and R260MN,

particularly evident in its significantly lower plastic strain at higher stress levels for both load cases. Besides its high yield strength, the subdued ratcheting behaviour could also be linked to its low plastic strain in the first load cycle. A comparison of 4.5(a) and 4.6(a) reveal that the initial strain should surpass a certain threshold, e.g. 1.5%, for significant ratcheting to occur in the following cycles. The influence of strain in the first cycle may be attributed to isotropic softening in rail steels [39], [118] that effectively reduces yield stress (as in constitutive modelling, explained in Section 4.3 and 4.4) with increasing effective plastic strain. The role of isotropic softening in the activation of material ratcheting merits further investigation.

4.3. CONSTITUTIVE MODELLING

This section provided a theoretical overview of the two constitutive models featured in this study, i.e. the Chaboche model and the OWII model, focusing on the kinematic hardening processes described by the models. The similarities and differences between the models were highlighted. Furthermore, the isotropic hardening/softening process represented by the VOCE method was also discussed and incorporated in the constitutive models.

4.3.1. NON-LINEAR KINEMATIC HARDENING

NLKH properties of the rail steels have been characterised using the Chaboche [36], [43] and OWII constitutive models [47], [89]. These models adhere to three fundamental rules: the yield criterion, the normality flow rule, and the hardening rule [41]. Both the Chaboche and OWII models employ the von-Mises yield criterion, as defined by Eq.(4.1):

$$f = \frac{3}{2}(\boldsymbol{s}-\boldsymbol{a}) : (\boldsymbol{s}-\boldsymbol{a}) - \sigma_y^2 \tag{4.1}$$

where the $\boldsymbol{s}$ is the deviatoric stress tensor, $\boldsymbol{a}$ is the backstress tensor and σ_y is the scalar yield stress. The yield function $f \geq 0$ 0 signifies that yield in material occurs, leading to the generation of plastic strain. The plastic strain,$\boldsymbol{\epsilon_p}$, is considered as part of the total strain, $\boldsymbol{\epsilon}$, which can be decomposed as shown below:

$$\boldsymbol{\epsilon} = \boldsymbol{\epsilon^e} + \boldsymbol{\epsilon^p} \tag{4.2}$$

The elastic strain,$\boldsymbol{\epsilon_e}$ in Eq.(4.2), can be directly calculated according to Hooke's Law with the stiffness tensor, $\boldsymbol{C}$ multiplied by the stress tensor, $\boldsymbol{\sigma}$ [120] as shown in Eq.(4.2).

$$\boldsymbol{\epsilon^e} = \boldsymbol{C\sigma} \tag{4.3}$$

The plastic strain should be determined according to the normality flow rule [36], [41] which requires that the change in plastic strains follows the gradient of the yield surface with respect to the change in stress as per Eq.(4.4).

$$d\boldsymbol{\epsilon^p} = d\lambda \frac{\partial f}{\partial \boldsymbol{\sigma}} = \frac{3}{2}\frac{1}{h}\langle d\boldsymbol{\sigma} : \boldsymbol{n}\rangle \boldsymbol{n} \tag{4.4}$$

$$\boldsymbol{n} = \frac{\frac{\partial f}{\partial \boldsymbol{\sigma}}}{\sqrt{\frac{\partial f}{\partial \boldsymbol{\sigma}} : \frac{\partial f}{\partial \boldsymbol{\sigma}}}} \tag{4.5}$$

where $d(\cdot)$ indicates the (incremental) change of the items: $d\boldsymbol{\epsilon^p}$ is thus the incremental plastic stress tensor, $d\boldsymbol{\sigma}$ is the incremental stress tensor, and $d\lambda$ is the change in the plastic multiplier. The $\frac{\partial f}{\partial \boldsymbol{\sigma}}$ is the gradient of the yield surface. The normality flow rule can be further expanded to include the non-linear plastic modulus h, specified by the hardening rule. The $\boldsymbol{n}$ is the unit normal tensor of the gradient of the yield function according to Eq.(4.5). The Macaulay bracket, $\langle\cdot\rangle$, returns zero when the value inside is negative. Therefore, $\langle d\boldsymbol{\sigma} : \boldsymbol{n}\rangle$ stipulates that plastic strain occurs only when the change in stress aligns with the gradient of the yield function.
The hardening rule can be formulated by introducing backstress [41]. In the Chaboche model, the total backstress is the sum of several components specified by Eq.(4.6). $\boldsymbol{\epsilon_p}$ is the plastic strain tensor, and p is the scalar of effective plastic strain determined by Eq.(4.7). C_i and γ_i are the plastic modulus and the plastic strain constant for the individual component of the backstress $\boldsymbol{a_i}$. The first term of Eq.(4.6) has the same form as Prager's linear kinematic hardening [121]. The second term features the dynamic recovery in the backstress that results in the Bauschinger effect [36], [41], [43], [89]. Furthermore, by applying the consistency condition $f = df = 0$ [36], [41], the non-linear plastic modulus ,h, crucial for solving the plastic strain, can be derived as shown in Eq.(4.8).

$$d\boldsymbol{a_i} = \frac{2}{3} C_i d\boldsymbol{\epsilon_p} - \gamma_i dp\boldsymbol{a_i} \tag{4.6}$$

$$dp = \sqrt{\frac{2}{3} d\boldsymbol{\epsilon^p} : d\boldsymbol{\epsilon^p}} \tag{4.7}$$

$$h = \sum_i \left[C_i - \sqrt{\frac{3}{2}} \gamma_i \boldsymbol{n} : \boldsymbol{a_i} \right] \tag{4.8}$$

The backstresses of OWII model is shown in Eq.(4.9). The OWII model shares the same linear kinematic term with the Chaboche model. The second term in Eq.(4.9) of OWII model makes the dynamic recovery effect less active compared to the Chaboche model [89]. The control constant m_i is introduced in each backstress component to regulate the ratcheting rate. $\overline{a_i}$ is the effective backstress calculated by Eq.(4.10). $\frac{C_i}{\gamma_i}$ can be interpreted as the stabilised value of each backstress component that remains constant when the plastic strain reaches $\frac{1}{\gamma_i}$ [47]. The ratcheting rate is therefore controlled by multiplying a coefficient $\frac{\overline{a_i}}{C_i/\gamma_i}$ (≤ 1) by the dynamic recovery term with the m_i smaller to intensify or larger to abate its effect as shown in Eq.(4.9). The nonlinear plastic modulus, h can then be derived as shown in Eq.(4.11).

$$d\boldsymbol{a_i} = \frac{2}{3} C_i d\boldsymbol{\epsilon_p} - \gamma_i \left(\frac{\overline{a_i}}{C_i/\gamma_i}\right)^{m_i} \left\langle d\boldsymbol{\epsilon_p} : \frac{\boldsymbol{a_i}}{C_i/\gamma_i} \right\rangle \boldsymbol{a_i} \tag{4.9}$$

$$\overline{a_i} = \sqrt{\frac{3}{2} \boldsymbol{a_i} : \boldsymbol{a_i}} \tag{4.10}$$

$$h = \sum_i \left[C_i - \frac{3}{2} \gamma_i \left(\frac{\overline{a_i}}{C_i/\gamma_i}\right)^{m_i} \left\langle \boldsymbol{n} : \frac{\boldsymbol{a_i}}{C_i/\gamma_i} \right\rangle \boldsymbol{n} : \boldsymbol{a_i} \right] \tag{4.11}$$

The OWII model can be further simplified [41], [89] as shown in Eq.(4.12), which becomes the Chaboche model when $m = 0$ with A single m specified here for the simplified

OWII model [38]. The non-linear plastic modulus is thus simplified to Eq.(4.13). The simplified OWII is used in this study to facilitate a direct comparison with the Chaboche model. Compared to the original OWII model, the simplified model uses a higher m value to control the ratcheting effects [89].

$$d\boldsymbol{a_i} = \frac{2}{3} c_i d\boldsymbol{\epsilon_p} - \gamma_i (\frac{\overline{a_i}}{C_i/\gamma_i})^m dp\boldsymbol{a_i} \tag{4.12}$$

$$h = \sum_i \left[C_i - \sqrt{\frac{3}{2}} \gamma_i (\frac{\overline{a_i}}{C_i/\gamma_i})^m \boldsymbol{n} : \boldsymbol{a_i} \right] \tag{4.13}$$

4.3.2. ISOTROPIC HARDENING/SOFTENING

VOCE method [36], [44] are also used in the aforementioned two constitutive models to approximate the isotropic hardening/softening properties of the rail steel, which evaluates the nonlinear expansion or contraction of the yield surface in response to the accumulation in the effective plastic strain as shown in Eq.(4.14). dR is the change in the yield stress that is induced by the change in the effective plastic strain dp. R symbolises the cumulative change in the yield stress, with its upper limit defined by Q as the maximum change in yield stress when isotropic hardening or softening reaches saturation. The rate for isotropic hardening/softening saturation, is also influenced by the rate factor b [108], [109] as shown in Eq.(4.14).

$$dR = b(Q - R)dp \tag{4.14}$$

With the isotropic hardening/softening incorporated, the yield function is updated, as shown in Eq.4.15, with σ_{y0} as the initial yield stress:

$$f = \frac{3}{2}(\boldsymbol{s} - \boldsymbol{a}) : (\boldsymbol{s} - \boldsymbol{a}) - (\sigma_{y0} + R)^2 \tag{4.15}$$

4.4. INITIAL CHARACTERISATION OF RAIL STEELS

By calibrating the two constitutive models, the characterisations of the three rail steels are first discussed in this section. The initial NLKH and isotropic hardening/softening parameters for the two constitutive models were calibrated based on the test results from Stage 1 and Stage 2. The calibrated models were then used in conjunction with the normality flow rule (Eq.(4.4) to numerically simulate the stress – strain relations in Stage 1 and 2, allowing for a comparison between the simulated and test results. In addition, the initial hardening parameters were applied in contact simulations to determine the load cases for tests at Stage 3, which is also elaborated in this section.

4.4.1. MATERIAL CHARACTERISATION USING CHABOCHE MODEL

The classic Chaboche model [36], [38] with three sets of back stresses was used to characterise the rail steels. The parameters of Chaboche NLKH and isotropic hardening/softening were calibrated together in a multi-parametric non-linear least squares process as elaborated in [122], [123],, which used both the experimental data from the 100th stabilised cycle of the 1%-strain range test at Stage 2 (see in Figure 4.4), and the monotonic tension

tests at Stage 1 (see in Figure 4.3). Since the tested strain range were limited by ±1%, the ultimate strength of the steels might not be captured if only the stabilised 100th cycle of Stage 2 was used, comparing Figures 4.3 and 4.4(a). This was addressed by incorporating the monotonic test results of Stage 1 into the calibration process with the parameters for isotropic hardening/softening simultaneously identified. The calibration also used Young's moduli and the mean values of the yield stresses, shown in Table 4.3.
Figure 4.7 illustrates how the hardening parameters describe the isotropic softening and kinematic hardening processes in a monotonic test and were calibrated for the constitutive models. As plastic strain increases, isotropic softening reaches saturation and kinematic hardening becomes stabilised. The yield stress, σ_{y_0}, in the isotropic softening process can saturate to $\sigma_{y_0} + Q$ at relatively low plastic strain. The saturated yield stress, σ_y in isotropic softening is lower than the σ_{y_0}, as indicated by the dashed line in Figure 4.7, representing a scenario where no change in $\sigma_{y_0}(Q = 0)$ with increasing plastic strain. For kinematic hardening, each backstress component attains its stabilised value of $C_i/\gamma_i (i = 1,2,3)$ at the plastic strain threshold of $1/\gamma_i$, which should cover a sufficient range of the hardening process. During the calibration of the hardening parameters, the sum of the backstress components, $\sum a_i, (i = 1,2,3)$ (kinematic hardening process) plus the yield stress, σ_y (isotropic softening process) at each plastic strain level approximates the total axial stress, σ and was compared with that in the test results during the calibration process.

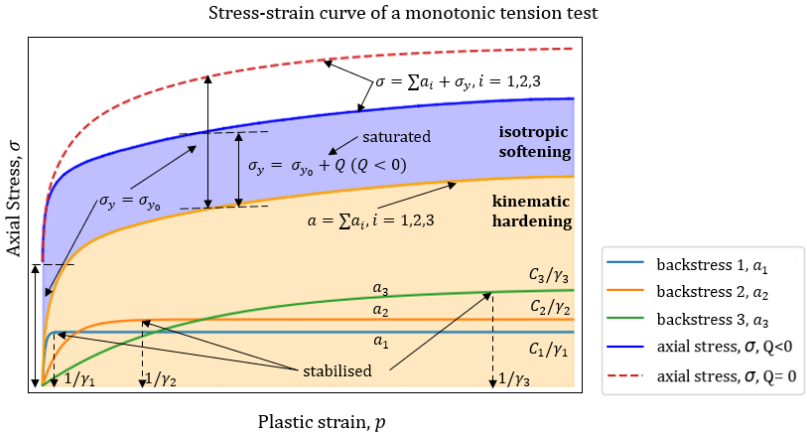

Figure 4.7: Illustration of isotropic softening and kinematic hardening processes in a montononic loaded stress–strain curve

The calibrated hardening parameters are presented in Table 4.4. Negative values of the parameter Q that determines the saturated yield stress in Eq.(4.14), indicate that the three steel rails exhibit an isotropic softening process as expected [39], [110], [118], namely the yield stress σ_y decreases with increasing equivalent plastic strain, p, until the limit $\sigma_{y0} + Q$ or saturation is reached, as illustrated in Figure 4.7. .

Table 4.4: Initially calibrated hardening parameters for the Chaboche model

Parameters	R220	R260MN	B320	Unit
C_1	511000	461000	522000	
C_2	15000	20000	70000	$[MPa]$
C_3	10500	11300	15500	
γ_1	1938	1964	2213	
γ_2	100	87	240	[-]
γ_3	27	28	36	
Q	-145	-167	-220	$[MPa]$
b	350	277	215	[-]

Relatively large values of C_3 ($\geq 10000MPa$) were selected during the calibration process as this was found beneficial for the subsequent optimisation of the hardening parameter, γ_3 (to be discussed in Section 4.5). Nevertheless, the C_3 values are limited by the values of γ_3 that should not be lower than γ_2, since $1/\gamma_i$, by definition, is the plastic strain limit for the backstress component to stabilise at C_i/γ_i, as illustrated in Figure 4.7 and discussed in Section 4.3. To use γ_3 as control constant of ratcheting, the $1/\gamma_3$ should not be too close to the tested plastic strain range, e.g. 1% (per load cycle) either as the third backstress component should not stabilise [38], [124], which also limits the value of γ_3 and thereby C_3. Furthermore, the calibration of C_3 considered the monotonic tension results in this study. It was found that a higher C_3 (basically a plastic modulus) gave a 'stiffened' response in the backstress, causing the stress calculated in the higher strain range to overshoot, as evidenced in the results of B320 (see later in Figure 4.8(b)). Consequently, it is crucial to maintain an appropriate balance between high values of C_3 and γ_3 for optimisation of ratcheting behaviour while accurately replicating the results of the monotonic tension.

The calibrated parameters were further used to simulate the strain range tests using the numerical solution of plastic strains according to Eq.(4.5) with Eq.(4.8) for Chaboche or Eq.(4.12) for OWII. The outcomes of the simulations were then evaluated against the test results from the stabilised cycle depicted in Figure 4.8. A minor discrepancy was observed between the simulated and test results, particularly in the highly non-linear part of the stress-strain curve immediately following the elastic part, where no plastic strain variation occurs with increased stress as shown in Figure 4.8(a). This discrepancy corresponds with the findings reported in [38], [109]. Additionally, the comparisons between the monotonic tension simulations and tests in Figure 4.8(b) indicated that the calibrated models achieved stress levels close to the ultimate strength. Discrepancies in B320 can be seen between the simulated and monotonic test results, attributed to the high value of C_3 as previously discussed.

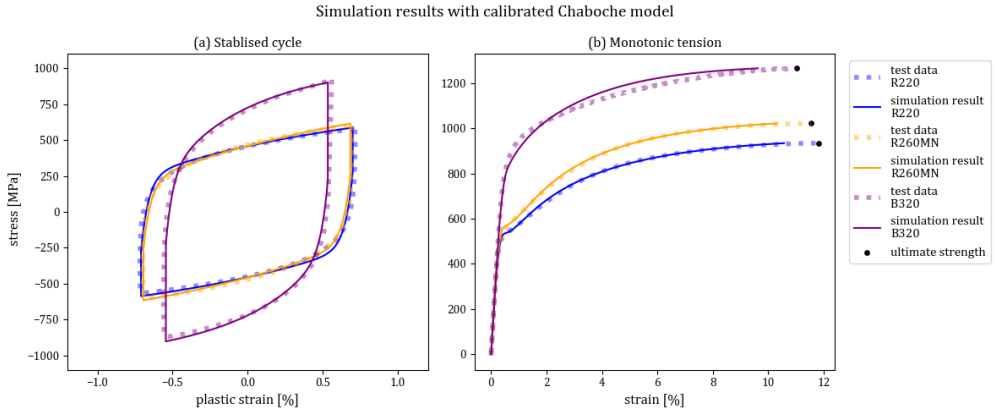

Figure 4.8: Simulation results compared with test results of the R220, R260MN and B320 rail steels based on Chaboche model: (a) the stabilised cycle of 1% strain range cyclic test, and (b) the monotonic tension test till ultimate strength

4.4.2. MATERIAL CHARACTERISATION USING OWII MODEL

The calibration of the OWII model is normally more straightforward, since hardening parameters can be directly determined from monotonic test data when the isotropic hardening/softening is not significant [38], [47]. This is usually not the case for rail steels that experience significant isotropic softening, as discussed above. Conveniently, back-stresses can be obtained by subtracting the yield stresses at each plastic strain level from the monotonic test data (indicated in Figure 4.7), since isotropic softening has already been characterised together with the Chaboche model. The remaining (ratcheting) control constant, m (Eq.(4.12)), can be determined depending on the load cases in the later optimisation process (to be discussed in Section 4.5).

Table 4.5 provides a summary of the OWII hardening parameters calibrated for the three rail steels. Different from the Chaboche model, the exponential shape of the stress–strain relation (see Figure 4.7) replicated by the OWII model (effectively a Chaboche model when $m = 0$, discussed in Section 4.3), can become multi-linear [38], [48], i.e. composing several linear sections, with a larger value of m (e.g. ≥ 1), as shown in Figure 4.9(a). Therefore, more sets of hardening parameters (C_i and γ_i) are required to closely replicate the nonlinear part of the stress–strain curve. In this study, seven sets were used to balance the computational efficiency for future FE simulations of wheel–rail contacts using constitutive models in rail material, and accuracy of reproducing the constitutive/stress–strain relation, as shown in Figure 4.9. Figure 4.9(a) shows a reasonable match between the numerical simulation results of OWII model and the strain range test results for the three rail steels. By comparing the simulation results with $m = 1$ and $m = 5$, we can see that the m value can alter the shape of the stress-strain curve in Figure 4.9(a), and change the monotonic responses in Figure 4.9(b) as a higher m value can 'stiffen' the material, resulting in a reduced strain value at higher stress levels for the steels.

Table 4.5: Initially calibrated hardening parameters for OWII model

Parameters	R220	R260MN	B320	Unit
C_1	725000	365000	800000	
C_2	76000	52000	251000	
C_3	26800	15100	53500	
C_4	8600	7000	18200	$[MPa]$
C_5	4200	5800	8000	
C_6	3800	4800	3400	
C_7	2300	2900	2600	
γ_1	5133	2850	8429	
γ_2	1175	632	1492	
γ_3	394	231	408	
γ_4	100	111	130	$[MPa]$
γ_5	47	51	74	
γ_6	25	29	29	
γ_7	13	13	13	
Q	-145	-167	-220	$[MPa]$
b	350	277	215	[-]

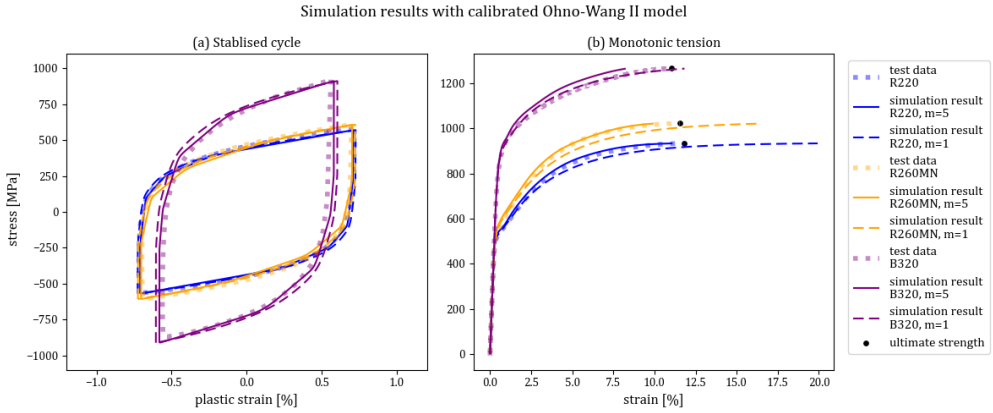

Figure 4.9: Simulation results compared with test results of the R220, R260MN and B320 rail steels based on OWII model: a) the stablised cycle of 1% strain range cyclic test, and b) the monotonic tension test till ultimate strength

4.4.3. LOAD CASE DETERMINATION FOR STRESS RANGE TESTS

Two load cases (Table 2.2) for the cyclic stress range tests at Stage 3 were determined based on two contact conditions. The stress ranges in these load cases were determined from wheel–rail contact simulations using an FE wheel–rail contact model [84], where the initially calibrated Chaboche model (Table 4.4) was applied in the rail material. The FE model duplicated the test setup of the V-track [63], [106], a scaled test rig used to reproduce real-life wheel–rail contact conditions and the consequent phenomena [51], [64], [65]. A normal load of 3500N and a traction coefficient (μ) of 0.3 were applied in

the FE model as LC1, to produce a partial-slip rolling contact condition on the V-Track for ratcheting and RCF generation [51], considering that the friction coefficient of the V-Track rail is 0.45 under a dry and clean condition. For comparison, the second load case, LC2, produced a full-slip contact condition with a traction coefficient equal to the friction coefficient, which achieves higher shear stresses and consequently a higher equivalent stress level during the contact.
Figure 4.10 illustrates the simulated contact shear stresses and traction bounds for both load cases on the rails. In Figure 4.10 (a), the adhesion and slip regions can be identified in the partial-slip contact solutions: the shear stresses are below and equal to the traction bounds in the adhesion and slip regions, respectively. Verifcaiton of the FE solution against CONTACT, widely-accepted software for rolling contact solutions[69], has been reported in [84]. In both Figure s4.10 (a) and (b), the peak pressures are not in the centre but shifts to the leading part, corresponding well to the plastic contact pressure distribution in [73].

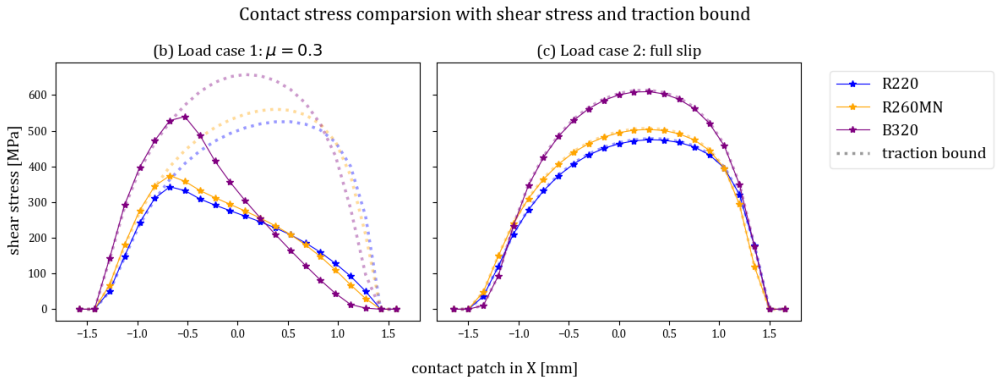

Figure 4.10: Comparison of the contact shear stresses and traction bounds for R220, R260MN and B320: (a) the results from LC1, and (b) the results from LC2

Figures 4.11 and 4.12 demonstrate how the loading pattern for the stress range tests were determined for the LC1 and LC2 in Table 2.2, respectively. The cyclic contact simulation was run to obtain the equivalent stress levels before and during rolling contact. Only two load cycles were simulated to avoid the possible influence of ratcheting that was not yet considered in the calibration of constitutive models at Stage 2. The peak equivalent stresses were obtained from the highest stress levels loaded by the contact in the first cycle. Subsequently, the residual equivalent stresses were obtained before the contact in the second cycle, representing the stress levels unloaded from contact after the first cycle. The loaded and unloaded stress levels (in Table 2.2) can then be determined as the levels of the peak and residual equivalent stresses, respectively, as indicated by the red dash-dotted lines in Figures 4.11 and 4.12. The loading patterns for cyclic stress range tests were subsequently constructed as the cyclic triangular ramp loads (solid red lines in Figures 4.11 and 4.12), which basically match the equivalent stresses induced by wheel–rail contact loading conditions. This replication of wheel–rail contact-induced stresses

facilitated testing of the rails close to railway operating conditions and comparison of the three rail steels for their ratcheting behaviours, considering the significant difference in their mechanical strengths.

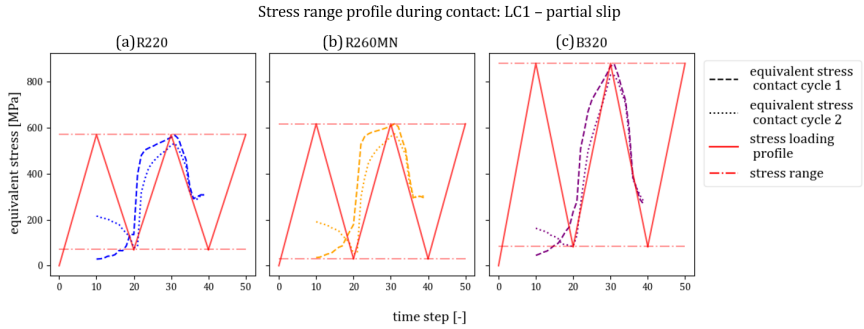

Figure 4.11: Stress ranges of LC1, determined based on the simulated equivalent stresses of two wheel-rail partial-slip contacts (a) R220, (b) R260MN, and (c) B320

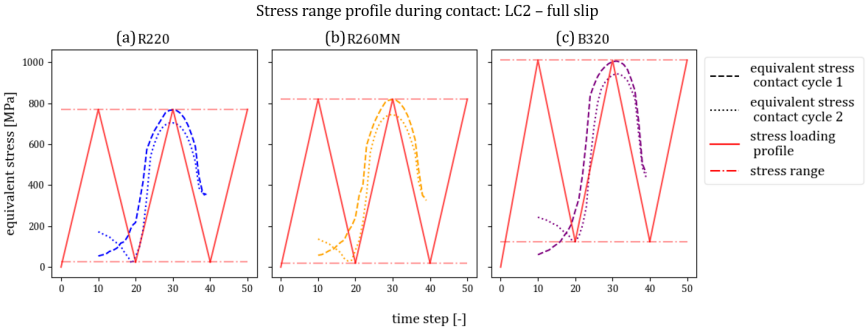

Figure 4.12: Stress ranges of LC2, determined based on the simulated equivalent stresses of two wheel-rail full-slip contacts (a) R220, (b) R260MN, and (c) B320

4.5. CONSTITUTIVE MODEL OPTIMISATION FOR RATCHETING

This section presents the optimisation process of the calibrated constitutive models for better representations of the rail material ratcheting properties. The material ratcheting behaviour of the rail steels prior to optimisation was first compared with the test results of Stage 3. Subsequently, the relevant parameters for both constitutive models were adjusted to align the calculated ratcheting strains and rates with those of the test results. Accordingly, material ratcheting behaviour simulated with the optimised constitutive models was presented and compared with the relevant/corresponding test results at Stage 3.

4.5.1. MATERIAL RATCHETING SIMULATED WITH INITIAL HARDENING PARAMETERS

Figure 4.13 compares the ratcheting strains obtained with cyclic stress range tests (shown also in Figures 4.5(b) and 4.5(b)) to the results simulated using two constitutive models, i.e. Chaboche and OWII, with the initial hardening parameters calibrated in sections 4.4.1 and 4.4.2. Here, the simulations refer to the numerical simulations that solve the plastic strains following Eq.4.5 with Eq. 4.8 for Chaboche, or Eq. 4.13 for OWII, under the same stress ranges tested at Stage 3.

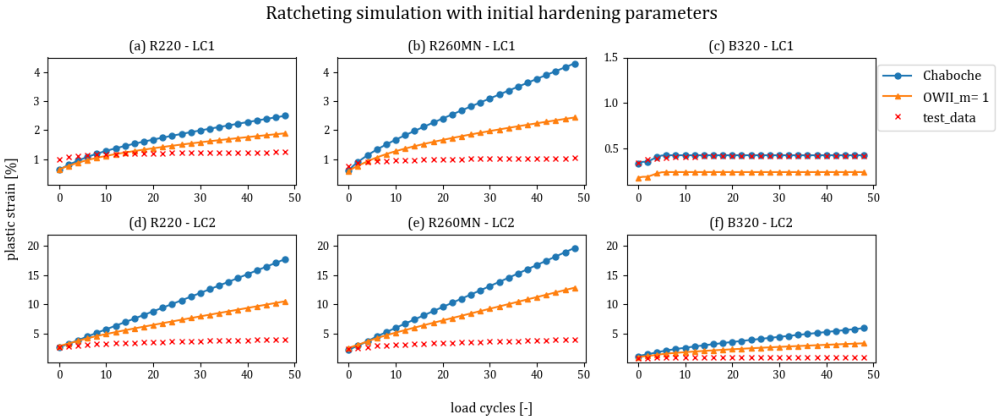

Figure 4.13: Ratcheting simulation results using the inital parameters of Chaboche and OWII ($m = 1$) compared with the test data for LC1 and LC2: (a) R220 under LC1, (b) R260MN under LC1, (c) B320 under LC1, (d) R220 under LC2, (e) R260MN under LC2, and (f) B320 under LC2

An outlier of the ratcheting strain results can be observed in Figure 4.13(c) that the B320 rail, for LC1, exhibited an elastic shakedown effect [33] during which the ratcheting rate diminished after about eight load cycles. This has been noticed in Figure 4.5 (c): the ratcheting rate was reduced to a very low level after only a few testing load cycles. In Figure 4.13(c), the ratcheting strain calculated with the Chaboche model matched closely with the test result, while the result of OWII model had a lower plastic strain level but still reached the shakedown after the eighth load cycle. This misalignment can be attributed to the ratcheting control constant, e.g., a larger m (≥ 1) that makes the material 'stiffer' and produces smaller strain values, as discussed in Section 4.4.2. Nonetheless, the difference in plastic strain was comparably small at about 0.15%.

4.5.2. OPTIMISATION OF THE CONSTITUTIVE MODELS

In the optimisation process, the relevant parameters were iterated in the numerical simulations (discussed in Section 4.4.1) of the cyclic stress range tests to match the simulated and tested ratcheting rates as suggested in [38]. The initial hardening parameter, γ_3, should be reduced for the Chaboche model [38], whereas the control constant, m, was increased for OWII model [38], [89], to reduce the simulated ratcheting rates. In this study, γ_3 or m was optimised separately for each load case, instead of looking for a sin-

gle value to work for both load cases, as this has been found difficult according to [125] (more ref!!!) and also in this study. Therefore, different values of γ_3 and m were presented for LC1 and LC2.
The optimised parameters γ_3 and m for LC1 are shown in Table 4.6. The rail steels exhibited relatively low ratcheting rates in LC1 as discussed in Section 4.2.4, which resulted in extremely low γ_3 values for the Chaboche models and relatively high m values for the OWII model, except for B320. Since the B320 was in elastic shakedown, the Chaboche parameters were unchanged. Comparisons between the tested and simulated ratcheting strains using optimised hardening parameters are presented in Figure 4.14. The parameter m for the OWII model was reduced to 0 (effectively becoming a Chaboche model) to better match the level of plastic strain of the test, as shown in Figure 4.14(c).

Table 4.6: Adjusted hardening parameter of Chaboche and control constant of OWII models for LC1

Parameters	R220	R260MN	B320
γ_3	0.0001	0.0001	36.00
m	27.00	31.00	0.00

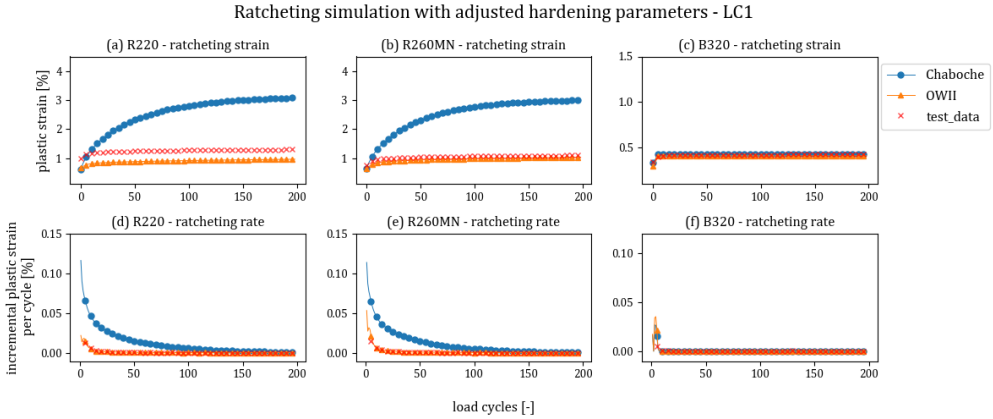

Figure 4.14: Ratcheting simulation results using the adjusted parameters of Chaboche and OWII compared with the test data for LC1: (a)-(c) the comparison of racheting strains for R220, R260MN and B320, and (d)-(f) the comparison of racheting rates for R220, R260MN and B320

Figures 4.14(a) and (b) show the simulated ratcheting strains compared with the test results for R220 and R260MN. For both rail steels, the ratcheting strains simulated with the optimised Chaboche model overshot to a level above 3% after 200 cycles, while the test results achieved strains slightly above 1%. With very small values γ_3 (= 0.0001), the simulated ratcheting rates could approach a level similar to the test results approaching 150 cycles, as shown in Figures 4.14(d) and (e). In contrast, the optimised OWII model performed better than the Chaboche model as indicated in Figures 4.14(a), (b), (d) and (e) with a close match in the ratcheting rates achieved between the simulated and test results. For the ratcheting strains, despite the initial difference in the strain level of R220

(Figure 4.14(a)), the patterns of the simulated strain accumulation were well aligned with the test results.

In contrast to R220 and R260MN, B320 steel exhibited elastic shakedown in LC1, as shown in Figures 4.14(c) and (f), owing to its high mechanical strength. The simulation results using both constitutive material models demonstrated the shakedown behaviour. Figures 4.14(c) shows that the Chaboche model with the initial calibrated hardening parameters could reproduce the matching ratcheting strains from the test without γ_3 being adjusted. The optimised OWII model can also produce the ratcheting strain pattern obtained with tests for B320 but with a small gap (about 0.05%) at the first cycle. In line with test results, the ratcheting rates calculated with the optimised models stabilised and reached zero after the first cycles, as shown in Figure 4.14(f).

The optimised parameters for LC2 are provided in Table 4.7 and the corresponding simulation results of material ratcheting behaviour are presented in Figure 4.6. For the R220 and R260MN steels, the optimised parameters γ_3 for the Chaboche model under LC2 are larger than those under LC1 , while the optimised parameters m for the OWII model are smaller under LC2. As shown in Figures 4.15(a), (b), (d) and (e), the ratcheting strains and rates simulated with the optimised models match reasonably well with the test results. The optimised OWII model performed excellently with the simulated ratcheting strains and rates both matching closely with the test results. The optimised Chaboche model also demonstrated the improved accuracy in predicting the rail ratcheting behaviour for LC2, although the ratcheting strains and rates were not precisely aligned with test results before 50 cycles.

Table 4.7: Adjusted hardening parameter of Chaboche and control constant of OWII models for LC2

Parameters	R220	R260MN	B320
γ_3	1.06	1.05	0.0001
m	10.30	9.00	85.00

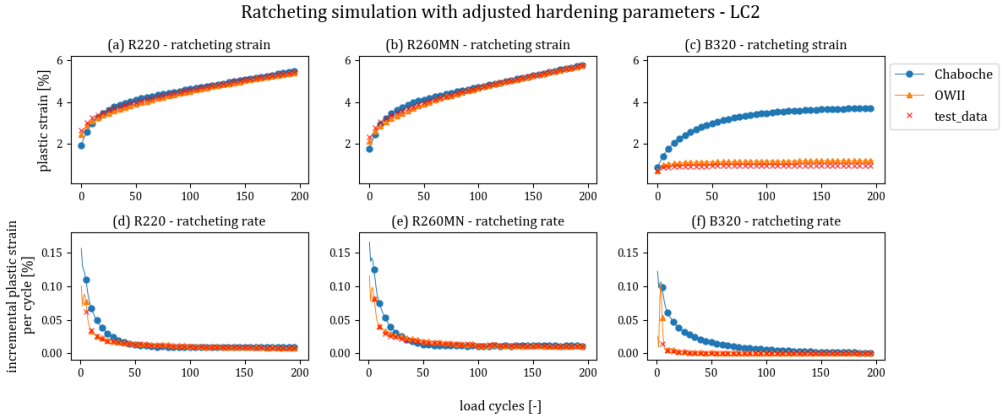

Figure 4.15: Ratcheting simulation results using the adjusted parameters of Chaboche and OWII compared with the test data for LC2: (a)-(c) the comparison of racheting strains for R220, R260MN and B320, and (d)-(f) the comparison of racheting rates for R220, R260MN and B320

The performance improvement of the Chaboche model in predicting ratcheting behaviour of R220 and R260MN can be attributed to two factors. First, the material ratcheting effects observed for R220 and R260MN steels were significantly more pronounced in LC2 than in LC1, reducing the need to lower the γ_3 values substantially to align with the ratcheting rates observed in the tests. Second, during the calibration of the initial NLKH parameters, high values were purposely selected for C_3, and consequently also for γ_3, giving more flexibility in its adjustment. Comprehensively comparing the simulation results under LC1 and LC2, it can be concluded that the Chaboche model struggled to accurately reproduce rail ratcheting behaviour with low ratcheting rates due to its relatively simple form in the nonlinear part of the kinematic hardening (see in Eq.(4.6)); in contrast, the OWII model exhibited better adaptiveness to varying ratcheting rates, facilitated by direct adjustments of the control constant, m, (Eq.(4.12) in the model.
For the B320 steel of LC2, the stabilised ratcheting rate observed during the test was still nearly negligible ($< 10^{-4}$%), and the stabilised ratcheting rate remained very low, which was close to a shakedown. Figures 4.15 (c) and (f) indicate that the optimised Chaboche model faced limitations in predicting the ratcheting behaviour of B320 under LC2 with low ratcheting rates, especially in the first few load cycles, as discussed above. The simulation approximated the test ratcheting rate after about 150 cycles, as shown in 4.15 14(f). Meanwhile, the optimised OWII model also had difficulty replicating the ratcheting behaviour of B320, leading to a notably high level of $m = 85$. A possible reason is that the yield stress of the tested sample could be at the upper bound of its variation range, while the mean value was used in the calibration (see Table 4.3). In such a case with the higher yield stress, the test can result in a shakedown state (e.g., for B320 under LC2), and the ratcheting behaviour cannot be correctly captured by the constitutive models calibrated based on the mean yield stress. These observations underscore that more extensive tests of the B320 rail material are needed to better represent its ratcheting behaviour using the Chaboche and OWII constitutive models (to be discussed in further research).

4.6. CONCLUSION AND FURTHER RESEARCH

This study experimentally investigated the mechanical, hardening, and material ratcheting properties of three different rail steels: R220, R260MN, and B320. The testing process was structured into three stages: the monotonic tension tests, cyclic strain range tests, and cyclic stress range tests. The load cases of the cyclic stress range tests were determined based on FE wheel–rail contact simulations to reflect the variation in equivalent stresses on the rail top surface in practice. Test results revealed that the bainitic steel B320 possesses superior mechanical strengths compared to the pearlitic steels R220 and R260MN, exhibiting higher yield stress and ultimate strength. Additionally, B320 showed much less significant ratcheting behaviour in the two applied load cases representing partial-slip and full-slip wheel–rail contact, respectively, in contrast to the pearlitic steels. The R220 and R260MN rails demonstrated similar mechanical strengths, with R260MN being slightly stronger, and similar ratcheting behaviours in both load cases. The test outcomes were then utilised to calibrate and optimise the hardening parameters of the Chaboche and OWII constitutive models. The comparisons between the test and simulation results using the optimised constitutive models indicated that the Chaboche model is reasonably accurate in modelling the shakedown behaviours for the bainitic B320 and

the ratcheting behaviours at high ratcheting rates for the pearlitic R220 and R260MN rail steels , but less adaptive for simulating the ratcheting behaviours at low ratcheting rates for the three rail steels; the OWII model, in contrast, exhibited better performance in terms of rail shakedown and ratcheting behaviour modelling for all three rail types and for both load cases.

All the three tested rail steels have experienced material ratcheting during the cyclic stress range tests, especially in the LC2 that produced the equivalent stress condition of a full-slip wheel-rail contact. However, the material ratcheting of the B320 steel was much less pronounced, as it was in elastic shakedown in LC1, and still close to a shakedown state in LC2. The subdued ratcheting behaviours could be attributed to the relatively low initial plastic strain of the B320 in the first cycle (because of the high yield stress of B320), which remained below 1%, possibly limiting the isotropic softening of the rail steel and the subsequent material ratcheting behaviour. Therefore, for a better understanding and representation of the ratcheting characteristics of the B320 bainitic rail steel, it would be beneficial to conduct the following complementary tests:

- First yield the B320 steel to a plastic strain of e.g., 1% (to be determined based on FE contact simulation) to possibly saturate the isotropic softening, and then use the yielded material in the uniaxial cyclic stress range test under the same stress ranges determined in this study.
- Include torsion loading in a bi-axial cyclic stress range test of B320, using shear stresses to induce a higher effective plastic strain under compressive and shear stress ranges that are equivalent to the stress ranges used in this study.
- Use higher stress ranges to induce higher plastic strains and compare B320 with premium rail steel grades such as MHH (head-hardened pearlitic) or B360 (bainitic), which have comparable or higher mechanical strengths.

Moreover, this study focused mainly on the uniaxial ratcheting behaviour of rail steels. However, the bi-axial stress conditions can produce different ratcheting behaviours in steels. Without addressing the bi-axial stress conditions may thus limit the accuracy of the constitutive models in replicating these behaviours [47], [48]. Therefore, it is recommended to extend the experimental investigation to bi-axial tests to further enhance the understanding of the ratcheting behaviours of the rail steels in practice and also to assess the precision of the Chaboche and OWII models to predict the ratcheting behaviours of the three rail steels under bi-axial conditions.

5

SIMULATION AND VALIDATION OF THE RATCHETING EFFECTS IN B320 AND R260MN RAILS UNDER CYCLIC WHEEL–RAIL CONTACTS

This chapter employed an efficient and accurate FE wheel–rail frictional rolling contact model to simulate the ratcheting effects in rail steels (bainitic B320 and pearlitic R260MN) under 100 cycles of contact loading measured from the HC tests on V-Track test rig. The FE simulation considered both the rail material ratcheting (an intrinsic material property of steel) and structural ratcheting (subjected to altering cyclic contact stress conditions), with the former represented by a calibrated Chaboche constitutive model and the latter captured by the evolving contact patch in the FE simulation. The simulation results were then validated by comparing to the measured running-band width and rail head plastic deformation in the V-Track. A comprehensive analysis of the simulated and measured ratcheting effects confirmed that the bainitic B320 rail exhibited better anti-RCF performances in terms of slower accumulation of plastic deformation, smaller expansion of the contact patch, and subdued ratcheting rates compared to the R260MN rail. The study also revealed that rail structural ratcheting suppresses the material ratcheting around the longitudinal centreline of the contact patch under the cyclic wheel loading, while at the other locations within the contact patch, the structural ratcheting may intensify the material ratcheting at early cycles, and then suppress it when the contact stresses reach the level of those at the centreline. Furthermore, the study confirmed that accumulation in residual stresses outside the contact patch can lead to accumulation in plastic strains beyond the rail running band, as the secondary effect of wheel–rail contact.

5.1. INTRODUCTION

HC is a common type of RCF and significantly challenges modern railways. HC is primarily attributed to rail ratcheting, i.e. the progressive and directional accumulation of plastic deformation induced by repeated wheel-rail contacts [13]. Extensive ratcheting can deplete the ductility of rail steel, and lead to the formation of cracks [9], [14], serious HC damage [7] and even disastrous accidents [1]. Therefore, gaining a deeper understanding of ratcheting phenomena in the rails is crucial for mitigating HC damages and ensuring the durability and reliability of railway infrastructure.

To investigate the ratcheting effects in rails, two ratcheting phenomena should be addressed: material and structural ratcheting [33], [35]. The material ratcheting is considered as an intrinsic elastoplastic behaviour of the (rail) steels, identifiable by material tests loaded under cyclic homogeneous (proportional) stresses [36], [126], [127]. The material ratcheting of rail steels can also be effectively represented by constitutive models that incorporate isotropic and kinematic hardening processes, emulating their elasto-plastic behaviours [36], [37], [41], [43], [89]. Isotropic hardening/softening describes the expansion/contraction of the yield surface, whereas kinematic hardening replicates the Bauschinger effect, where the yield surface shifts under cyclic loading. Among various constitutive models, the Chaboche model [36], [43] has been widely used in cyclic loading simulations [34], [79], [101], [128], [129] with its relatively simple formulation and low computational demand. The application of the Chaboche model in the ratcheting simulation of wheel–rail contacts, especially including also the structural ratcheting, has not been extensively studied, encouraging further detailed examination and validation of the model under real-life railway operating conditions.

With respect to structural ratcheting, it concerns the plastic strain accumulated under non-uniformly distributed and varied stress conditions with an increase in load cycles. This is particularly relevant in the context of wheel-rail contact, as the contact patch presents an uneven stress distribution [71], [73], and the contact contact geometry, i.e., the profiles of the wheel and the rail, changes due to plastic deformation [40], [84] with contact cycles, leading to alterations in contact stresses in each cycle [79], [84]. Therefore, structural ratcheting should be addressed by wheel–rail contact models to capture the rail ratcheting behaviour under real-life cyclic wheel loading conditions. The features of structural ratcheting cannot be fully captured by 2D analytical or FE models [34], [81], [87] that simulate wheel-rail contact as line contact. As to the 3D FE contact models, due to the high computational demand, simplifications have often been made by modelling either one contact body (usually the rail) with prescribed contact stresses [6], [57], [76], [83] or small parts of the wheel and rail [78]. They excluded the influence of structural ratcheting from its evolving contact geometry, or simulated only full-slip wheel–rail contact as normal real-life railway operation is with partial-slip wheel–rail contact.

To account for both material and structural ratcheting, this research employed an efficient and accurate wheel-rail cyclic contact model [84] with the rail material represented by a calibrated Chaboche constitutive model [130] to comprehensively study the ratcheting effects in the rails. Two types of rail steels were studied: a newly developed bainitic B320 rail and a conventional pearlitic R260MN rail, with their material ratcheting properties characterised through cyclic material tests [130]. Meanwhile, the ratcheting in these rail steels was investigated experimentally in the V-Track test rig at TU Delft [51].

Ratcheting simulations were performed for up to 100 wheel-rail contact cycles, with the same partial-slip loading conditions measured on the same rail steels in the V-Track. The effects of material and structural ratcheting were then analysed in detail in terms of plastic deformation, the evolution of the contact patch, the contact and equivalent stress states, and ratcheting strains at locations within and beyond the contact patch. The simulated ratcheting effects in the rails were also validated indirectly by comparing them to the measured changes in the width of the running band and rail profile in the V-Track.

5.2. METHODOLOGY

This section first explained the ratcheting simulation procedure, and then described the Chaboche constitutive models calibrated for the two rail steels, focusing on their mechanical and hardening parameters used in the simulations. The determination of the loading conditions for V-Track tests was also detailed in this section. Finally, the approach for validating the simulations was explained.

5.2.1. FE MODELLING AND SIMULATION PROCEDURE

An FE model for the rolling contact simulation was built in LS-DYNA [131] to replicate the wheel–rail setup of the V-Track test rig [63], [106], as illustrated in Figure 5.1. The V-Track (an overview shown in Figure 5.1(a)) features down-scaled wheels running over the rails in a ring track, with the wheels and rails made from the original material [66]. The V-Track can reproduce real-life wheel–rail contact conditions, and has successfully produced various rail damages, including HC, as reported in [66]. Figures 5.1(b) and (c) illustrate a comparative view of the wheel-rail setups in the V-Track and FE model in LS-DYNA. The wheel features a cylindrical shape with a radius of 65 mm, whereas the rail head has a designed contact radius of 30 mm. In the FE model, the wheel was simplified as a layer of wheel tread, rigidly connected to the rotating shaft, and the rail was reduced to a partial of the rail head section with a length of 28 mm, as shown in Figure 5.1(c).
This study employed the same modelling procedure as detailed in [84], which has been optimised and verified for its accuracy and efficiency in cyclic contact simulations. Improvements were made in the FE model represented in [84]. The rigid beams were replaced by the constrained nodal rigid body (CNRB)[131] to connect the flexible wheel tread and the rigid central shaft, as illustrated in Figure 5.1(c). This modification further reduced the complexity of the model and improved the computational efficiency. Furthermore, as shown in Figure 5.2, the fine mesh region of the rail was extended over the defined contact region (with a mesh size of 0.15 mm) to capture the build-up in residual stresses and strains beyond the contact region (with a mesh size of 0.30 mm)[51]. As in [84], a fine mesh of 0.10 mm was designated along the rail depth to precisely track the shear stress distribution beneath the rail surface.
This study also used the automated simulation procedure described in [84]. The new FE model employed in this study increased the simulation efficiency with one load cycle taking less than 20 min, while 25 min were needed for a one-cycle simulation in [84], using 16 threads of the CPU at its overclocking speed of 3.7 GHz. The procedure can automatically execute the rail ratcheting simulations for a predefined number of wheel

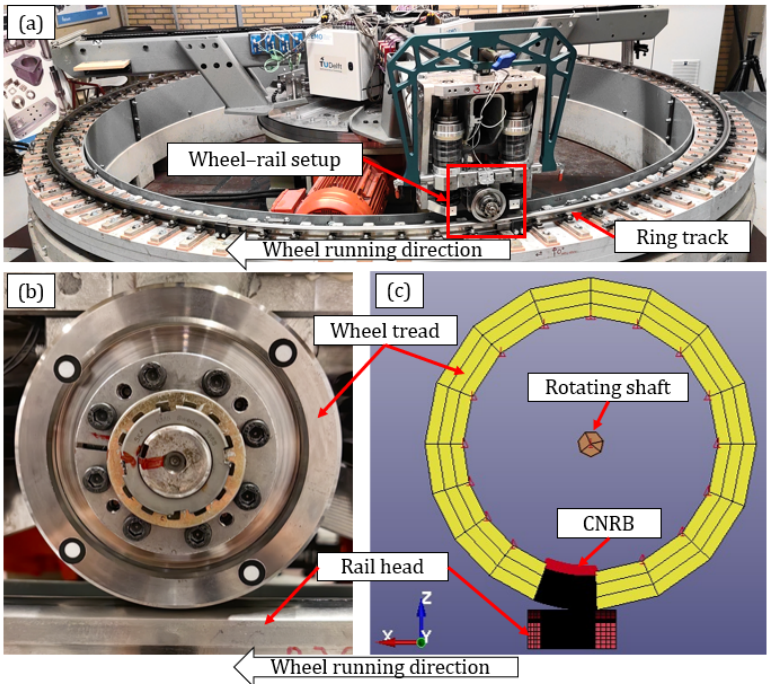

Figure 5.1: The V-Track test rig and the corresponding FE model (a) An overview of the V-Track test rig, (b) scaled wheel and rail in the V-Track, and (c) wheel–rail contact model in LS-DYNA

load cycles, extract the stress–strain states and irrecoverable nodal displacements, and carry them to the next-cycle simulation, thereby capturing the structural ratcheting that features the changes in contact conditions per cycle. The output from the procedure, including the accumulation of plastic deformation, contact patch evolution, and the ratcheting rates, were extensively investigated to examine the complete ratcheting effects in the two rails of concern in this study.

5.2.2. MATERIAL MODEL

Elastic material was used in the wheel to practically approximate the actual situation on V-Track, as in [84]. The wheel on V-Track experienced a high count of revolutions running over the entire ring track in one load cycle of the rail, making contact with $12560 - mm$ length of rail along the ring track, as illustrated in Figure 5.1(a). The high number of contacts of the wheel resulted in a worn profile with a considerably wider running band and strain-hardening of steel in much earlier load cycles than the rail. Therefore, simulating the change in profile of the wheel that is in contact only with a small section of the rail ($28mm$) in this model was unrealistic and unnecessary. Moreover, using the elastic material for the wheel was computationally more efficient for the ratcheting simulation.

To consider the material ratcheting in the rails, the Chaboche NLKH model [36] was

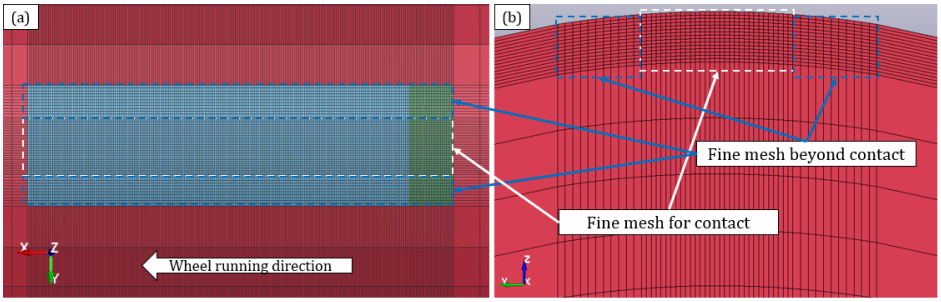

Figure 5.2: Fine mesh zones defined in the rail model (a) fine mesh zones defined on the rail surface (top view of the rail model), and (b) fine mesh zones defined in the rail subsurface (cross-section view of the rail model)

used, integrated with the VOCE isotropic hardening/softening [36], [44], which is available in the LS-DYNA [132]. Table 5.1 presents the mechanical and hardening parameters used in the Chaboche model for the two rail steels, bainitic B320 and pearlitic R260MN. C_i and γ_i $(i = 1,2,3)$ are the plastic modulus and the plastic strain constants to specify each component of the backstresses [36], [38]. The Q and b are the limits of the change in yield stress and the exponent constant that regulates the rate of isotropic softening, respectively. The isotropic softening is indicated by the negative values of Q as shown in Table 5.1 as the yield stress saturates at σ_y,softened $= \sigma_{y,0} + Q$ with accumulated effective plastic strain.

Table 5.1: The mechanical and hardening parameters of R260MN and B320 rail steels [130]

Parameters	R260MN	B320	unit
C_1	461000	522000	
C_2	20000	70000	MPa
C_3	11300	15500	
γ_1	1964	2213	
γ_2	87	240	-
γ_3	0.0001	36	
Q	-167	-220	MPa
b	277	215	-
$\sigma_{y,0}$	348	538	MPa
E	198	196	GPa

The hardening parameters of the rail steels were calibrated with uniaxial material tests discussed in [130], which showed that B320 steel has superior mechanical strengths, evident in its limited accumulation of plastic strain during cyclic loading, compared to the pearlitic R260MN steel. According to [130], the calibrated Chaboche model of the B320 rail was able to replicate the elastic shakedown under a stress range equivalent to the traction condition of 0.3 with a normal contact force of $3500N$, higher than the load cases in this study (discussed in Section 5.2.3). In contrast, R260MN steel produced a much higher material ratcheting strain from the stress range equivalent to the same traction condition, resulting in a very small value of γ_3 (in Table 5.1) to match the sta-

bilised ratcheting rate of the test, but with an overshoot in the ratcheting strain. We can thus anticipate that the B320 rail will show less ratcheting effects than the R260MN rail in the ratcheting simulations

5.2.3. LOAD CASE

The loading conditions for the simulations were determined at two locations of the V-Track: on the B320 rail section between the sleepers 19 and 22, and on the R260MN rail section between the sleepers 87 and 90. The vertical and longitudinal wheel–rail contact forces measured from the V-Track at different load cycles (cycles 1, 50 and 100) are presented in Figure 5.3, together with the coefficient of (CoT), i.e. ratio of the longitudinal force to the vertical force. The lateral force was minimised as controlled below 5% of the longitudinal forces in the HC tests. The contact forces were low-pass filtered at $100Hz$ to remove the high-frequency dynamic effects that were less relevant for quasi-static HC initiation [78], [105]. A low-frequency fluctuation remained in the filtered loads with a wavelength of about $5cm$, as shown in Figure 5.3. Its possible impact will be discussed later in Section 5.3.5.

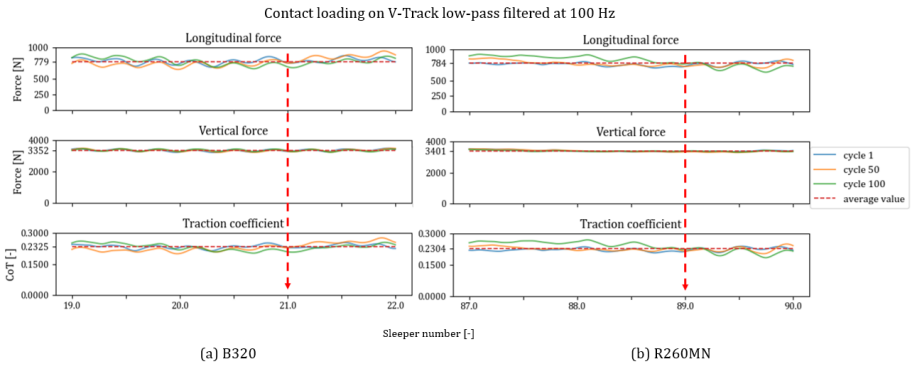

Figure 5.3: : Longitudinal, vertical forces and the coefficient of traction(CoT) measured from V-Track for (a) B320 and (b) R260MN rails

Figure 5.3 shows that the measured wheel-rail contact forces have good repeatability. The average vertical and longitudinal forces over the three sleeper ranges are $3352N$ and $779N$ for B320, and $3401N$ and $784N$ for R260MN, respectively. The traction coefficients on both rails are around 0.23. These load values were used as loading conditions for the quasi-static FE simulations. Because the loading conditions on the sleeper No. 21 for B320 and No. 89 for R260MN were quite close to these average values (i.e. the simulated loading condition), as indicated by the red dashed arrow in Figures 5.3(a) and (b), respectively, the measured ratcheting effects on these two sleepers in the V-Track were used to compare with the simulation results for the validations.

5.2.4. VALIDATION

This study took an indirect approach, i.e. measuring the rail surface running band and cross-sectional profile changes, to validate the results of the ratcheting simulation. The

direct validation, e.g. comparing the ratcheting strains between the simulation and test [15], [87], will be conducted in a follow-up study, because because it would be inefficient and costly if we cut a small rail sample at 100 cycles just for validation while the HC tests with a ring track of rails were planned to run for much higher number of cycles on V-Track. Furthermore, the ratcheting strain as normally indicated by the deformed pearlite lamellae [15] could hardly be observed under an optical microscope after only 100 load cycles compared to that after 60,000 cycles [51].

RAIL SURFACE CHANGE

As a preliminary assessment, the running bands on the rail surfaces were examined with the measured widths compared to the simulated wheel–rail contact patch sizes. As shown in Figure 5.4, rail surface images before applying wheel loading and at sleepers No. 21 (B320 Rail) and No. 89 (R260MN) after 100 load cycles were captured, using an ultra-macro lens with a $25-mm$ focal length and a magnification of $2.5\times$. These images were post-processed to visually identify the running bands on the rail top surfaces after 100 wheel load cycles. The running bands measured on the B320 and R260MN rails after 100 cycles were $1.99mm$ and $2.27mm$ in width, respectively.

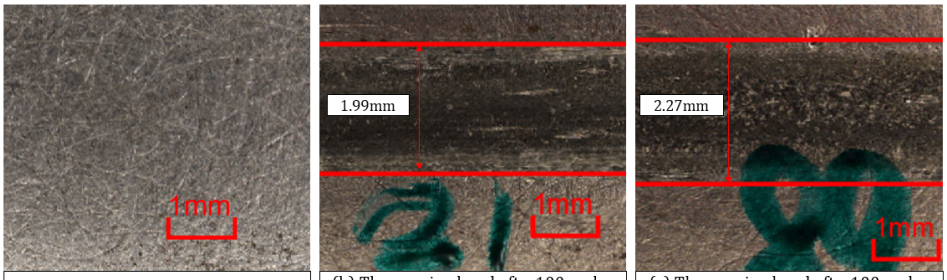

(a) Original surface before test

(b) The running band after100 cycles – B320

(c) The running band after100 cycles – R260MN

Figure 5.4: Rail surface observed from the images: Rail surface observed from the images: (a) rail surface before applying wheel loads, (b) top surface of B320 rail after 100 wheel loads, and (c) top surface of R260MN rail after 100 wheel loads

RAIL CROSS-SECTIONAL PROFILE CHANGE

The cross-sectional profile changes of the rail heads were captured using a HandyScan 3D black Elite. The scanner setup on the V-Track and a result image during scanning are demonstrated in Figures 5.5(a) and (b), respectively. The meshes of the rail surfaces generated by the 3D scan were used to obtain the cross-sectional profiles in the contour graph in the Y-Z plan (normal to the rail longitudinal direction), as shown in Figure 5.5(c). The cross-sectional contour curves were then resampled at every 0.05 mm along the Y-axis (in the lateral direction). The resampled cross-sectional profiles were subsequently filtered to remove noise from the scans, as an example shown in Figure 5.5(d). The undeformed rail head profiles were reconstructed using the least squared method based on the resampled points from the undeformed surface parts (away from the apparent running band) to determine the original contact radius, R, as indicated in

Figure 5.5(d). The maximum difference between the deformed and reconstructed 'original' profiles in the Z-axis (in the vertical direction) was identified as the vertical plastic deformation dZ, as shown in Figure 5.5(d).

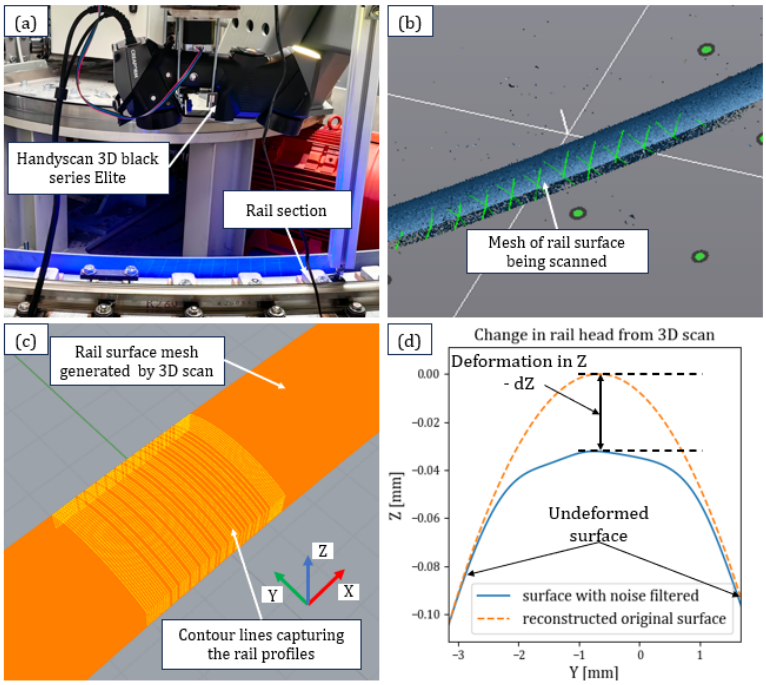

Figure 5.5: Rail cross-sectional profile measured with 3D scans: (a) the scanner setup (b) the scanning process (c) the sampling of the profiles from scanning (d) the post-processed rail profile and the deformation in the Z-axis

5.3. SIMULATION RESULTS AND VALIDATION

This section analysed the simulation results of the ratcheting effects in the two rail steels. The plastic deformations in the rail surface and subsurface, along with the evolution of contact patches, were first analysed and compared between the B320 and R260MN rails. The structural ratcheting represented by the evolving contact and equivalent stresses was then analysed in detail at different locations within and beyond the contact patch. The complete ratcheting effects were further evaluated in terms of the ratcheting strains and rates. Lastly, validation of the simulated ratcheting effects was discussed.

5.3.1. PLASTIC DEFORMATION

Figures 5.6 and 5.7 present the simulated rail head plastic deformation evolution in 100 load cycles for the B320 and R260MN rails, respectively. The same loading conditions were applied, as presented in Section 5.2.3. We can see that both rails show similar patterns in the development of plastic deformation, which was rapid in earlier cycles (from cycle 1 to cycle 20), then moderated (from cycle 20 to cycle 45, and from 45 to 70), and

finally approached stabilisation (after cycle 70). The B320 rail, owing to its superior mechanical strength, produced less plastic deformation than the R260MN rail, as anticipated. The R260MN rail experienced almost twice as much plastic deformation as the B320 in all three axis directions.

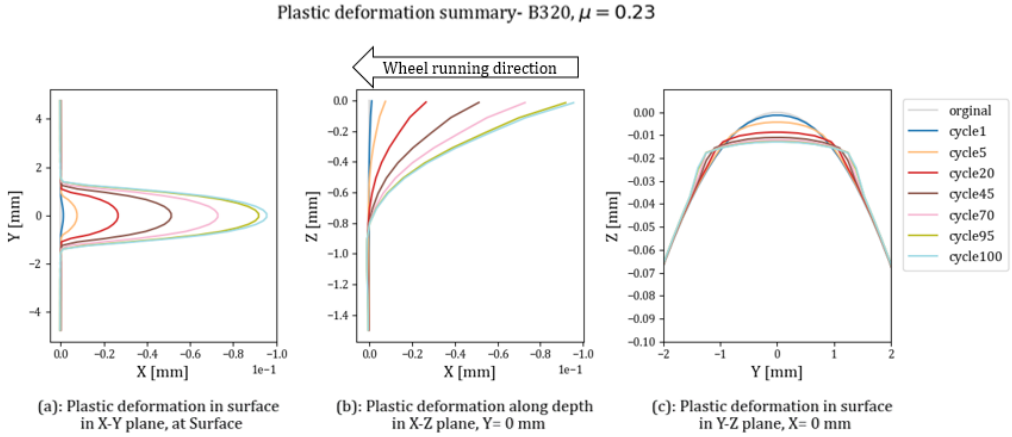

Figure 5.6: Simulated accumulation of plastic deformation of B320 rail, (a) plastic deformation in the X-Y plane (b) plastic deformation in the X-Z plane, and (c) plastic deformation in the Y-Z plane.

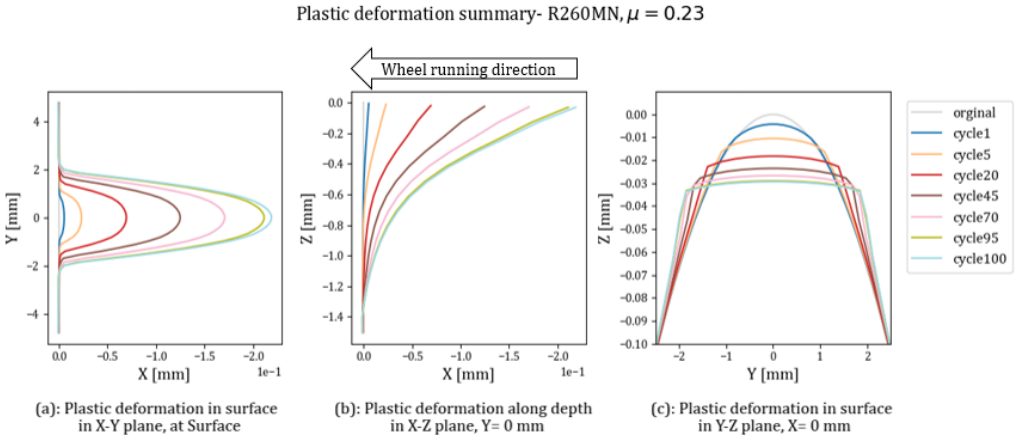

Figure 5.7: Simulated accumulation of plastic deformation of R260MN rail, (a) plastic deformation in the X-Y plane (b) plastic deformation in the X-Z plane, and (c) plastic deformation in the Y-Z plane.

Figures 5.6(c) and 5.7(c) also show that for both rails, the contact radii in the lateral direction increased with load cycles due to the accumulation of plastic deformation. An increase in contact radii can then affect contact conditions and solutions, e.g. expanding the contact patches and, at the same time, reducing the contact stresses at the centreline of the contact patch (to be elaborated in the next section). Furthermore, the differences

in the Z-axis between the original profile and those during the load cycles indicate to what extent the rail head was plastically deformed in the simulation. The validation of this plastic deformation against the test results is presented in Section 5.3.5.

5.3.2. CONTACT PATCH EVOLUTION

Figures 5.8 and 5.9 compare the wheel–rail elasto-plastic contact solutions of the B320 and R260MN rails to those on the purely elastic rail under the same loading conditions. Both plastically deformed rails have their peak normal contact pressures leaning toward the leading side of the contact patch, in contrast to the symmetrical contact pressure distribution of the elastic rail. That is because, for the B320 and R260MN rails, the higher shear stresses on the trailing side of the contact patch plastically deformed the rail more than that on the leading side, causing larger expansion of the contact patch on the trailing side and thus with lower contact pressures, thus forming the egg-shaped contact patch with the peak contact pressure shifting forward [74], [100], [133]. Therefore, the contact patches of B320 and R260MN rails had egged shapes as compared to the elliptical shape on the elastic rail, as marked by the red dashed ovals in Figures 5.8(c) and 5.9(c).

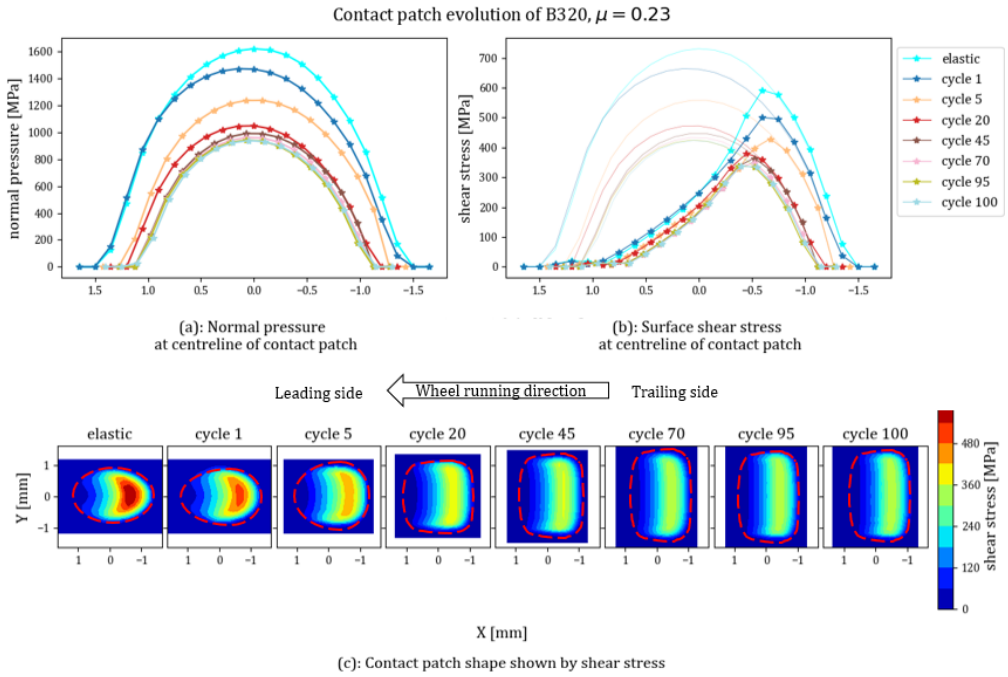

Figure 5.8: Contact stresses and contact patch evolution of the B320 rail

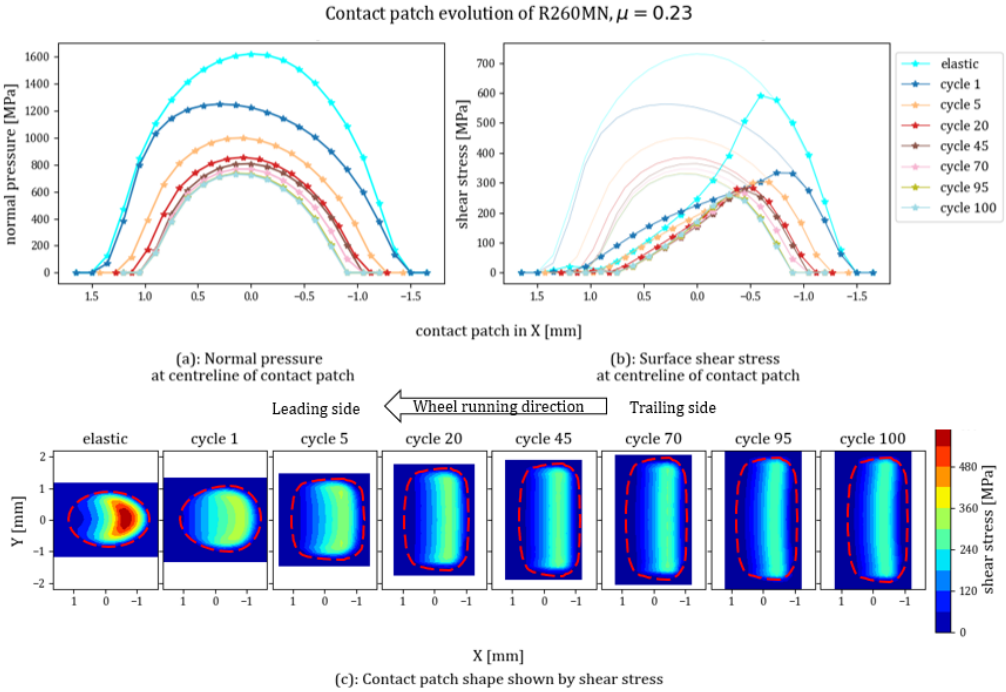

Figure 5.9: Contact stresses and contact patch evolution of the 260MN rail

Furthermore, the B320 rail had contact stresses in the first load cycle close to those of the elastic rail, with their contact patches differing marginally as indicated in Figure 5.8(c). This small difference in contact pressures indicated that the plastic deformation in the B320 rail of the first cycle was relatively small due to its higher yield strength. Contrastingly, the R260MN showed much lower contact stresses in the first cycle compared to those of the elastic rail, and the contact patch of R260MN was significantly larger than those of the elastic and B320 rails. The results showed that the use of elastic material can overestimate the actual contact stresses and is thus less suitable for analysing the ratcheting in rail.

The contact patch evolves with increasing load cycles due to plastic deformation as discussed in [40], [84]. Figures 5.8(c) and 5.9(c) show the simulated contact patch evolution of B320 and R260MN rails, respectively. With the accumulation of plastic deformation, the contact radii of the rail head increased, as shown in Figures 5.6 and 5.7. This process led to a considerable expansion of the contact patch in the lateral direction and limited shrinkage in the longitudinal direction in 100 wheel load cycles, as shown in Figures 5.8(c) and 5.9(c). The contact patch expansion was more significant in the early cycles, especially within 20 cycles, and approached stabilisation after 70 cycles. For both rails, the contact patches barely changed between the 95th and 100th cycles. This trend aligned well with the development in the accumulation of plastic deformation presented in Figures 5.6 and 5.7.

The change in surface contact stresses on the two rails, as shown in Figures 5.8 and 5.9,

followed a similar pattern: the magnitudes of the contact stresses first decreased rapidly, and gradually stabilised after 70 cycles. The stabilised normal and shear stresses were considerably lower than those of the first cycle. Additionally, the contact stresses decreased much less significantly in the B320 rail than in the R260MN due to the smaller plastic deformation accumulated over 100 cycles and consequently the smaller expansion in the contact patch.

For the first wheel load cycle, the contact stresses yielded the rail material, initiating material plastic deformation in the rail head. The contact stresses were effectively reduced by the plastic deformation, decelerating material ratcheting at the centreline of the contact patch. Subsequently, the rail head continued to accumulate plastic deformation, leading to further expansion of the contact patch and reduction in contact stresses. Therefore, at the centreline of the contact patch, the material ratcheting gave the structural ratcheting a pattern of decreasing stresses over the cycles; Meanwhile, the structural ratcheting suppressed the material ratcheting by decreasing contact stresses over the load cycles. Eventually, an equilibrium in the change of contact stresses was reached between the material and structural ratcheting so that the decrease in contact stresses and accumulation of plastic deformation stabilised as indicated by the small but steady change in contact stresses between cycles 95 and 100 for both rails shown in Figures 5.8 (a), (b), 5.9 (a) and (b).

5.3.3. CONTACT INDUCED STESSES

To obtain an overview of ratcheting effects in the B320 and R260MN rail heads, we examined both the rail surface contact stresses and the effective stresses of the surface elements at five different lateral (Y) locations: four within and one beyond the contact patch after 100 wheel load cycles, as shown in Figures 5.10 and 5.11, respectively. The black dashed lines in the figures demarcate the stress conditions into three parts: before, during and after contact.

Figures 5.10 and 5.11 show the changes in the surface contact stresses and equivalent stresses of the surface elements at various lateral locations for both rails over the load cycles. The surface shear stresses at the longitudinal centreline of the contact patch, i.e. $Y = 0.0mm$ in Figures 5.10 and 5.11, are the same as those presented in Figures 5.8(b) and 5.9(b) where the comparisons to the elastic solutions are also given. The effective stresses at $Y = 0.0mm$ exceeded the initial yield stresses ($538MPa$ for B320 and $348MPa$ for R260MN, as denoted by the blue horizontal lines) in all load cycles, and their variations followed a similar pattern as the contact stresses: they first decreased rapidly and then gradually stabilised. We can see that the peaks of the equivalent stresses align with those of the contact shear stresses. This confirmed that the contact shear stress contributed the most to material yield [42] within the contact patch [66].

In cycle 1, at the edge of the contact patches, which was $Y = 0.87mm$ for B320 and $Y = 1.02mm$ for R260MN (not yet any surface stresses at further locations), the effective stresses were below the initial yield stresses, indicating that plastic deformation did not occur throughout the contact. At the furthest locations of interest away from the contact patch centreline, no surface contact stresses were present since they were beyond the contact patch, while the contact-induced effective stresses existed with low magnitudes. The after-contact parts of Figures 5.10(b) and 5.11(b) also show that the effective stresses

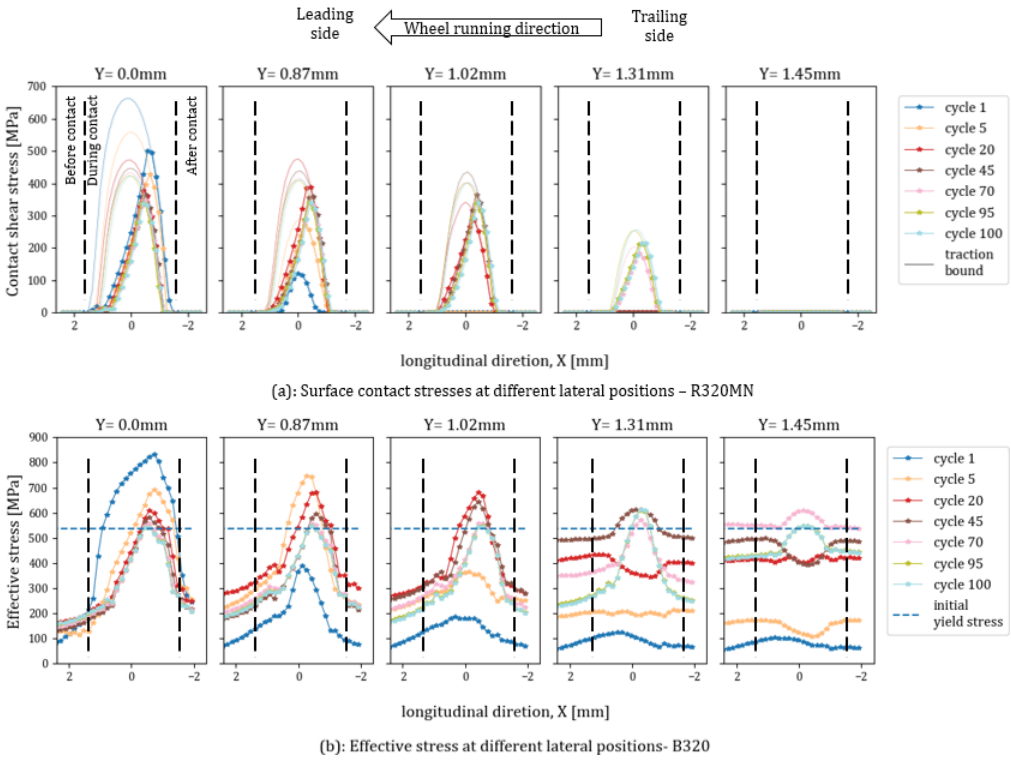

Figure 5.10: Stress states in the B320 rail in various load cycles at various lateral locations: (a) contact surface shear stresses and traction bound, and (b) the effective stress of the surface elements.

did not diminish after wheel passing, indicating that residual stresses were generated in rails after contact.

In cycle 5, both the contact and effective stresses increased significantly at the contact patch edge locations of cycle 1 ($Y = 0.87mm$ for B320 and $Y = 1.02mm$ for R260MN), indicating that the contact patches expanded and yielded the rails further in the lateral direction. The contact-induced effective stresses beyond the contact patch, i.e. over $Y = 0.87mm$ for B320 and $Y = 1.02mm$ for R260MN (with zero surface contact stress), can also be observed. In particular, the effective stress exceeded the initial yield stress on the R260MN rail at $Y = 1.31mm$, exhibiting the secondary effect of contact discussed in [66]: the compressive wheel-rail contact patch incited tension around it and the accumulation of these residual tensile stresses could also cause the rail to yield.

With a further increase in cycles, we can see that the edge of the contact patch expanded further for both rails, indicated by non-zero surface stresses at further lateral locations. This, meanwhile, caused the surface and effective stresses to decrease at the longitudinal centrelines of the contact patches. Different structural ratcheting patterns can be observed at the other lateral locations than the centreline: the contact stresses first increased until they approached the level at the centreline, then decreased, and eventually stabilised. For instance, by comparing the left two graphs of Figure 5.10(a), the surface

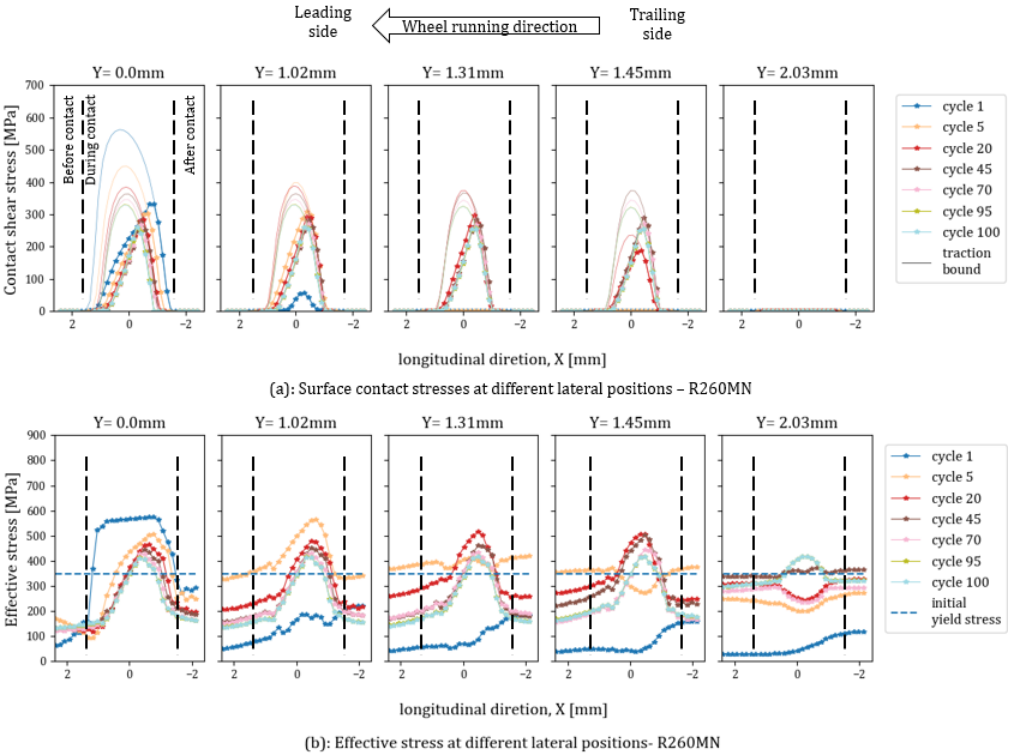

Figure 5.11: Stress states in the R260MN rail in various load cycles at various lateral locations: (a) contact surface shear stresses and traction bound, and (b) the effective stress of the surface elements.

stresses at $Y = 0.87mm$ for B320 increased with load cycles and reached the same level at the centreline in cycle 20; and then the surface stresses decreased until cycle 70 and stabilised afterwards.
In cycle 100, the half-width of the contact patch expanded beyond $1.31mm$ for B320 and $1.45mm$ for R260MN, indicated by the non-zero surface stresses. Within the contact patch, the effective stresses within 100 cycles all exceeded the softened yield stress (σ_y,softened $= \sigma_{y,0} + Q$). Beyond the contact patch, we can see that the effective stresses may also exceed the yield stresses at $1.45mm$ for B320 and $2.03mm$ for R260MN, implying that the plastic deformation could occur from the secondary effects of rolling contact, even though the ratcheting effects within the contact patch appeared to stabilise.

5.3.4. RATCHETING RATE

The ratcheting behaviours of the rails can be quantified in terms of the ratcheting strains and rates, represented by the effective plastic strain accumulated throughout the cycles p^{eff} and the change of the effective plastic strain per cycle dp^{eff}/dN, respectively [38], [39], [76]. With only the material ratcheting considered, we may expect that the ratcheting rate decreased rapidly and stabilised after a few cycles as exhibited in material ratch-

eting tests [38], [39]. This stabilised ratcheting rate has been used to calculate the critical ratcheting strain and to predict the initiation of RCF cracks [34], [76]. The ratcheting simulations of this study revealed some different patterns in the ratcheting strains during wheel–rail rolling contacts when the structural ratcheting was considered.
Figure 5.12 shows the ratcheting of the B320 rail at different lateral locations within and beyond the contact patch. At the centreline $Y = 0.0mm$, the ratcheting rate shown in Figure 5.12(b) started at a relatively high value, and then quickly decreased with load cycles, and finally stabilised at 0.0013 after 40 cycles, which is also evident with the linear increase of ratcheting strain shown in Figure 5.12(a). This change in ratcheting rate was consistent with the trends in the accumulation of plastic deformation as discussed in Section 5.3.1 and similar to the material ratcheting behaviour. However, as discussed in Sections 5.3.2 and 5.3.3, the change in the ratcheting rate was influenced by not only the material ratcheting of the rail steel but also the structural ratcheting during which the contact stresses decreased with the expansion of the contact patch and thus the material ratcheting was decelerated.

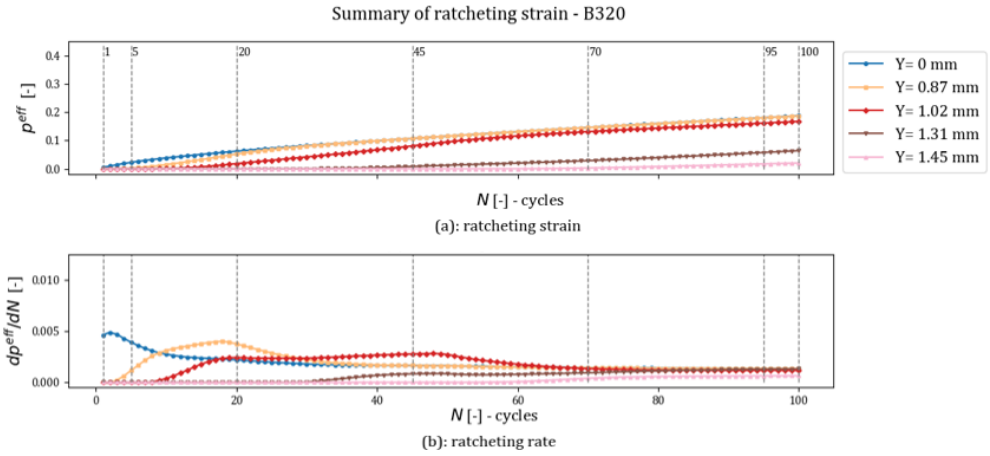

Figure 5.12: Ratcheting strain and rate in the B320 rail over the 100 load cycles at five different lateral locations (a) the accumulation of ratcheting strain, and (b) the change of ratcheting rate

The ratcheting rates in B320 rail at the other lateral locations of the contact patch showed different patterns. For instance, at $Y = 0.87mm$ (likewise at $Y = 1.02mm$), the ratcheting rate increased with load cycles (in line with the contact stresses increase per Figure 5.10) and peaked at cycle 18, and then decreased afterwards, and eventually stabilised at cycle 70 to a similar level of that at the centreline. The change in the ratcheting rate aligned with the trend of the contact surface and effective stresses presented in Section 5.3.3. At $Y = 1.31mm$, the ratcheting rate generally increased until it stabilised after 80 cycles. The rail ratcheting behaviours at these locations, i.e. $Y = 0.87mm$, $Y = 1.02mm$ and $Y = 1.31mm$, were thus influenced by the structural ratcheting discussed in Section 5.3.3. Furthermore, at $Y = 1.45mm$, which was still outside the contact patch at cycle 100, we can observe the onset of plastic deformation in the 53rd cycle. This confirmed that plastic strains can accumulate beyond the contact patch, attributed to the

secondary effect of contact discussed in [66].
Similar trends can be observed in Figure 5.13 for R260MN rail ratcheting strains and rates. The R260MN rail accumulated higher effective plastic strains, almost twice as much as that of the B320. The stabilised ratcheting rate of R260MN is around 0.0026, while that of B320 is 0.0013 The higher ratcheting rate was expected since the R260MN rail has lower mechanical strengths than the B320 rail with more plastic strain accumulated already at early cycles (c.a. 0.10 for R260MN versus c.a. 0.05 for B320 in 20th cycle) , which led to saturation of isotropic softening and softened yield stress at early cycles, further intensifying material ratcheting.

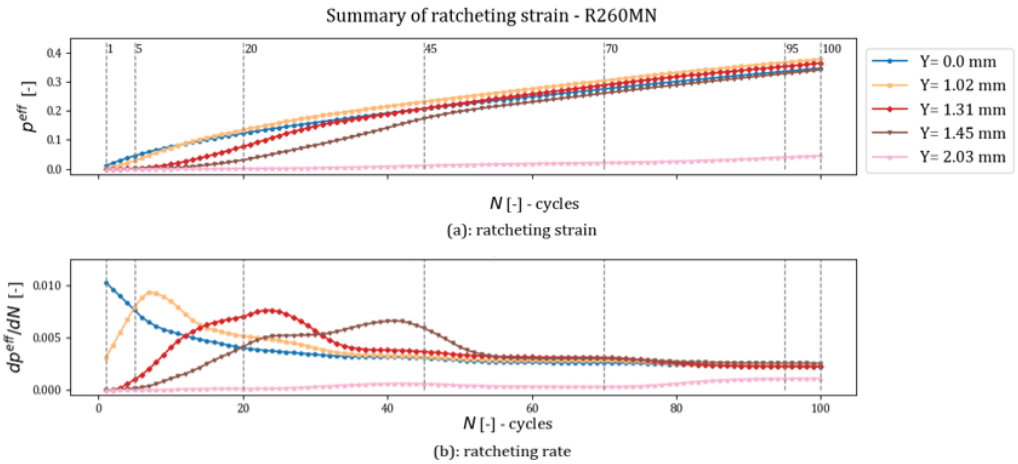

Figure 5.13: Ratcheting strain and rate in the R260MN rail over the 100 load cycles at five different lateral locations (a) the accumulation of ratcheting strain, and (b) the change of ratcheting rate

The patterns in the ratcheting rates within the contact patch of both rails underscore the crucial influence of the structural ratcheting at wheel–rail contact. At/around the centreline of the contact patch, the structural ratcheting had a suppressive effect on the rail ratcheting as the ratcheting rate decreased (see in Figures 5.12(b) and 5.13(b)), owing to the expansion of the contact patch and reduction in contact stresses (see in Figures 5.10 and 5.11, $Y = 0.0\,mm$). At the locations within the contact patch away from the centreline, the structural ratcheting at early load cycles reinforced the material ratcheting and consequently led to increasing ratcheting rates, as the contact stresses increased with the expansion of the contact patch, causing the rail to yield further. When the contact stresses at these lateral locations reached the level of those at the centreline with the increase of load cycles, the structural ratcheting began to suppress the material ratcheting, which then slowed down the accumulation in plastic deformation and subsequently contact patch evolution. The suppressing effect of structural ratcheting diminished when the equilibrium (as in the change of contact stresses) was reached between the effects of material ratcheting and structural ratcheting, as indicated by the stabilised ratcheting rates approaching the 100th cycle.

5.3.5. VALIDATION

This study took two steps to validate the simulation results. First, the rail running bands observed after the 100th wheel load cycle from the V-Track were compared with the simulated contact patches for both rails. The width of the contact patch was checked against the that of the running band for an initial assessment. Second, the rail top plastic deformation after the 100th cycle in the Z-axis was extracted from 3D scans of the geometry on the V-Track, statistically analysed and compared with the simulated vertical plastic deformation for the B320 rail.

RUNNING BAND

Figure 5.14 shows the simulated contact patches at the 1st and 100th cycles compared with the running bands on the V-Track after 100 cycles for both rails. The white grids indicate the FE mesh size on the rail top surface, which is $0.15mm \times 0.15mm$. The contact patches on both rails of the first cycle can fit well within the observed running bands in Figures 5.14(a) and (c), demonstrating the reliability of using the FE method and V-Track test rig to study wheel–rail contact.

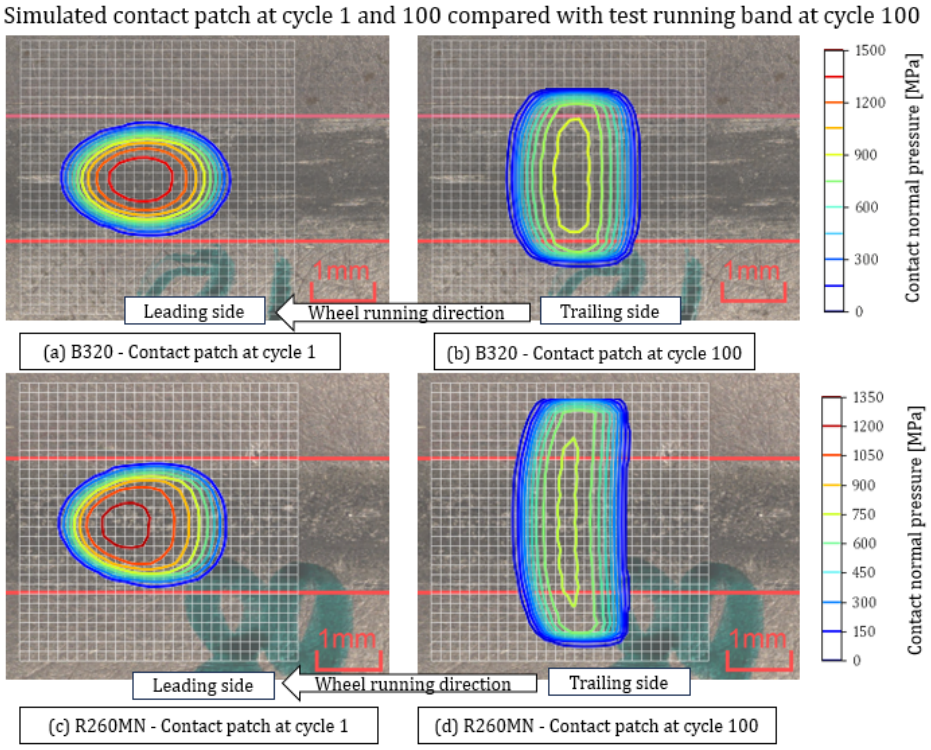

Figure 5.14: Simulated contact patch compared with the observed running bands, (a) contact patch of cycle 1 for B320, (b) contact patch of cycle 100 for B320, (c) contact patch of cycle 1 for R260MN, and (d) contact patch of cycle 100 for R260MN

Figures 5.14(b) and (d) compare the simulated contact patches with the observed run-

ning band after the 100th cycle. The simulated contact patch on the B320 rail slightly exceeded (with three elements on each side) the running band, whereas that on the R260MN rail was much wider (approximately 6 elements on each side) than the observed running band. The B320 rail had relatively limited expansion in the contact patch, as also indicated in Figure 5.8(c), owing to its high yield stress and subdued material ratcheting behaviour [130]. The overestimation of the contact patch expansion for R260MN could be attributed to the excessive plastic strains induced by the material ratcheting represented by the Chaboche model. As discussed in Section 5.2.2, the hardening properties of the Chaboche model for R260MN could result in an overshoot in replicating the ratcheting strains, causing plastic deformation and consequently the size of the contact patch to be overestimated, especially within 20 cycles (as shown in Figure 5.9), in the rail ratcheting simulation. Therefore, the simulation results of the R260MN rail plastic deformation were not further compared with the test in the second step of validation.

PLASTIC DEFORMATION IN Z-AXIS

30 rail cross-sectional profiles were selected from the scanned rail surface in a 5-cm range over the sleeper NO. 21 of the B320 rail based on random selection and then analysed. The reconstructed contact radii of original rail profiles (R) and the vertical plastic deformation(dZ) after 100 load cycles were post-processed from the selected profiles. The reconstructed radii of the original rail profiles ranged from 29.40mm to 30.40mm, with a median of 29.76mm and a mean of 29.80mm while the (design) radius used in the FE rail model was 30mm. The vertical plastic deformation, determined by comparing the deformed and the reconstructed original rail profiles, as demonstrated in Figure 5.5(d), varied from 0.005mm to 0.030mm with the average at 0.017mm and median at 0.015mm.

Since the contact radii R of the 30 selected rail profiles were distributed over a relatively large range of 1mm with a median value (29.76) smaller than design radius, a further selection was made considering the R in a 3% range over design radius of 30mm for a better comparison with the simulated results. The corresponding vertical plastic deformation dZ ranged from 0.0075mm to 0.0275mm with a median of 0.014mm and a mean of 0.016 mm, as the statistics shown in Figure 5.15(a). The difference in the plastic deformation among the cross-sections can be caused by the fluctuation of wheel-rail contact forces shown in Figure 5.3, which possibly resulted in the variation in the plastic deformation and wear along the rail in the V-Track. As indicated by a red horizontal line in Figure 5.15(a), the simulation result of dZ is 0.013mm, which was determined based on the simulated surface plastic deformation in Figure 5.6(c). Figure 5.15(b) compares the simulated deformed rail profile to one measured profiles with a R of 30.10mm, both attaining a dZ of 0.013mm. More measured deformed profiles can been seen in appendix. The good agreement between the simulated and measured rail plastic deformation under 100 wheel load cycles confirmed that the effectiveness of the proposed modelling framework to investigate rail ratcheting effects and to predict the initiation of HC cracks.

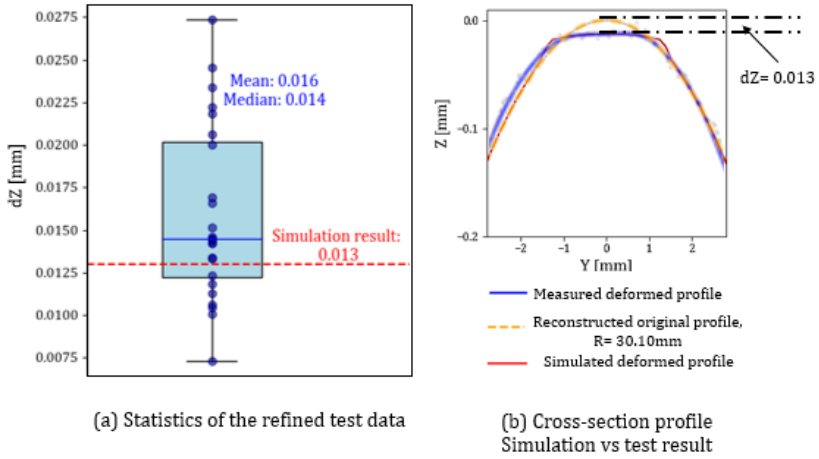

(a) Statistics of the refined test data

(b) Cross-section profile
Simulation vs test result

Figure 5.15: Step-2 validation results of the vertical plastic deformation: (a) statistics of the refined test data vs the simulated result, and (b) a deformed B320 rail cross-sectional profile vs simulated rail profile

5.4. CONCLUSIONS AND FURTHER RESEARCH

This study addressed both the material and structural ratcheting to elucidate the ratcheting effects observed in rails subject to cyclic wheel–rail rolling contacts. Employing the Chaboche material models to represent two rail steels, i.e. B320 and R260MN, in an efficient and accurate FE frictional rolling contact model, both the ratcheting processes were incorporated in the cyclic wheel–rail contact simulations. The wheel–rail frictional rolling contacts were simulated up to 100 cycles using the same loading conditions as measured from a V-Track test that was designed to generate real-life rail ratcheting and head checks. Furthermore, the running-band width and rail head plastic deformation from the V-Track were measured to validate the simulated wheel–rail contact solutions and rail ratcheting behaviours. The good agreement between the simulations and measurements supports the effectiveness of the proposed modelling framework to investigate rail ratcheting effects for predicting the initiation of HC cracks. The primary findings are summarised as follows.

- The wheel-rail contact stresses are reduced under cyclic wheel loading when the plasticity in the rail steels occurs, since the plastic deformation increases the size of the contact patch, with other things equal. This cannot be considered by linear elastic material models.
- The distribution of contact shear stress for a 3D wheel–rail contact leads to uneven deformation at the contact interface with higher plastic deformation at the trailing end of the contact patch. This pattern in plastic deformation results in an egged shape of the contact patch with the maximum normal contact pressure shifted to the leading end, compared to the symmetrical and elliptical contact patch solved using elastic material..
- The ratcheting simulation over the 100 load cycles confirmed that the B320 rail

outperformed the R260MN rail steel in terms of RCF resistance as it exhibited lower level of plastic deformation accumulation, smaller contact patch expansion, and subdued ratcheting effects.

- The simulation results revealed the interplay between the structural and material ratcheting vary with the location within the contact patch: at the longitudinal centreline, the structural ratcheting suppresses the material ratcheting with decreasing contact stresses over the load cycles; and at the other lateral locations away from the centreline in the contact patch, the structural ratcheting may intensify the material ratcheting at early cycles and subsequently suppress it once the contact stresses reach the level of those at the centreline.

- The ratcheting effect in the rail stabilises when the equilibrium in the change of contact stresses influence by the material and structural ratcheting is reached, showing different patterns as compared to the cases simulated only with the material ratcheting.

- The ratcheting simulations also revealed that the residual stresses can be accumulated outside the contact patch, thereby demonstrating the secondary effect from the wheel–rail contact, i.e. rail steel yield outside the running band.

In this study, the Chaboche constitutive model was used to replicate the material ratcheting, potentially leading to an overestimation of plastic strains and material ratcheting, especially for the soft rail steels with large ratcheting rate, as discussed in [38] and also observed in the simulation results of this study: the simulated contact patch of the R260MN rail was considerably wider than the actual running band observed on the V-Track. Therefore, it is essential for future studies to incorporate more advanced constitutive models, such as OWII or Abdel-Karim-Ohno models [41], [89], in the FE simulations for the ratcheting effects of R260MN rail [57], [80]. Furthermore, to conclusively validate the accuracy of the proposed modelling framework in predicting ratcheting effects, the next phase of research should implement a direct validation method, e.g. deriving the ratcheting strains of the tested rail samples cut from the V-Track based on microscopic examinations [66].

5.5. APPENDIX

A selection of 16 post-processed rail profiles used for validation is presented in Figure 5.16

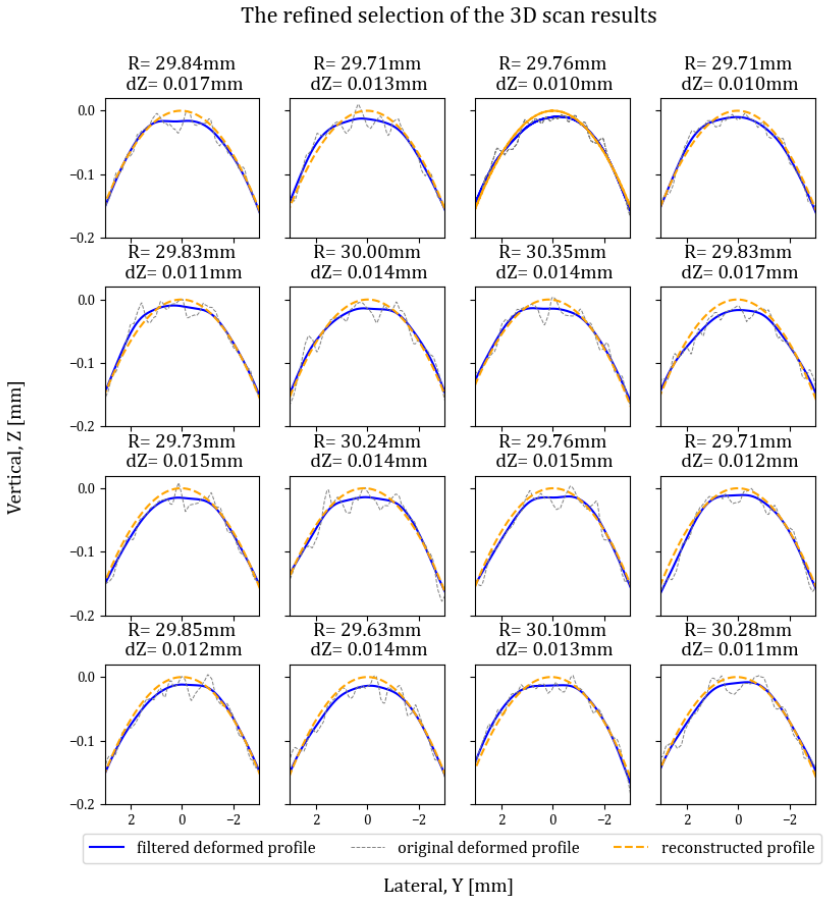

Figure 5.16: 16 cross-section profiles post-processed from the 3D-scanned rail top surface of B320

6

CONCLUSION AND RECOMMENDATIONS

6.1. CONCLUSIONS

This dissertation presented a combined numerical and experimental approach to studying ratcheting effects in rails that are closely associated with the initiation of HC cracks. A numerical simulation procedure using the FE method as developed to accurately and efficiently simulate wheel-rail contact with a large number of cycles. Along with the numerical simulations, lab tests were conducted, including the HCs replication in the V-Track test rig and the microscopic analysis of the HC samples, to investigate the initiation mechanisms of HC cracks and their dependence on the wheel–rail contact conditions (e.g. geometry and loads) and the contact-induced stresses on and beneath the rail surfaces. The material properties of rail steels, as another dominant factor of ratcheting, were tested in terms of elasto-plastic behaviours, and the calibrated classic constitute models were adopted to the FE simulations. The simulated rail ratcheting effects with incorporation of both material ratcheting and structural ratcheting were finally validated against the lab tests. The research (sub-)questions presented in Section 1.6 have been addressed in this dissertation as follows:

Q1 **How can the actual stress conditions and the ratcheting behaviour in the rails be accurately and efficiently captured in an FE simulation with a large number of wheel-rail contact cycles**

This question has been answered in Chapter 2 by developing an innovative FE simulation procedure that can efficiently and accurately simulate the ratcheting effects in the rail. The FE wheel–rail contact model, with its meshing scheme optimised, was verified using the CONTACT programme. By applying a NLKH steel material to the FE contact model, rail ratcheting behaviours under up to 100 partial-slip wheel passages were simulated under different traction conditions. The ratcheting effects were analysed in terms of rail head plastic deformation, wheel-rail contact patch evolution, and ratcheting strains. The findings obtained from the simulations are summarised below:

- The cyclic wheel-rail contacts can cause the rail surface material to deform plastically, consequently increase the contact patch size, reduce contact stresses, and then slow down the further deformation of the rail. The accumulation of plastic deformation, evolution of the contact patch, and increase of the ratcheting strain are rapid at the early load cycles, and then become slower with the increase of cycles and eventually stabilise.
- The interplay between the rail material ratcheting and contact patch evolution (structural ratcheting) should be considered for accurate predictions of rail ratcheting and subsequent HC crack initiations.
- Higher traction coefficients (0.35) significantly increase ratcheting strain and the stabilised ratcheting rate in the rail surface and subsurface compared to the cases with lower traction coefficients (0.10 or 0.20). Shakedown, instead of further ratcheting, can be expected when the traction coefficient is low (e.g. 0.10).

Q2 **How can the ratcheting behaviour and subsequent HC crack initiation be influenced by wheel-rail contact conditions?**

Chapter 3 answered this research question. In this chapter, the initiation mechanism of HC was experimentally investigated using the V-Track to generate ratcheting and HC damage in rails under contacts equivalent to real-life cyclic wheel–rail applications. Samples of the HC damage were then cut from the R260MN rail tested on V-Track for microscopic analyses. Findings from the microscopic analysis were further compared to results of the numerical studies using BEM and FE method. The study led to the following conclusions:

- Capable of maintaining consistent loading for numerous cycles with good repeatability, the V-Track test rig developed at TU Delft can successfully generate RCF-induced rail surface damage under controlled conditions reflecting the real-life wheel-rail contacts under railway operating conditions
- The contact shear stress directions calculated with CONTACT correspond well to the rail ratcheting plastic flows observed from the microscopic analysis, suggesting that the contact analysis using BEM is a valid approach to qualitatively predicting the ratcheting patterns within the contact patch.
- The FE analyses confirmed the key role of contact shear stress in ratcheting formation inside the contact patch. In addition, the FE analyses indicate that wheel–rail rolling contact can also yield rail material and initiate cracks outside contact patch due to residual stress accumulation. The shear stress directions outside the contact patch are opposite to those inside. These FE results are in good agreement with the microscopic analysis results showing an opposite plastic flow pattern outside the contact patch.

Q3 **How can the elasto-plastic behaviours of rail steels under real-life operational conditions be experimentally investigated and characterised with classic constitutive models for ratcheting simulations?**

This question has been addressed in Chapter 4. The chapter experimentally investigates three rail steels (R220, R260MN and B320) for their mechanical properties, elasto-plastic and material ratcheting behaviours. The experimental investigations involve uni-axial tests of monotonic tension, cyclic strain ranges, and cyclic stress ranges. The stress ranges that may generate rail ratcheting behaviour were determined from two wheel-rail load cases of real-life operational conditions. The test results were then used to calibrate the Chaboche and OWII constitutive models to reproduce the elasto-plastic behaviours of the tested rail steels. The calibrated constitutive models were further optimised to represent rail ratcheting behaviour under real-life wheel loads. The findings are summarised as follows:

- Pearlitic steels R220 and R260MN showed similar mechanical strength and ratcheting behaviour. By contrast, the bainitic B320 rail steel exhibit superior mechanical strength and can significantly lower the rail ratcheting responses for the two load cases of interest.

- The OWII model demonstrated greater precision in the rail shakedown and ratcheting behaviour (ratcheting strains and rates) modelling for all the three rail types, whereas the Chaboche model faced limitations, particularly in reproducing relatively low ratcheting rates (for the bainitic B320 rail steel).

Q4 **How can the material and HC experiments be used to calibrate and validate the rail ratcheting prediction models**

Chapter 5 has addressed this question. In Chapter 5, both the material ratcheting of the rail steels and the structural ratcheting occurring at wheel-rail contacts were considered in the rail ratcheting simulations running up to 100 load cycles. Chapter 5 employed the FE modelling principle and simulation procedure presented in Chapter 2 to capture structural ratcheting, and employed the Chaboche models calibrated from Chapter 4 to reproduce the material ratcheting of the B320 and R260MN steels. The ratcheting effects, in terms of plastic deformation, contact patch evolution and ratcheting rates, were analysed for locations within and outside the contact patch, and further validated against the results from HC tests in the V-Track. The findings are summarised below:

- The good agreement between the FE simulations and V-Track measurements supports the effectiveness of the proposed modelling framework to investigate rail ratcheting effects, which can be further utilised to predict the initiation of HC cracks.
- When rail plastic deformation occurs due to wheel–rail contact, the contact shear stress causes uneven deformation in the contact patch, leading to the larger plastic deformation at the trailing end, which results in an egged-shaped contact patch and that the maximum normal contact pressure shifts to the leading end in the simulation.
- Simulation results revealed that the interaction between structural and material ratcheting varies depending on the location within the contact patch. At the centreline, structural ratcheting suppresses material ratcheting by decreasing contact stresses over load cycles, influenced by the accumulation of plastic deformation; and at lateral positions away from the centreline, structural ratcheting may initially intensify material ratcheting due to increasing contact stresses, then suppress it once the contact stresses align with those at the centreline. Ratcheting in the rail stabilises when an equilibrium in the contact stresses change (influenced by both material and structural ratcheting) is reached.
- Ratcheting simulations confirmed the test finding from Chapter 4 that the bainitic B320 rail outperformed the pealitic R260MN rail steel in terms of RCF resistance: the B320 rail exhibited lower levels of accumulated plastic deformation, smaller contact patch sizes, and much subdued ratcheting effects in 100 wheel load cycles
- Ratcheting simulations also confirmed the finding reported in Chapter 3 that the accumulation of residual stresses outside the contact patch can cause rail steel to yield, as a secondary effect from wheel–rail contact.

Through addressing the sub-questions, this dissertation qualitatively investigated the correlation among stress conditions during wheel–rail contact, rail ratcheting, and RCF crack initiation using V-Track, identified a new crack initiation mechanism, and quantitatively developed a validated simulation procedure for modelling ratcheting in rails, thereby advancing the current state-of-the-art. By validating these simulations against V-Track test results, this work made progress in improving predictions of crack initiation through efficient and accurate modelling of wheel–rail contacts, using mechanical and ratcheting properties of rail steels obtained from material testing. The combined approach integrating cyclic rolling contacts with both structural and material ratcheting processes, demonstrated the potential for more precise RCF prediction in complex, real-life railway operations, ultimately enhancing the cost-effectiveness and efficiency of railway operation and maintenance. Additionally, the material testing in Chapter 4 introduced a new selection criterion of rail steels for the industry, e.g. infrastructure managers, providing a quantitative evaluation of their ratcheting properties.

6.2. RECOMMENDATIONS FOR FUTURE RESEARCH

This dissertation has developed and validated an effective framework to study ratcheting, which should be further developed to predict HC crack initiation in rails. Efforts can be taken to further improve the efficiency and accuracy of the modelling and simulation, extensively validate the results, and ultimately implement this framework in field studies under more complex railway operating conditions. The following future research is recommended:

- **Microscopic analysis**.Only the results of the R260MN rail samples were presented in Chapter 3. Results of other steel grades should still be processed and analysed in depth for their ratcheting patterns during wheel-rail contacts. Particularly, the B320 as a new bainitic rail steel that has a microstructure distinctively different from the pearlitic rails should be investigated on a micro scale to understand its effects on ratcheting.
- **Material testing**. The ratcheting behaviour of the B320 steel was not fully activated during the uniaxial stress range tests, which could be related to the low plastic strain in the first load cycle that limits its isotropic softening. Therefore, further testing should be conducted by either loading the test samples with higher plastic strain in the first cycle or incorporating shear strain in a bi-axial cyclic testing.
- **Constitutive modelling**. Chapter 4 calibrated two classic constitutive models, i.e. Chaboche and OWII, for the rail steels in the material testing. The Chaboche model has its limitations in replicating the small ratcheting strains while both the Chaboche and OWII models were not tested in multi-axial conditions. As discussed in Section 1.3.3, more advanced constitutive models have been developed to solve these problems. These models should be tested for their accuracy and most importantly computation efficiency for FE wheel-rail rolling contact simulations with high number of load cycles.
- **Further validation of simulated ratcheting in rails**. The indirect validation approach was used in Chapter 5 by comparing the simulated plastic deformation and

the measured rail profile change over 100 cycles of wheel–rail rolling contact. This proved the validity of this simulation framework in studying ratcheting. Nonetheless, to reach the ultimate goal, i.e. using this framework to predict HC crack initiation, the simulated ratcheting results need to be more vigorously validated directly, e.g. using the ratcheting strains from microscopic analysis over a higher number of load cycles (e.g. 5000 or more). This will be conducted in the future research.

BIBLIOGRAPHY

[1] S. L. Grassie, "Rolling contact fatigue on the british railway system: Treatment", *Wear*, vol. 258, no. 7-8, pp. 1310–1318, Mar. 2005. DOI: https://doi.org/10.1016/j.wear.2004.03.065.

[2] Z. Li, X. Zhao, C. Esveld, R. Dollevoet, and M. Molodova, "An investigation into the causes of squats—correlation analysis and numerical modeling", *Wear*, vol. 265, no. 9–10, pp. 1349–1355, Oct. 2008, ISSN: 0043-1648. DOI: 10.1016/j.wear.2008.02.037.

[3] Z. Li, "Squats on railway rails", in *Wheel–Rail Interface Handbook*, R. Lewis and U. Olofsson, Eds. Elsevier, 2009, ch. Chapter 13, pp. 409–436. DOI: 10.1533/9781845696788.1.409.

[4] M. Naeimi, Z. Li, Z. Qian, *et al.*, "Reconstruction of the rolling contact fatigue cracks in rails using X-ray computed tomography", *NDT and E International*, vol. 92, pp. 199–212, Dec. 2017, ISSN: 09638695. DOI: 10.1016/j.ndteint.2017.09.004.

[5] R. Stock and R. Pippan, "RCF and wear in theory and practice—the influence of rail grade on wear and RCF", *Wear*, vol. 271, no. 1-2, pp. 125–133, May 2011. DOI: https://doi.org/10.1016/j.wear.2010.10.015.

[6] Y. Zhou, S. Wang, T. Wang, Y. Xu, and Z. Li, "Field and laboratory investigation of the relationship between rail head check and wear in a heavy-haul railway", *Wear*, vol. 315, no. 1-2, pp. 68–77, Jul. 2014, ISSN: 00431648. DOI: 10.1016/j.wear.2014.04.004. [Online]. Available: http://dx.doi.org/10.1016/j.wear.2014.04.004.

[7] D. Fletcher, F. Franklin, and A. Kapoor, "Rail surface fatigue and wear", in *Wheel–Rail Interface Handbook*, R. Lewis and U. Olofsson, Eds. Elsevier, 2009, ch. Chapter 9, pp. 280–310, ISBN: 9781845694128. DOI: 10.1533/9781845696788.1.280.

[8] S. Kaewunruen, A. Freimanis, and M. Ishida, "Effect of extreme climate on wheel-rail interaction over rail squats", in *The 6th European Conference on Computational Mechanics (ECCM 6): ECCM6*, 2018.

[9] D. T. Eadie, D. Elvidge, K. Oldknow, *et al.*, "The effects of top of rail friction modifier on wear and rolling contact fatigue: Full-scale rail-wheel test rig evaluation, analysis and modelling", *Wear*, vol. 265, no. 9-10, pp. 1222–1230, Oct. 2008, ISSN: 00431648. DOI: 10.1016/j.wear.2008.02.029.

[10] R. Dollevoet, Z. Li, and O. Arias-Cuevas, "A method for the prediction of head checking initiation location and orientation under operational loading conditions", *Proceedings of the Institution of Mechanical Engineers, Part F: Journal of Rail and Rapid Transit*, vol. 224, no. 5, pp. 369–374, Jul. 2010. DOI: 10.1243/09544097jrrt368.

[11] R. Dollevoet, *Design of an Anti Head Check profile based on stress relief*. PhD thesis, 2010, p. 151, ISBN: 9789036530736. DOI: 10.3990/1.9789036530736.

[12] K. L. Johnson, *Contact mechanics*. Cambridge university press, 1987.

[13] A. Bower and K. Johnson, "The influence of strain hardening on cumulative plastic deformation in rolling and sliding line contact", *Journal of the Mechanics and Physics of Solids*, vol. 37, no. 4, pp. 471–493, Jan. 1989. DOI: https://doi.org/10.1016/0022-5096(89)90025-2.

[14] G. Donzella, M. Faccoli, A. Mazzù, C. Petrogalli, and R. Roberti, "Progressive damage assessment in the near-surface layer of railway wheel-rail couple under cyclic contact", *Wear*, vol. 271, no. 1-2, pp. 408–416, May 2011, ISSN: 00431648. DOI: 10.1016/j.wear.2010.10.042.

[15] W. R. Tyfour, J. H. Beynon, and A. Kapoor, "Deterioration of rolling contact fatigue life of pearlitic rail steel due to dry-wet rolling-sliding line contact", *Wear*, vol. 197, no. 1-2, pp. 255–265, Sep. 1996, ISSN: 00431648. DOI: 10.1016/0043-1648(96)06978-5.

[16] G. Donzella, A. Mazzù, and C. Petrogalli, "Competition between wear and rolling contact fatigue at the wheel-rail interface: Some experimental evidence on rail steel", *Proceedings of the Institution of Mechanical Engineers, Part F: Journal of Rail and Rapid Transit*, vol. 223, no. 1, pp. 31–44, Jan. 2009, ISSN: 09544097. DOI: 10.1243/09544097JRRT161.

[17] J. Flašker, G. Fajdiga, S. Glodež, and T. K. Hellen, "Numerical simulation of surface pitting due to contact loading", *International Journal of Fatigue*, vol. 23, no. 7, pp. 599–605, Aug. 2001, ISSN: 01421123. DOI: 10.1016/S0142-1123(01)00020-2.

[18] A. F. Bower, "The influence of crack face friction and trapped fluid on surface initiated rolling contact fatigue cracks", *Journal of Tribology*, vol. 110, no. 4, pp. 704–711, Oct. 1988, ISSN: 15288897. DOI: 10.1115/1.3261717.

[19] R. Heyder and M. Brehmer, "Empirical studies of head check propagation on the DB network", *Wear*, vol. 314, no. 1-2, pp. 36–43, Jun. 2014, ISSN: 00431648. DOI: 10.1016/j.wear.2013.11.035.

[20] M. d. G. M. da Fonseca Gomes, L. H. de Almeida, L. C. F. Gomes, and I. Le May, "Effects of microstructural parameters on the mechanical properties of eutectoid rail steels", *Materials Characterization*, vol. 39, no. 1, pp. 1–14, Jul. 1997, ISSN: 1044-5803. DOI: 10.1016/s1044-5803(97)00086-7.

[21] A. Elwazri, P. Wanjara, and S. Yue, "The effect of microstructural characteristics of pearlite on the mechanical properties of hypereutectoid steel", *Materials Science and Engineering: A*, vol. 404, no. 1–2, pp. 91–98, Sep. 2005, ISSN: 0921-5093. DOI: 10.1016/j.msea.2005.05.051.

[22] T. Lesage, M. Avettand-Fènoël, D. Balloy, S. Assaf, F. Cristofari, and P. Secordel, "Head check resistance of b320 bainitic rail steel grade", *Materials Today Communications*, vol. 31, p. 103 259, Jun. 2022. DOI: 10.1016/j.mtcomm.2022.103259.

[23] F. Franklin, J. Garnham, C. Davis, D. Fletcher, and A. Kapoor, "The evolution and failure of pearlitic microstructure in rail steel – observations and modelling", in *Wheel–Rail Interface Handbook*, R. Lewis and U. Olofsson, Eds. Elsevier, 2009, ch. Chapter 10, pp. 311–348. DOI: 10.1533/9781845696788.1.311.

[24] H. Chen, Y. Ji, C. Zhang, *et al.*, "Understanding cementite dissolution in pearlitic steels subjected to rolling-sliding contact loading: A combined experimental and theoretical study", *Acta Materialia*, vol. 141, pp. 193–205, Dec. 2017, ISSN: 1359-6454. DOI: 10.1016/j.actamat.2017.09.017.

[25] J. Wen, J. Marteau, S. Bouvier, M. Risbet, F. Cristofari, and P. Secordel, "Comparison of microstructure changes induced in two pearlitic rail steels subjected to a full-scale wheel/rail contact rig test", *Wear*, vol. 456–457, p. 203 354, Sep. 2020, ISSN: 0043-1648. DOI: 10.1016/j.wear.2020.203354.

[26] Y. Hu, L. Zhou, H. Ding, *et al.*, "Microstructure evolution of railway pearlitic wheel steels under rolling-sliding contact loading", *Tribology International*, vol. 154, p. 106 685, Feb. 2021, ISSN: 0301-679X. DOI: 10.1016/j.triboint.2020.106685.

[27] C. Esveld, "The rail", Undefined/Unknown, in *Modern railway track, second edition*, D. Z.-v. Nieuwhuizen, Ed. MRT productions, 2001, ch. Chapter 10, pp. 275–332.

[28] J. Garnham and C. Davis, "Rail materials", in *Wheel–Rail Interface Handbook*, R. Lewis and U. Olofsson, Eds. Elsevier, 2009, ch. Chapter 5, pp. 125–171. DOI: 10.1533/9781845696788.1.125.

[29] S. M. Hasan, D. Chakrabarti, and S. B. Singh, "Dry rolling/sliding wear behaviour of pearlitic rail and newly developed carbide-free bainitic rail steels", *Wear*, vol. 408-409, pp. 151–159, Aug. 2018, ISSN: 00431648. DOI: 10.1016/j.wear.2018.05.006.

[30] J. Lubliner, "Constitutive theory", in *Plasticity theory*. Courier Corporation, 2008, pp. 111–176.

[31] A. Varvani-Farahani, "Cyclic plasticity of metals", in A. A. Roostaei and H. Jahed, Eds. Elsevier, 2022, ch. Chapter 5, pp. 139–174. DOI: https://doi.org/10.1016/C2018-0-04874-4.

[32] P. P. Benham and H. Ford, "Low endurance fatigue of a mild steel and an aluminium alloy", *Journal of Mechanical Engineering Science*, vol. 3, no. 2, pp. 119–132, Jun. 1961, ISSN: 2058-3389. DOI: 10.1243/jmes_jour_1961_003_017_02.

[33] S. K. Paul, "A critical review of experimental aspects in ratcheting fatigue: Microstructure to specimen to component", *Journal of Materials Research and Technology*, vol. 8, no. 5, pp. 4894–4914, 2019, ISSN: 2238-7854. DOI: https://doi.org/10.1016/j.jmrt.2019.06.014. [Online]. Available: https://www.sciencedirect.com/science/article/pii/S2238785419300900.

[34] J. Ringsberg, "Prediction of fatigue crack initiation for rolling contact fatigue", *International Journal of Fatigue*, vol. 22, no. 3, pp. 205–215, Mar. 2000. DOI: https://doi.org/10.1016/S0142-1123(99)00125-5.

[35] H. Hübel, "Basic conditions for material and structural ratcheting", *Nuclear Engineering and Design*, vol. 162, no. 1, pp. 55–65, Mar. 1996. DOI: 10.1016/0029-5493(95)01136-6.

[36] J. Chaboche, "Time-independent constitutive theories for cyclic plasticity", *International Journal of Plasticity*, vol. 2, no. 2, pp. 149–188, Jan. 1986. DOI: 10.1016/0749-6419(86)90010-0.

[37] Y. Jiang and H. Sehitoglu, "Modeling of cyclic ratchetting plasticity, part i: Development of constitutive relations", *Journal of Applied Mechanics*, vol. 63, no. 3, pp. 720–725, Sep. 1996. DOI: 10.1115/1.2823355.

[38] S. Bari and T. Hassan, "Anatomy of coupled constitutive models for ratcheting simulation", *International Journal of Plasticity*, vol. 16, no. 3-4, pp. 381–409, Jan. 2000. DOI: 10.1016/s0749-6419(99)00059-5.

[39] C. L. Pun, Q. Kan, P. J. Mutton, G. Kang, and W. Yan, "Ratcheting behaviour of high strength rail steels under bi-axial compression–torsion loadings: Experiment and simulation", *International Journal of Fatigue*, vol. 66, pp. 138–154, Sep. 2014. DOI: 10.1016/j.ijfatigue.2014.03.021.

[40] A. Kapoor and K. Johnson, "Effect of changes in contact geometry on shakedown of surfaces in rolling/sliding contact", *International Journal of Mechanical Sciences*, vol. 34, no. 3, pp. 223–239, Mar. 1992. DOI: 10.1016/0020-7403(92)90073-p.

[41] M. Abdel-Karim, "Modified kinematic hardening rules for simulations of ratchetting", *International Journal of Plasticity*, vol. 25, no. 8, pp. 1560–1587, Aug. 2009. DOI: 10.1016/j.ijplas.2008.10.004.

[42] R. v. Mises, "Mechanik der festen körper im plastisch- deformablen zustand", *Nachrichten von der Gesellschaft der Wissenschaften zu Göttingen, Mathematisch-Physikalische Klasse*, vol. 1913, pp. 582–592, 1913. [Online]. Available: http://eudml.org/doc/58894.

[43] C. O. Frederick and P. J. Armstrong, "A mathematical representation of the multiaxial bauschinger effect", *Materials at High Temperatures*, vol. 24, no. 1, pp. 1–26, Apr. 2007. DOI: 10.3184/096034007x207589.

[44] E. Voce, "A practical strain hardening function", *Metallurgia*, vol. 51, pp. 219–226, 1955.

[45] C. White, C. Bronkhorst, and L. Anand, "An improved isotropic—kinematic hardening model for moderate deformation metal plasticity", *Mechanics of Materials*, vol. 10, no. 1–2, pp. 127–147, Nov. 1990, ISSN: 0167-6636. DOI: 10.1016/0167-6636(90)90023-9.

[46] A. Ekberg, "Anisotropy and rolling contact fatigue of railway wheels", *International Journal of Fatigue*, vol. 23, no. 1, pp. 29–43, Jan. 2001, ISSN: 0142-1123. DOI: 10.1016/s0142-1123(00)00070-0.

[47] N. Ohno and J.-D. Wang, "Kinematic hardening rules with critical state of dynamic recovery, part i: Formulation and basic features for ratchetting behavior", *International Journal of Plasticity*, vol. 9, no. 3, pp. 375–390, Jan. 1993. DOI: 10.1016/0749-6419(93)90042-o.

[48] M. Abdel-Karim and N. Ohno, "Kinematic hardening model suitable for ratchetting with steady-state", *International Journal of Plasticity*, vol. 16, no. 3–4, pp. 225–240, Jan. 2000, ISSN: 0749-6419. DOI: 10.1016/s0749-6419(99)00052-2.

[49] G. Z. Kang, Y. Li, Q. Gao, Q. H. Kan, and J. Zhang, "Uniaxial ratchetting in steels with different cyclic softening/hardening behaviours", *Fatigue & Fracture of Engineering Materials & Structures*, vol. 29, no. 2, pp. 93–103, Feb. 2006. DOI: 10.1111/j.1460-2695.2006.00964.x.

[50] O. Arias-Cuevas, Z. Li, R. Lewis, and E. Gallardo-Hernández, "Rolling–sliding laboratory tests of friction modifiers in dry and wet wheel–rail contacts", *Wear*, vol. 268, no. 3-4, pp. 543–551, Feb. 2010. DOI: https://doi.org/10.1016/j.wear.2009.09.015.

[51] F. Ren, Z. Yang, O. Hajizad, J. Moraal, and Z. Li, "Experimental investigation into the initiation of head check damage using v-track", in *12th International Conference on Contact Mechanics and Wear of Rail/Wheel Systems, 4-7 September 2022, Melbourne, Victoria, Australia*, 2022.

[52] J. H. Beynon, J. E. Garnham, and K. J. Sawley, "Rolling contact fatigue of three pearlitic rail steels", *Wear*, vol. 192, no. 1-2, pp. 94–111, Mar. 1996, ISSN: 00431648. DOI: 10.1016/0043-1648(95)06776-0.

[53] O. Arias-Cuevas, Z. Li, and R. Lewis, "A laboratory investigation on the influence of the particle size and slip during sanding on the adhesion and wear in the wheel–rail contact", *Wear*, vol. 271, no. 1-2, pp. 14–24, May 2011. DOI: https://doi.org/10.1016/j.wear.2010.10.050.

[54] D. Fletcher and S. Lewis, "Creep curve measurement to support wear and adhesion modelling, using a continuously variable creep twin disc machine", *Wear*, vol. 298-299, pp. 57–65, Feb. 2013. DOI: 10.1016/j.wear.2012.11.065.

[55] M. Hiensch and N. Burgelman, "Rolling contact fatigue: Damage function development from two-disc test data", *Wear*, vol. 430-431, pp. 376–382, Jul. 2019. DOI: https://doi.org/10.1016/j.wear.2019.05.028.

[56] X. Zhao, Q. Chen, Y. Liu, X. Qiu, E. Meli, and A. Rindi, "Effects of slip ratio and contact stress on rolling contact fatigue of defected rail materials", *Engineering Failure Analysis*, vol. 131, p. 105 817, Jan. 2022, ISSN: 1350-6307. DOI: 10.1016/j.engfailanal.2021.105817.

[57] Y. Li, Y. Wu, P. Mutton, C. Qiu, and W. Yan, "A ratcheting mechanism-based numerical model to predict damage initiation in twin-disc tests of premium rail steels", *Engineering Failure Analysis*, vol. 146, p. 107 066, Apr. 2023, ISSN: 1350-6307. DOI: 10.1016/j.engfailanal.2023.107066.

[58] Y. Xie, W. Wang, J. Guo, *et al.*, "Rail rolling contact fatigue response diagram construction and shakedown map optimization", *Wear*, vol. 528–529, p. 204 964, Sep. 2023, ISSN: 0043-1648. DOI: 10.1016/j.wear.2023.204964.

[59] D. Chen, M. Zhong, M. Mou, *et al.*, "Research on the damage mechanism of the rolling contact fatigue of a wheel–rail contact system under the influences of surface defects", *Engineering Failure Analysis*, vol. 164, p. 108 631, Oct. 2024, ISSN: 1350-6307. DOI: 10.1016/j.engfailanal.2024.108631.

[60] A. C. Athukorala, D. V. D. Pellegrin, and K. I. Kourousis, "Characterisation of head-hardened rail steel in terms of cyclic plasticity response and microstructure for improved material modelling", *Wear*, vol. 366-367, pp. 416–424, Nov. 2016. DOI: https://doi.org/10.1016/j.wear.2016.03.024.

[61] S. Liu, U. De Silva, D. Chen, A. C. Leslie, and P. A. Meehan, "Investigation of wheel squeal noise under mode coupling using two-disk testrig experiments", *Wear*, vol. 530–531, p. 205 035, Oct. 2023, ISSN: 0043-1648. DOI: 10.1016/j.wear.2023.205035.

[62] K. Oldknow, R. Stock, and E. Vollebregt, "Effects of rail hardness on transverse profile evolution and computed contact conditions in a full-scale wheel-rail test rig evaluation", *Wear*, vol. 560–561, p. 205 589, Jan. 2025, ISSN: 0043-1648. DOI: 10.1016/j.wear.2024.205589.

[63] M. Naeimi, Z. Li, R. H. Petrov, J. Sietsma, and R. Dollevoet, "Development of a new downscale setup for wheel-rail contact experiments under impact loading conditions", *Experimental Techniques*, vol. 42, no. 1, pp. 1–17, Oct. 2017. DOI: 10.1007/s40799-017-0216-z.

[64] Z. Yang, P. Zhang, J. Moraal, and Z. Li, "An experimental study on the effects of friction modifiers on wheel–rail dynamic interactions with various angles of attack", *Railway Engineering Science*, vol. 30, no. 3, pp. 360–382, Aug. 2022, ISSN: 2662-4753. DOI: 10.1007/s40534-022-00285-y.

[65] C. He, Z. Yang, P. Zhang, *et al.*, "A finite element thermomechanical analysis of the development of wheel polygonal wear", *Tribology International*, vol. 195, p. 109 577, Jul. 2024, ISSN: 0301-679X. DOI: 10.1016/j.triboint.2024.109577.

[66] F. Ren, Z. Yang, and Z. Li, "Experimental and numerical investigation into head check initiation on the v-track test rig", 2024, to be subimitted.

[67] M. Naeimi, Z. Li, and R. Dollevoet, "Determining the angles of squat cracks via CT scanning and metallographic observations", *Engineering Fracture Mechanics*, vol. 230, p. 107 016, May 2020. DOI: https://doi.org/10.1016/j.engfracmech.2020.107016.

[68] J. J. Kalker, *Three-Dimensional Elastic Bodies in Rolling Contact*. Springer Netherlands, Oct. 31, 1990, 344 pp., ISBN: 0792307127. [Online]. Available: https://www.ebook.de/de/product/2225648/j_j_kalker_three_dimensional_elastic_bodies_in_rolling_contact.html.

[69] J. Kalker, "Wheel-rail rolling contact theory", *Wear*, vol. 144, no. 1-2, pp. 243–261, Apr. 1991. DOI: 10.1016/0043-1648(91)90018-p.

[70] Z. Li, "Wheel-rail rolling contact and its application to wear simulation", Ph.D. dissertation, Electrical Engineering, Mathematics and Computer Science, TU Delft, 2002.

[71] X. Zhao and Z. Li, "The solution of frictional wheel–rail rolling contact with a 3d transient finite element model: Validation and error analysis", *Wear*, vol. 271, no. 1-2, pp. 444–452, May 2011. DOI: https://doi.org/10.1016/j.wear.2010.10.007.

[72] X. Deng, Z. Qian, and R. Dollevoet, "Lagrangian explicit finite element modeling for spin-rolling contact", *Journal of Tribology*, vol. 137, no. 4, Oct. 2015. DOI: 10.1115/1.4030709.

[73] Z. Wei, L. Z., Z. Qian, R. Chen, and R. Dollevoet, "3d fe modelling and validation of frictional contact with partial slip in compression-rolling evolution", *International Journal of Rail Transportation*, vol. 4, no. 1, pp. 20–36, Oct. 2015. DOI: 10.1080/23248378.2015.1094753.

[74] Z. Yang, X. Deng, and Z. Li, "Numerical modeling of dynamic frictional rolling contact with an explicit finite element method", *Tribology International*, vol. 129, pp. 214–231, Jan. 2019. DOI: 10.1016/j.triboint.2018.08.028.

[75] X. Deng, Z. Li, Z. Qian, W. Zhai, Q. Xiao, and R. Dollevoet, "Pre-cracking development of weld-induced squats due to plastic deformation: Five-year field monitoring and numerical analysis", *International Journal of Fatigue*, vol. 127, pp. 431–444, Oct. 2019, ISSN: 0142-1123. DOI: 10.1016/j.ijfatigue.2019.06.013.

[76] C. L. Pun, Q. Kan, P. J. Mutton, G. Kang, and W. Yan, "An efficient computational approach to evaluate the ratcheting performance of rail steels under cyclic rolling contact in service", *International Journal of Mechanical Sciences*, vol. 101-102, pp. 214–226, Oct. 2015. DOI: https://doi.org/10.1016/j.ijmecsci.2015.08.008.

[77] A. Bower and K. Johnson, "Plastic flow and shakedown of the rail surface in repeated wheel-rail contact", *Wear*, vol. 144, no. 1-2, pp. 1–18, Apr. 1991. DOI: 10.1016/0043-1648(91)90003-d.

[78] M. Pletz, K. A. Meyer, D. Künstner, S. Scheriau, and W. Daves, "Cyclic plastic deformation of rails in rolling/sliding contact –quasistatic FE calculations using different plasticity models", *Wear*, vol. 436-437, p. 202 992, Oct. 2019, ISSN: 00431648. DOI: 10.1016/j.wear.2019.202992.

[79] Y. Wu, J. Zhao, H. Miao, *et al.*, "3d rolling contact finite element analysis of high-speed railway turnout considering ratchetting effect", *Engineering Failure Analysis*, vol. 160, p. 108 171, Jun. 2024, ISSN: 1350-6307. DOI: 10.1016/j.engfailanal.2024.108171.

[80] Z. Zhou, W. Li, Z. Wen, S. Zhou, and G. Tao, "Three-dimensional elastic–plastic stress analysis of wheel–rail cyclic rolling contact using finite element method", *Wear*, vol. 542–543, p. 205 277, Apr. 2024, ISSN: 0043-1648. DOI: 10.1016/j.wear.2024.205277.

[81] W. Daves, W. Kubin, S. Scheriau, and M. Pletz, "A finite element model to simulate the physical mechanisms of wear and crack initiation in wheel/rail contact", *Wear*, vol. 366-367, pp. 78–83, Nov. 2016. DOI: 10.1016/j.wear.2016.05.027.

[82] Y. Zhou, X. Zheng, J. Jiang, and D. Kuang, "Modeling of rail head checks by X-ray computed tomography scan technology", *International Journal of Fatigue*, vol. 100, pp. 21–31, Jul. 2017, ISSN: 01421123. DOI: 10.1016/j.ijfatigue.2017.03.005.

[83] H. Su, C. L. Pun, P. Mutton, Q. Kan, and W. Yan, "Numerical study on the ratcheting performance of heavy haul rails in curved tracks", *Wear*, vol. 436-437, p. 203 026, Oct. 2019. DOI: 10.1016/j.wear.2019.203026.

[84] F. Ren, Z. Yang, and Z. Li, "An efficient 3d finite element procedure for simulating wheel–rail cyclic contact and ratcheting", *Tribology International*, p. 109 878, Jun. 2024, ISSN: 0301-679X. DOI: 10.1016/j.triboint.2024.109878.

[85] A. Kapoor, "Wear by plastic ratchetting", *Wear*, vol. 212, no. 1, pp. 119–130, Nov. 1997. DOI: 10.1016/s0043-1648(97)00083-5.

[86] A. Kapoor, "A re-evaluation of the life to rupture of ductile metals by cyclic plastic strain", *Fatigue & Fracture of Engineering Materials and Structures*, vol. 17, no. 2, pp. 201–219, Feb. 1994. DOI: https://doi.org/10.1111/j.1460-2695.1994.tb00801.x.

[87] A. Kapoor, J. H. Beynon, D. I. Fletcher, and M. Loo-Morrey, "Computer simulation of strain accumulation and hardening for pearlitic rail steel undergoing repeated contact", *The Journal of Strain Analysis for Engineering Design*, vol. 39, no. 4, pp. 383–396, May 2004. DOI: 10.1243/0309324041223935.

[88] J. Chaboche, "On some modifications of kinematic hardening to improve the description of ratchetting effects", *International Journal of Plasticity*, vol. 7, no. 7, pp. 661–678, Jan. 1991. DOI: 10.1016/0749-6419(91)90050-9.

[89] N. Ohno and J. Wang, "On modelling of kinematic hardening for ratcheting behaviour", *Nuclear Engineering and Design*, vol. 153, no. 2-3, pp. 205–212, Jan. 1995, ISSN: 00295493. DOI: 10.1016/0029-5493(95)90012-8.

[90] J. Lu, W. Sun, A. Becker, and A. A. Saad, "Simulation of the fatigue behaviour of a power plant steel with a damage variable", *International Journal of Mechanical Sciences*, vol. 100, pp. 145–157, Sep. 2015, ISSN: 0020-7403. DOI: 10.1016/j.ijmecsci.2015.06.019.

[91] L. Xu, X. Nie, J. Fan, M. Tao, and R. Ding, "Cyclic hardening and softening behavior of the low yield point steel BLY160: Experimental response and constitutive modeling", *International Journal of Plasticity*, vol. 78, pp. 44–63, Mar. 2016. DOI: 10.1016/j.ijplas.2015.10.009.

[92] S. J. Lorenz, F. Sadeghi, and C. Wang, "Effect of spatial hardness distribution in rolling contact fatigue performance of bearing contacts", *Tribology International*, vol. 171, p. 107 550, Jul. 2022, ISSN: 0301-679X. DOI: 10.1016/j.triboint.2022.107550.

[93] A. Mazzù, C. Petrogalli, and M. Faccoli, "An integrated model for competitive damage mechanisms assessment in railway wheel steels", *Wear*, vol. 322-323, pp. 181–191, Jan. 2015. DOI: https://doi.org/10.1016/j.wear.2014.11.013.

[94] B. Zhao, F. Shen, Y. Cui, Y. Xie, and K. Zhou, "Damage analysis for an elastic-plastic body in cylindrical contact with a rigid plane", *Tribology International*, vol. 115, pp. 18–27, Nov. 2017, ISSN: 0301-679X. DOI: 10.1016/j.triboint.2017.05.009.

[95] A. Mazzù, D. Battini, and N. Zani, "Computational assessment of ratcheting in rail-wheel contact with solid contaminant", *Wear*, p. 205 346, Mar. 2024, ISSN: 0043-1648. DOI: 10.1016/j.wear.2024.205346.

[96] K. L. Johnson, "Plastic deformation in rolling contact", in *Rolling Contact Phenomena*, Springer Vienna, 2000, pp. 163–201. DOI: 10.1007/978-3-7091-2782-7_3.

[97] A. Mazzù and G. Donzella, "A model for predicting plastic strain and surface cracks at steady-state wear and ratcheting regime", *Wear*, vol. 400-401, pp. 127–136, Apr. 2018. DOI: 10.1016/j.wear.2018.01.002.

[98] F. Franklin, J. Garnham, D. Fletcher, C. Davis, and A. Kapoor, "Modelling rail steel microstructure and its effect on crack initiation", *Wear*, vol. 265, no. 9–10, pp. 1332–1341, Oct. 2008, ISSN: 0043-1648. DOI: 10.1016/j.wear.2008.03.027.

[99] Z. Yang, Z. Li, and R. Dollevoet, "Modelling of non-steady-state transition from single-point to two-point rolling contact", *Tribology International*, vol. 101, pp. 152–163, Sep. 2016, ISSN: 0301-679X. DOI: 10.1016/j.triboint.2016.04.023.

[100] X. Zhao and Z. Li, "A three-dimensional finite element solution of frictional wheel–rail rolling contact in elasto-plasticity", *Proceedings of the Institution of Mechanical Engineers, Part J: Journal of Engineering Tribology*, vol. 229, no. 1, pp. 86–100, Jul. 2014. DOI: https://doi.org/10.1177/1350650114543717.

[101] M. Pletz, W. Daves, W. Yao, W. Kubin, and S. Scheriau, "Multi-scale finite element modeling to describe rolling contact fatigue in a wheel–rail test rig", *Tribology International*, vol. 80, pp. 147–155, Dec. 2014. DOI: 10.1016/j.triboint.2014.07.005.

[102] Z. Yang and Z. Li, "A numerical study on waves induced by wheel-rail contact", *International Journal of Mechanical Sciences*, vol. 161-162, p. 105 069, Oct. 2019. DOI: 10.1016/j.ijmecsci.2019.105069.

[103] S. Li, M. Naeimi, C. He, R. Dollevoet, and Z. Li, "An integrated 3d dynamic fe vehicle-track model in elasto-plasticity to investigate short pitch corrugation under cyclic wheel loads", *Structures*, vol. 53, pp. 1000–1011, Jul. 2023, ISSN: 2352-0124. DOI: 10.1016/j.istruc.2023.05.001.

[104] B. Wu, W. Wang, J. Pan, *et al.*, "Study on corrugated wear on high-speed railways based on an improved finite element model of wheel-rail rolling contact", *Tribology International*, vol. 179, p. 108 199, Jan. 2023, ISSN: 0301-679X. DOI: 10.1016/j.triboint.2022.108199.

[105] V. L. Popov, "Contact mechanics and friction", in Springer Berlin Heidelberg, 2010, ch. 19, pp. 301–322. DOI: 10.1007/978-3-642-10803-7.

[106] P. Zhang, J. Moraal, and Z. Li, "Design, calibration and validation of a wheel-rail contact force measurement system in v-track", *Measurement*, vol. 175, p. 109 105, Apr. 2021. DOI: https://doi.org/10.1016/j.measurement.2021.109105.

[107] A. Kapoor and F. J. Franklin, "Tribological layers and the wear of ductile materials", in *Wear*, vol. 245, Elsevier BV, Oct. 2000, pp. 204–215. DOI: 10.1016/S0043-1648(00)00480-4.

[108] P. Karvan and A. Varvani-Farahani, "Isotropic-kinematic hardening framework to assess ratcheting response of steel samples undergoing asymmetric loading cycles", *Fatigue & Fracture of Engineering Materials & Structures*, vol. 42, no. 1, pp. 295–306, Aug. 2018. DOI: 10.1111/ffe.12905.

[109] A. Nath, K. K. Ray, and S. V. Barai, "Evaluation of ratcheting behaviour in cyclically stable steels through use of a combined kinematic-isotropic hardening rule and a genetic algorithm optimization technique", *International Journal of Mechanical Sciences*, vol. 152, pp. 138–150, Mar. 2019. DOI: 10.1016/j.ijmecsci.2018.12.047.

[110] G. Schleinzer and F. Fischer, "Residual stresses in new rails", *Materials Science and Engineering: A*, vol. 288, no. 2, pp. 280–283, Sep. 2000. DOI: 10.1016/s0921-5093(00)00872-8.

[111] X. Chen, "On the ohno-wang kinematic hardening rules for multiaxial ratcheting modeling of medium carbon steel", *International Journal of Plasticity*, vol. 21, no. 1, pp. 161–184, Jan. 2005. DOI: 10.1016/j.ijplas.2004.05.005.

[112] S. Bari and T. Hassan, "An advancement in cyclic plasticity modeling for multiaxial ratcheting simulation", *International Journal of Plasticity*, vol. 18, no. 7, pp. 873–894, Jul. 2002. DOI: 10.1016/s0749-6419(01)00012-2.

[113] A. Monk-Steel, D. Thompson, F. de Beer, and M. Janssens, "An investigation into the influence of longitudinal creepage on railway squeal noise due to lateral creepage", *Journal of Sound and Vibration*, vol. 293, no. 3-5, pp. 766–776, Jun. 2006. DOI: 10.1016/j.jsv.2005.12.004.

[114] O. Hajizad, A. Kumar, Z. Li, R. H. Petrov, J. Sietsma, and R. Dollevoet, "Influence of microstructure on mechanical properties of bainitic steels in railway applications", *Metals*, vol. 9, no. 7, p. 778, Jul. 2019, ISSN: 20754701. DOI: 10.3390/met9070778.

[115] P. Zhang, S. Li, and Z. Li, "Short pitch corrugation mitigation by rail constraint design", *International Journal of Mechanical Sciences*, vol. 243, p. 108 037, Apr. 2023. DOI: 10.1016/j.ijmecsci.2022.108037.

[116] G. Donzella, M. Faccoli, A. Ghidini, A. Mazzù, and R. Roberti, "The competitive role of wear and RCF in a rail steel", *Engineering Fracture Mechanics*, vol. 72, no. 2, pp. 287–308, Jan. 2005, ISSN: 00137944. DOI: 10.1016/j.engfracmech.2004.04.011.

[117] Z. Yang, A. Boogaard, Z. Wei, J. Liu, R. Dollevoet, and Z. Li, "Numerical study of wheel-rail impact contact solutions at an insulated rail joint", *International Journal of Mechanical Sciences*, vol. 138-139, pp. 310–322, Apr. 2018. DOI: 10.1016/j.ijmecsci.2018.02.025.

[118] G. Kang and Q. Gao, "Uniaxial and non-proportionally multiaxial ratcheting of u71mn rail steel: Experiments and simulations", *Mechanics of Materials*, vol. 34, no. 12, pp. 809–820, Dec. 2002. DOI: 10.1016/s0167-6636(02)00198-9.

[119] A. Ekberg, B. Åkesson, and E. Kabo, "Wheel/rail rolling contact fatigue – probe, predict, prevent", *Wear*, vol. 314, no. 1–2, pp. 2–12, Jun. 2014, ISSN: 0043-1648. DOI: 10.1016/j.wear.2013.12.004.

[120] A. A. Roostaei and H. Jahed, Eds., *Cyclic Plasticity of Metals*. Elsevier, 2022. DOI: 10.1016/c2018-0-04874-4.

[121] W. Prager, "Recent developments in the mathematical theory of plasticity", *Journal of applied physics*, vol. 20, no. 3, pp. 235–241, 1949.

[122] A. R. Curtis, M. J. D. Powell, and J. K. Reid, "On the estimation of sparse jacobian matrices", *IMA Journal of Applied Mathematics*, vol. 13, no. 1, pp. 117–119, Feb. 1974. DOI: 10.1093/imamat/13.1.117.

[123] J. Nocedal and S. J. Wright, *Numerical optimization*. Springer, 1999.

[124] H. Ramezansefat and S. Shahbeyk, "The chaboche hardening rule: A re-evaluation of calibration procedures and a modified rule with an evolving material parameter", *Mechanics Research Communications*, vol. 69, pp. 150–158, Oct. 2015. DOI: 10.1016/j.mechrescom.2015.08.003.

[125] M. Khurshid, M. Leitner, Z. Barsoum, and C. Schneider, "Residual stress state induced by high frequency mechanical impact treatment in different steel grades – numerical and experimental study", *International Journal of Mechanical Sciences*, vol. 123, pp. 34–42, Apr. 2017, ISSN: 0020-7403. DOI: 10.1016/j.ijmecsci.2017.01.027.

[126] A. Bower, "Cyclic hardening properties of hard-drawn copper and rail steel", *Journal of the Mechanics and Physics of Solids*, vol. 37, no. 4, pp. 455–470, Jan. 1989, ISSN: 0022-5096. DOI: 10.1016/0022-5096(89)90024-0.

[127] T. Hassan and S. Kyriakides, "Ratcheting in cyclic plasticity, part i: Uniaxial behavior", *International Journal of Plasticity*, vol. 8, no. 1, pp. 91–116, Jan. 1992, ISSN: 0749-6419. DOI: 10.1016/0749-6419(92)90040-j.

[128] A. Mohammadpour and T. Chakherlou, "Numerical and experimental study of an interference fitted joint using a large deformation chaboche type combined isotropic–kinematic hardening law and mortar contact method", *International Journal of Mechanical Sciences*, vol. 106, pp. 297–318, Feb. 2016, ISSN: 0020-7403. DOI: 10.1016/j.ijmecsci.2015.10.012.

[129] J.-H. Hwang, Y.-J. Kim, J.-W. Kim, and S.-E. Kim, "Initial cyclic hardening behavior of cracked structures under large-amplitude cyclic loading", *Engineering Fracture Mechanics*, vol. 254, p. 107 911, Sep. 2021, ISSN: 0013-7944. DOI: 10.1016/j.engfracmech.2021.107911.

[130] F. Ren, Z. Yang, and Z. Li, "Experimental investigation and constitutive modelling of the mechanical and ratcheting properties in rail steels", 2024, to be submitted.

[131] *Ls-dyna keyword user's manual volume ii material models*, LIVERMORE SOFTWARE TECHNOLOGY, 2020.

[132] *Ls-dyna keyword user's manual volume i*, LIVERMORE SOFTWARE TECHNOLOGY, 2020.

[133] Z. Wei, C. Shen, Z. Li, and R. Dollevoet, "Wheel–rail impact at crossings: Relating dynamic frictional contact to degradation", *Journal of Computational and Nonlinear Dynamics*, vol. 12, no. 4, Feb. 2017. DOI: 10.1115/1.4035823.

ACKNOWLEDGEMENTS

Embarking upon this five-year PhD journey has proven to be both a rigorous and rewarding endeavour, one that has demanded perseverance, adaptability, and the invaluable support of many individuals. The research was undertaken amidst unprecedented global circumstances, as the COVID-19 pandemic introduced significant obstacles, from prolonged lockdowns to remote working constraints. Navigating these complexities has been an exercise in resilience, and it has enriched both the process and outcome of this research in ways that would not have been otherwise possible. I am profoundly grateful to those whose guidance and encouragement have made this journey both possible and meaningful.

I extend my sincere gratitude to my promoter, Prof. dr. Zili Li, whose expertise, insight, and steadfast support have been invaluable to this research. His intellectual guidance and encouragement provided a constant source of motivation, especially during the more challenging periods. I am equally indebted to my co-promoter, Dr. Zhen Yang, for his thoughtful feedback, incisive critique, and unwavering commitment to excellence, which have undoubtedly strengthened the quality of this work. Their patience and dedication have been instrumental to both my academic development and the successful completion of this dissertation. I also owe thanks to my former co-promoter, Dr. Alfredo Nunez Vicencio, for supporting me in passing my Go-NoGo after the first year of my PhD. My thanks also go to the committe members who provide their valuable comments to improve my final dissertation. Additionally, I am extremely grateful to Prof. Andrei Metrikine, who was also my supervisor during my master graduation, for believing in my ability to complete the challenging path of a PhD.

I am also thankful to my colleagues, Jan Moraal, Derek Bochove, Dr. Ankit Kumar, Dr. Vitoria Mattos Ferreira, Dr. Sudhindra Ayenampudi and Dr. Omid Hajizad, for their collaboration and insights throughout the MaxLife project. My gratitude extends to Prof. Jilt Sietsma, Dr. Viktoria Savran, Dr. Ivan Shevtsov, Dr. Pei Yan, Franscois Cristofari, Prof. Roumen Petrov, Bart Schotsman and Prof. Maria Santofimia Navarro for their guidance and advice during our M2i joint project meetings. I am also grateful to Fred Schilperoort, Peter de Vries, and Dave Ruijtenbeek for their assistance in completing the material tests. Working alongside such talented and supportive individuals has been a privilege, and their shared knowledge, encouragement, and constructive feedback have significantly enriched my research and my experience in this academic community. Special thanks to Jacques Aousin and Giray Arslan, whose excellent assistance alleviated the burdens of sample preparation. I would also like to extend particular thanks to Dr. Junping Zhong, Dr. Wenli Jia, and Dr. dr. Yuanchen Zeng. We were like the boys of Easy Company sharing a foxhole in the Ardennes forest, betting on how our "enemy" —COVID-19— might strike during the pandemic lockdowns.

My thanks also go to my wonderful colleagues within our Railway Engineering group, including Prof. Rolf Dollevoet, whose research on HCs provided a significant source of in-

spiration. Jacqueline Barnhoorn has been immensely helpful with administrative tasks, and Ellard Groenewegen offered invaluable support with project finances. I would also like to thank Dr. Pan Zhang, who assisted me with V-Track and accompanied me on a memorable drive along the Great Ocean Road and fined for speeding, and Chunyan He and Longge Su, who supported me greatly with the demanding tasks of 3D scans, as well as Dr. Valeri Markine, Dr. Li Wang, Dr. Chen Shen, Dr. Siwarak Unsiwilai, Dr. Yunlong Guo, Dr. Hongrui Wang, Dr. Taniya Kapoor, Wassamon Phusakulkajorn, Gokul Jayasree Krishnan, Shashanka Katta, and Nikhil Manakshya.

Lastly, I owe a profound debt of gratitude to my family: my wife, my parents and in-laws, my grandparents, and our dog, Latte. My heartfelt thanks extend to meine Deutsche Familie—Malen, Armin, Marki, Päddy, Chrissy, and Oma Lotte—whose kindness and support have been a source of warmth and encouragement. I am equally grateful to my friends, Hao & Yuting, Ran & Giulia, Ruben, Alejandro, whose unwavering encouragement and support have been an anchor throughout this journey, especially during the lockdowns. I would also like to express my heartfelt remembrance of my grandfather, who sadly passed away in March. His memory has been a constant source of inspiration and resilience, and I dedicate this work in part to him. This dissertation stands as much as a testament to their faith and encouragement as it does to my own efforts. Completing this work has been a deeply transformative chapter in my life, and I remain indebted to everyone who has contributed to its realisation.

Fang Ren
November 2024
Rotterdam

CURRICULUM VITÆ

Fang REN

16-05-1988 Born in Qingyang, People's Republic of China.

WORK EXPERIENCE

2024–present Postdoctoral researcher
Delft University of Technology, the Netherlands

2019–2024 Ph.D candidate
Delft University of Technology, the Netherlands

2017–2019 Project engineer
DEME group, Belgium

2014–2017 Naval architect, Structural engineer
Temporary Works Design, the Netherlands

EDUCATION

2019–2023 BSc Data science and business analytics
University of London, first class honours, part-time

2012–2014 MSc Offshore and dredging engineering
Delft University of Technology, cum laude, the Netherlands

2011–2012 MSc Engineering project management
University of Manchester, the UK

2007–2011 BSc Harbour, waterway and coastal engineering
Hohai University, the PRC

LIST OF PUBLICATIONS

Journal paper:

5. **F. Ren, Z. Yang, Z. Li**, *Simulation and validation of the ratcheting effects in B320 and R260MN rails under cyclic wheel-rail contacts*, 2024, to be submitted

4. **F. Ren, Z. Yang, Z. Li**, *Experimental investigation and constitutive modelling of the mechanical and ratcheting properties in rail steels*, 2024, to be submitted

3. **F. Ren, Z. Yang, Z. Li**, *Experimental and numerical investigation into head check initiation on the V-Track test rig*, 2024, submitted to international journal for potential publication

2. **F. Ren, Z. Yang, Z. Li**, *An efficient 3D finite element procedure for simulating wheel–rail cyclic contact and ratcheting*, Tribology International, Elsevier BV, 2024, 109878

Conference paper:

1. **F. Ren, Z. Yang, O. Hajizad, J. Moraal, Z. Li**, *Experimental investigation into the initiation of head check damage using V-Track* , 12th International Conference on Contact Mechanics and Wear of Rail/Wheel Systems, 4-7 September 2022, Melbourne, Victoria, Australia, 2022